

Jiaqi Wang

# Numerical investigation of oscillatory flow around a step cylinder

Master's thesis in Marine Technology

Supervisor: Lars Erik Holmedal

Co-supervisor: Cai Tian

June 2022



Jiaqi Wang

# **Numerical investigation of oscillatory flow around a step cylinder**

Master's thesis in Marine Technology  
Supervisor: Lars Erik Holmedal  
Co-supervisor: Cai Tian  
June 2022

Norwegian University of Science and Technology  
Faculty of Engineering  
Department of Marine Technology



Kunnskap for en bedre verden





# Preface

This thesis is intended to be a result for my Master's degree in Marine Technology and it is written at Institute of Marine Technology at the Norwegian University of Science and Technology in the spring of 2022. This thesis describes the numerical investigation of oscillatory flow around a step cylinder and a powerful in-house code MGLET (Multi Grid Large Eddy Turbulence) is used as the numerical solver. All of the CFD simulations are performed on the supercomputer Betzy.

The topic of the thesis was inspired by my supervisor, professor Lars Erik Holmedal, co-supervisor, postdoctoral fellow Cai Tian, and postdoctoral fellow Jianxun Zhu. With their helps I have learned the basics of CFD, the basics of uniform and oscillatory flow around a circular cylinder and around a step cylinder. I have been familiar with the operation process of the in-house code MGLET and the supercomputer Betzy.

I would like to thank my supervisor, professor Lars Erik Holmedal. He motivate me with his supportive attitude and encouragement.

Next I would like to thank my co-supervisor Cai Tian. He taught me step by step how to use the MGLET and the supercomputer Betzy. From the time I started doing simulations and writing my dissertation, he hepled me with his extensive knowledge and helped me solve problems when I encountered them.

I would also like to thank postdoctoral fellow Jianxun Zhu for his help and inspiration.

---

# Table of Contents

List of Figures	iii
List of Tables	vi
Nomenclature	vii
<b>1 Abstract</b>	<b>1</b>
<b>2 Introudction</b>	<b>2</b>
2.1 State of the art . . . . .	2
2.1.1 Oscillatory flow around a circular cylinder . . . . .	2
2.1.2 Flow around a step cylinder . . . . .	4
2.2 Motivation . . . . .	5
2.3 Structure of the thesis . . . . .	6
<b>3 Flow around a cylinder</b>	<b>7</b>
3.1 Flow regions . . . . .	7
3.2 Boundary layers and separation . . . . .	7
3.3 Flow regimes around a cylinder with various fixed ranges of $Re$ . . . . .	10
3.3.1 Vortex shedding . . . . .	11
3.3.2 Forces on a cylinder . . . . .	12
3.4 Flow around a cylinder in oscillatory flows . . . . .	13
3.4.1 Parameters and flow regimes . . . . .	13
3.4.2 Morison's equation . . . . .	16
3.5 Flow around a step cylinder . . . . .	16
<b>4 Governing equations and numerical method</b>	<b>21</b>
4.1 Mass conservation . . . . .	21
4.2 Momentum conservation . . . . .	21
4.3 The Navier–Stokes equations . . . . .	21
4.4 The solution algorithm . . . . .	22
<b>5 Numerical step-up</b>	<b>26</b>
5.1 Computational domain and gird . . . . .	26
5.2 Boundary conditions . . . . .	28
5.3 Validity of the numerical code MGLET . . . . .	30
5.3.1 Validation of $C_D$ and $C_M$ . . . . .	31

---

5.3.2	Validation of Honji vortices . . . . .	31
5.4	Convergence test . . . . .	36
<b>6</b>	<b>Results and discussion</b>	<b>39</b>
6.1	Flow development at parameters $KC = 2.8$ and $\beta = 80$ for large cylinder . . . . .	39
6.2	Appearance process of Honji vortex . . . . .	42
6.3	Merging process of Honji vortex . . . . .	44
<b>7</b>	<b>Discussion</b>	<b>49</b>
<b>8</b>	<b>Conclusion</b>	<b>51</b>
	<b>Bibliography</b>	<b>52</b>

---

## List of Figures

1	Stokes number versus Keulegan–Carpenter number. Reprinted from Sarpkaya [8]. . . . .	3
2	Velocity distribution in the case of a flow around a cylinder. Reprinted from Tec-science [20]. . . . .	8
3	The limiting value of KC number when the flow separation occurs. Reprinted from Faltinsen [21]. . . . .	9
4	Regimes of flow around a smooth, circular cylinder in steady current. Reprinted from Sumer [22]. . . . .	10
5	Shedding of vortex. Reprinted from Sumer [22]. . . . .	11
6	Strouhal number for a smooth circular cylinder. Reprinted from Sumer [22]. . . . .	12
7	Drag and lift force coefficient. Reprinted from Sumer [22]. . . . .	13
8	Flow regime for oscillatory flow around an cylinder and streaklines. Reprinted from Elston et al. [23], Zhao et al. [24] and Tong et al. [25]. . . . .	14
9	Flow regime B for oscillatory flow around an cylinder and streaklines. (a) is plane view of flow in the (y,z)-plane and (b) is plane view of flow in the (x,z)-plane. Reprinted from Elston et al. [23], Zhao et al. [24] and Tong et al. [25]. . . . .	15
10	Different types of vortices near the step cylinder. Reprinted from Dunn [19]. . . . .	17
11	Sketch of vortex lines and vortex linkages in direct mode(large cylinder $Re_L = 76$ , small cylinder $Re_S = 57$ ). Reprinted from Lewis and Gharib. [16]. . . . .	18
12	Sketch of vortex lines and vortex linkages in indirect mode(large cylinder $Re_L = 99$ , small cylinder $Re_S = 56$ ). Reprinted from Lewis and Gharib. [16]. . . . .	18
13	Vortex-shedding patterns from the step cylinder(large cylinder $Re_L = 156$ , small cylinder $Re_S = 79$ ). Reprinted from Dunn [19]. . . . .	19
14	Staggered arrangement of the variables in grid. Dashed line: momentum cell for u-velocity. Reprinted from Manhart [31]. . . . .	22
15	Treatment of the immersed boundary. Reprinted from Jiang [32]. . . . .	23
16	The coordinate system and computational domain. . . . .	26
17	Multi-level grids in the (x, z)—plane at $y/D = 0$ . The level of boxes are illustrated with the blue line arrows and numbers. Numbers 1 to 5 represent the coarsest boxes to the finest grid cells. . . . .	27
18	Time series of the maximum CFL criterion. (a) The CFL criterion from 0-40T (b) The CFL criterion from 365T-400T. . . . .	28
19	Comparison between theoretical and simulative fluid velocity $u$ at two corner points on inlet(black solid line) and outlet(red dash line) in case A. The theoretical sinusoidal velocity $u$ is illustrated by green dash line. (a) shows one peak of the velocity $u$ and (b) shows zoomed in velocity $u$ at the peak . . . . .	30
20	Comparison between theoretical and simulative fluid velocity $u$ at two corner points on inlet(black solid line) and outlet(red dash line) in case B. The theoretical sinusoidal velocity $u$ is illustrated by green dash line. (a) shows one peak of the velocity $u$ and (b) shows zoomed in velocity $u$ at the peak . . . . .	30
21	Temporal and spatial evolution of the spanwise velocity component $w$ . (a) shows $w$ along the line $x/D = 0$ , $y/D = 0.52$ and (b) shows $w$ along the $x/D = 0$ , $y/D = -0.52$ . . . . .	32

---

22	Temporal and spatial evolution of the axial velocity component $w$ . (a) and (b) are reprinted from Jiang [36] and (c) is reprinted from An [14]. . . . .	32
23	Vorticity isosurfaces around the cylinder when $KC = 2, \beta = 200$ and at time $t/T = 120$ . (a-c) are the components $\omega_x = \pm 1, \omega_y = \pm 1$ and $\omega_z = \pm 1$ respectively. . . . .	33
24	Vorticity isosurfaces around the cylinder when $KC = 2, \beta = 200$ and at time $t/T = 220$ . (a-c) are the components $\omega_x = \pm 1, \omega_y = \pm 1$ and $\omega_z = \pm 1$ respectively. . . . .	33
25	Vorticity isosurfaces around the cylinder when $KC = 2, \beta = 200$ and at time $t/T = 220$ . (a-c) are the components $\omega_x = \pm 1, \omega_y = \pm 1$ and $\omega_z = \pm 1$ respectively. Reprinted from An [14]. . . . .	34
26	Vorticity isosurfaces of x component ( $\omega_x = \pm 1$ ) around the cylinder when $KC = 2, \beta = 200$ and at time $t/T = 220$ . Reprinted from Yang [42]. . . . .	34
27	The crosssection of the Honji vortices in (y,z)-plane at $x/D = 0$ . Reprinted from Jiang [36]. . . . .	35
28	Streamwise vorticity distribution in the (y,z)-plane at $x/D = 0$ . (a) $t = 240$ , (b) $t = 440$ . . . . .	35
29	The phase average velocity $u/U_a$ at streamwise location $x/D = 0.6D$ , spanwise location $z/D = -6.2$ calculated using properties listed in Table 5 and using parameter values $KC = 2.8, \beta = 80$ with time range from $t = 365T$ to $t = 465T$ . The sub figures (a), (b), (c), (d) are results of domain, time step, grid and geometry convergence tests, respectively. The phase angle for each case is (a) $\theta = 57.85^\circ$ , (b) $\theta = 101.83^\circ$ , (c) $\theta = 101.83^\circ$ , (d) $\theta = 57.85^\circ$ . . . . .	37
30	The phase average velocity $v/U_a$ at streamwise location $x/D = 0.6D$ , spanwise location $z/D = -6.2$ calculated using properties listed in Table 5 and using parameter values $KC = 2.8, \beta = 80$ with time range from $t = 365T$ to $t = 465T$ . The sub figures (a), (b), (c), (d) are results of domain, time step, grid and geometry convergence tests, respectively. The phase angle for each case is (a) $\theta = 57.85^\circ$ , (b) $\theta = 101.83^\circ$ , (c) $\theta = 101.83^\circ$ , (d) $\theta = 57.85^\circ$ . . . . .	38
31	Temporal and spatial evolution of the spanwise velocity component $w/U_m$ . (a) shows $w/U_m$ along the line $x/D = 0, y/D = 0.52$ and (b) shows $w$ along the $x/D = 0, y/D = -0.52$ . . . . .	40
32	Zoomed-in temporal and spatial evolution of the spanwise velocity component $w/U_m$ along the line $x/D = 0, y/D = 0.52$ . . . . .	41
33	Vorticity isosurfaces $\omega_y = \pm 0.1$ around the cylinder at time $t = 760.06s$ , in the range $-3 < z/D < 0$ . . . . .	42
34	Vorticity isosurfaces $\omega_y = \pm 0.1$ around the cylinder at time $t = 807.66s$ , in the range $-3 < z/D < 0$ . . . . .	43
35	Vorticity isosurfaces $\omega_y = \pm 0.1$ around the cylinder at time $t = 838.46s$ , in the range $-3 < z/D < 0$ . . . . .	43
36	Vorticity isosurfaces $\omega_y = \pm 0.1$ around the cylinder at time $t = 857.71s$ , in the range $-3 < z/D < 0$ . . . . .	44
37	Vorticity isosurfaces $\omega_y = \pm 0.1$ around the cylinder at time $t = 919.66s$ , in the range $-3 < z/D < 0$ . . . . .	44
38	Vorticity isosurfaces $\omega_y = \pm 0.1$ around the cylinder at time $t = 776.51s$ , in the range $-7 < z/D < -3$ . . . . .	45
39	Vorticity isosurfaces $\omega_y = \pm 0.1$ around the cylinder at time $t = 787.71s$ , in the range $-7 < z/D < -3$ . . . . .	46

---

---

40	Vorticity isosurfaces $\omega_y = \pm 0.1$ around the cylinder at time $t = 790.51s$ , in the range $-7 < z/D < -3$ . . . . .	46
41	Vorticity isosurfaces $\omega_y = \pm 0.1$ around the cylinder at time $t = 798.91s$ , in the range $-7 < z/D < -3$ . . . . .	47
42	Vorticity isosurfaces $\omega_y = \pm 0.1$ around the cylinder at time $t = 807.66s$ , in the range $-7 < z/D < -3$ . . . . .	47
43	Vorticity isosurfaces $\omega_y = \pm 0.1$ around the cylinder at time $t = 821.66s$ , in the range $-7 < z/D < -3$ . . . . .	48
44	Vorticity isosurfaces $\omega_y = \pm 0.1$ around the cylinder at time $t = 832.51s$ , in the range $-7 < z/D < -3$ . . . . .	48

---

## List of Tables

1	Detailed mesh information. . . . .	28
2	Two different boundary conditions tested in the domain. . . . .	28
3	Domain information and flow property. . . . .	31
4	A collection of relevant studies of the case $KC = 2, \beta = 200$ . . . . .	31
5	Details of convergence tests . . . . .	38
6	Details of geometries and parameters . . . . .	39
7	Oscillatory period number of occurrence of appearance and merging of Honji vortex . . . . .	42

---

## Nomenclature

$\beta$	Stokes number
$\epsilon$	The mean energy dissipation rate
$\nu$	Kinematic viscosity of fluid
$\bar{u}$	Mean flow velocity
$\Phi$	Velocity spectrum tensor
$\rho$	Density
$a$	Amplitude of the fluid particles motion
$C_D$	Drag coefficient
$C_L$	Lift coefficient
$C_M$	Mass coefficient
$D$	Cross section diameter of cylinder
$F_D$	Total in-line force
$F_f$	In-line friction force
$F_p$	In-line pressure force
$f_v$	Vortex shedding frequency
$KC$	Keulegan–Carpenter number
$KC_H$	Approximated Hall line
$KC_h$	Hall line
$KC_{cr}$	Critical stability line
$p$	Pressure
$r$	Cross section radius of the cylinder
$Re$	Reynolds number
$St$	Strouhal number
$T$	period of the oscillatory flow
$U$	Free-stream velocity
$U_a$	Velocity amplitude of the oscillatory flow
$\tau$	Wall shear stress



---

# 1 Abstract

The structures with a similar shape to the step cylinder, which consists of one small-diameter cylinder at the top and a coaxial large-diameter cylinder in the middle, are widely used in marine engineering applications. A numerical simulation of the oscillatory flow around a step cylinder has been performed. In this simulation, by adjusting the values of diameter ratio to 1.8,  $KC$  number to 2.8, and  $\beta$  to 80, the flow around the small cylinder is set in regime A, while the flow around the large cylinder is set in regime B. A powerful in-house code MGLET (Multi Grid Large Eddy Turbulence) is used as the numerical solver. All of the CFD simulations are performed on the supercomputer Betzy.

A numerical simulation of oscillatory flow around a circular cylinder with parameters  $KC = 2$  and  $\beta = 200$  is carried out to assess the validity of the numerical code MGLET. The simulation results of Morison's force coefficients  $C_D$  and  $C_M$ , the flow patterns, and spacing between Honji vortices are consistent with previous studies which prove that the numerical code MGLET is suitable for the final simulation. To validate the important CFD setup parameters, a series of convergence studies, e.g., the mesh resolution test, the computational domain size test, the time step test, and the geometry test are performed.

In the final simulation, the evolution of the flow in regimes A and B around the small and large cylinder, respectively, is visualized by using the time history of the relative axial (spanwise) velocity  $w/U_m$ . The results show that the three-dimensionality due to the appearance of the step slightly affects the flow patterns behind the small cylinder, while it has a great impact on the flow around the large cylinder. The flow behind the small cylinder remains its two-dimensional features as it has in regime A around a uniform cylinder. The three-dimensionality near the step leads to instability in Honji vortices around the large cylinder in regime B and finally induces two kinds of long-term phenomenon: appearance and merging of Honji vortex pair.

The appearance and merging process of Honji vortex is presented by vorticity isosurfaces  $\omega_y = \pm 0.1$ . The cause of Honji vortex generation in the present study is instability in Honji vortices due to the lack of half vortex pair. In the present study, a total of 20.5 or 21.5 pairs of Honji vortex are distributed along the axis of the large cylinder. As time goes by, new vortices appear in a pair below the step. One part of the newly generated vortex pair and the already existing Honji vortex form a new pair. The other vortex of the newly generated vortex pair is left alone and continues to induce instability in the rest of the Honji vortices. The merging process of the Honji vortex shows different features on the negative and positive  $y$  sides of the large cylinder. On the negative side, as two neighbouring Honji vortex pairs move toward each other, the negative part of the upper pair and the positive part of the lower pair cancel each other completely and the remaining parts of the two vortex pairs form a new vortex pair. On the positive side, as the upper and lower vortex pairs keep squeezing the middle vortex pair, the middle vortex pair finally disappear due to the cancellation and suppression effect.

---

## 2 Introudction

Circular cylinders are one of the most commonly used structures in the coastal and offshore industries. The cylindrical shapes can be encountered in subsea risers developed for transportation, pipelines on the seabed, etc. However, when the vortex shedding frequency is close to the natural frequency of the circular cylinder structures, the vortex-induced vibration (VIV) can be induced and it may cause the fatigue failure of these structures.

In recent years, the suppression of VIV responses of a riser with staggered buoyancy elements has received more and more attention. Various strategies have been proposed, and among them the passive geometrical modifications to cylinder geometry, such as a step, are commonly used to change the spanwise coherence of vortex shedding. Thus, it is interesting to understand the development of oscillatory flow around a step cylinder.

### 2.1 State of the art

#### 2.1.1 Oscillatory flow around a circular cylinder

The vortex motions and induced loads on a circular cylinder placed in a sinusoidally oscillating flow are different than one in a steady flow. In the last few decades, many investigations are performed into the flow structure developments around a circular cylinder vibrating in simple harmonic in-line motion in a still fluid, or equivalently into the flow structure generated by a circular cylinder in unidirectional oscillatory flow. These flows draw people's attention because their results are the idealized portrayals of loads on cylindrical structures immersed in waves.

The in-line force acting on the cylinder in oscillatory flow is predicted by a semi-empirical equation (Equation (24)) introduced by Morison [1]. The inertia coefficient ( $C_M$ ) and drag coefficients ( $C_D$ ) in the Morison equation have been experimentally calculated from laboratory and full-scale researches. Keulegan and Carpenter [2] investigated  $C_M$  and  $C_D$  of a cylinder horizontally fixed below standing waves, and found these two coefficients can be correlated with the Keulegan–Carpenter number ( $KC$ ). Later on, Sarpkaya [3] has found that  $C_M$  and  $C_D$  are not only dependent on  $KC$ , but also on Stokes number ( $\beta$ ) which is proportional to  $Re$ . From there on, many studies have presented that the force acting on the circular cylinder, the flow structures and generation and shedding of vortices are highly relative to these three parameters ( $KC, Re, \beta$ ).

Williamson [4] carried out experiments to investigate the motions of vortices around single cylinder in sinusoidal flow giving a constant  $\beta$  at 730 and  $KC$  values up to 35. The detailed flow visualizations shown in his study present several repeatable patterns of vortex shedding and show that the process of pairing of vortices from a previous half cycle with those in a present half cycle is fundamental to all the patterns. He has also shown that the vortex motions were related to the induced forces, and has found an expression for r.m.s in-line force coefficients ( $C_{F_{rms}}$ ) as a function of  $KC$ .

Tatsuno and Bearman [5] performed experiments using a tank filled with water where a circular cylinder performing sinusoidal oscillations. Their purpose is to investigate in detail of the flow structures for  $KC < 15$  and for  $\beta < 160$ . Classified by flow separation, the generation of vortices and vortex shedding, eight different flow regimes (A\*, A, B, C, D, E, F, and G) have been identified (shown in Figure 8). These flow regimes are depending on  $KC$  and  $\beta$ , or equivalently, on  $KC$  and  $Re$  and most of them have a spatially periodic patterns. Among these flow regions, only regimes A\* and A are two-dimensional symmetric, and only in regime A\* there is no vortex shedding. However, it is very difficult to identify the critical value of  $KC$  and  $\beta$  between regime A\* and regime A. Because, in the regime A, the shed vortices are cancelled by mixing with vorticity of opposite sign in the cylinder boundary layer and do not survive into far field.

The flows in regimes B to G are three-dimensional, and in these regimes, vortex structures develop along the direction of the cylinder's axis. Among these regimes, the flow structure in regime B differs great from other regimes. By doing a sequence of experiments of oscillating circular cylinder immersed in water with small  $KC$  values ( $1.3 < KC < 3.9$ ) and  $\beta$  values ( $70 < \beta < 700$ ), Honji [6]

investigated the flow structure in regime B in detail and observed mushroom-like flow structures distributed evenly along the cylinder in spanwise direction. As the flow structure develop, these mushroom-like vortices result a flow structure in a plane parallel to the oscillatory plane, which is named as 'streaked flow'. Furthermore, Honji [6] found that these mushroom-like vortices are not developed due to flow separation, but due to an instability (caused by the centrifugal forces with the varying strength) in the boundary-layer flow. This three-dimensional flow instability is called Honji instability and is associated with the transition from two-dimensional flow in regime A to three-dimensional flow in regime B.

Later on, Hall [7] carried on the investigation of three-dimensional instability of the boundary layer on the oscillating cylinder in a viscous fluid. Hall simplified the problem by assuming that the oscillation period is very small (with very small  $KC$  and large  $\beta$ ), and this stability problem only depending on a radial variable and time. His study led to the result given by

$$KC_h = 5.778\beta^{-1/4} \left(1 + 0.205\beta^{1/4} + \dots\right) \quad (1)$$

This  $KC_h - \beta$  relationship is called the 'Hall line', which separates the regime of a featureless two-dimensional flow and an unstable region. However, even this simplified formula provides great results on high  $\beta$  region, the 'Hall line' itself does not represent a critical line between a region of absolute stability and a region of three-dimensional instabilities.

In a later study, Sarpkaya [8] conducted detailed experiments to observe the three-dimensional instabilities over the parameter ranges  $0.02 < KC < 1.0$  and  $10^3 < \beta < 1.4 \times 10^6$ . In his experiments, Sarpkaya first investigated the mushroom-shaped coherent structures in narrow regions near the Hall line(Figure 4). Based on video viewing and the information obtained from it, Sarpkaya decomposed the mushrooms into two structures: two weak, counter-rotating vortices and a periodically appearing stem. The mushrooms appeared through a number of oscillations, and once the mushrooms came in to existence, the stems of them disappeared and stopped draining boundary fluid into the mushrooms. In this case, the mushrooms were not connected to the cylinder, but neither did them move away form the cylinder in the direction of oscillation. In fact, the mushrooms moved toward the cylinder, while the vortices decreased due to the cut-off of supply of vorticity and diffusion.

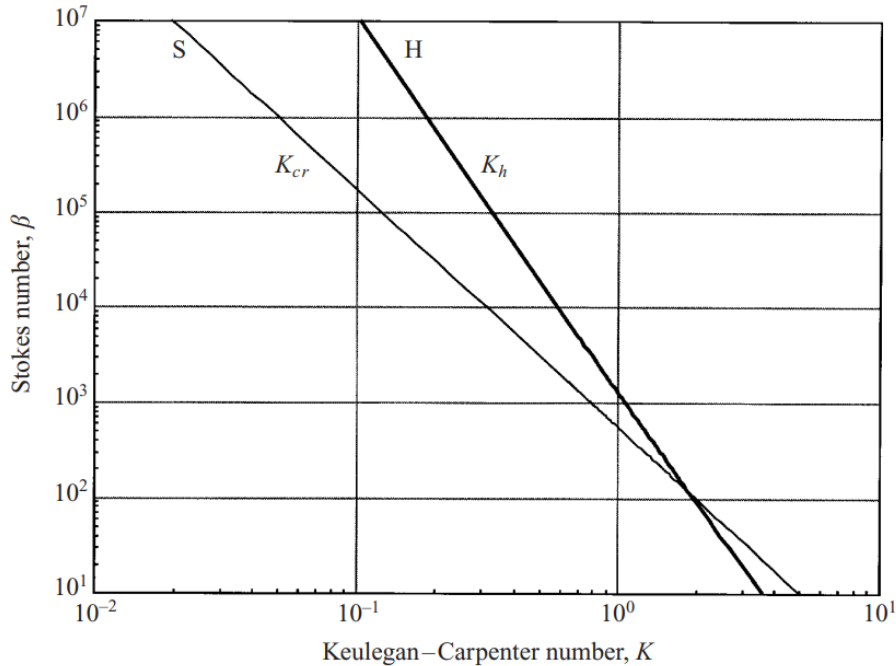


Figure 1: Stokes number versus Keulegan-Carpenter number. Reprinted from Sarpkaya [8].

---

In the same study, Sarpkaya also discussed the start of three-dimensional instability near the critical  $K_{cr}$  and the quasi-coherent structures(QCS), which had weaker instability than the Honji instability. Based on the experimental results, the  $KC - \beta$  plane was divided into three flow regimes by two lines: Hall line(H) and Sarpkaya line(S) given by

$$KC_{cr} = 12.5\beta^{-2/5} \quad (2)$$

In Figure 4, the region to the left of S is stable and no discernible flow structures around the cylinder during oscillation. Between S and H, there is an unstable transition region where many forms of quasi-coherent structures occur. Then near the Hall line, those quasi-coherent structures tends to become coherent mushroom-like structures. To the right of the Hall line, instabilities take many forms and fall due to the influence of separation and turbulence.

At early stage, confined to computing resources, most of previous numerical investigations focused on two-dimensional flows. In reality, the two-dimensional flows around a circular cylinder in oscillating flow hardly exist. However, in many studies, the two-dimensional flow model have been provided that, as along as the flow model in the weakly three-dimensional flow regime, it is able to reproduce the important features observed in three-dimensional flows Justesen [9], Dütsch et al. [10], Lin et al. [11], Nehari et al. [12] performed a numerical investigation of the oscillating flow around a circular cylinder using both a three-dimensional and a two-dimensional model at regimes A, D and F. They found that the two-dimensional features like the asymmetric motion in the sectional plane at regimes D and F, as well as switching from a pattern to its mirror-image are not affected by three-dimensional effects. These inherent features of vortex are considered to be caused by a two-dimensional instability and can be simulated using pure two-dimensional models. Dütsch et al. particularly studied the flow pattern in regimes A, E and F using experiments and numerical predictions. Their results shown that, even with the weak stability in the flow pattern, good agreement was found between experimental results and numerical predictions. However, despite the weak three-dimensional effects on flow features, Nehari et al. [12] found that the three-dimensional effects delayed the switching phenomenon in regime D, and caused different transversal component of the force on the cylinder.

Numerical simulations of the Honji instability have been performed since Honji's study. Zhang and Dalton [13] focused on the three-dimensional development of the flow at  $\beta = 196$  and  $KC$  increases from 1 to 4. They presented the transition process from two-dimensional laminar flow to three-dimensional turbulent flow, and they found the mushroom-shaped structures observed by Honji. To get further understanding of the Honji instability, An et al. [14] conducted numerical simulations of the oscillatory flow around circular cylinder at  $KC = 2$  and  $100 < \beta < 600$ . In their project, detailed flow structure of Honji vortices and the evolution process of vortices over one cycle of oscillation were presented. They also found that the spacing between adjacent vortices is sensitive to the value of  $KC$ , but hardly relative to the value of  $\beta$ .

### 2.1.2 Flow around a step cylinder

The cylindrical geometries are widely used in engineering applications, but when the  $Re$  is sufficiently large, the vortex shedding might occur and the cyclic vortex force will cause vibrations of the structures. Those such vibrations are called vortex-induced vibrations (VIV) and cause the fatigue damage to structures. Over the past decades, various experimentally and numerically investigations for suppressing VIV are done by researchers and engineers. Theoretically, the VIV suppression methods should reduce the spanwise coherence of vortices and eliminate the drag forces and the magnitudes of the fluctuating lift on cylindrical structures. Among all these VIV suppression solutions, the passive geometrical modifications to cylinder geometry such as helical strakes, splitter plates and step changes are commonly used to change the spanwise coherence of vortex shedding.

There are considerable studies of vortex wake on the vortex shedding of the step cylinder geometry. The flow behind a step cylinder at the  $Re$  of  $8 \times 10^4$  was initially investigated by Ko et al. [15]. In their experiments, they analyzed the pressure fluctuations in the wake of a step cylinder and

---

they associated it to the effect of the discontinuity on the vortex wakes shed from the cylinders. They also found that the spanwise position where the two-dimensionality of the vortex wake ends depends on the diameter of the cylinder.

The three-dimensionality is likely to occur in which the velocity or diameter for the cylinder varies along spanwise direction. Lewis et al. [16] studied this three-dimensionality in wakes of step cylinders with several diameter ratios  $1.14 < D/d < 1.76$  at a range of Reynolds numbers  $35 < Re < 200$ . Based on the visualizations of flow and frequency analysis, they found two types of vortex interaction: direct and indirect modes of interaction. The occurrence of these two different modes and the transitional mode between them is a function of the Reynolds number ( $Re$ ) and the diameter ratio ( $D/d$ ). When  $D/d < 1.25$ , the direct mode appears and vortices shed from the small and large cylinders with two different shedding frequencies  $f_S$  and  $f_L$ , respectively. These two types of distinct vortices interact with each other in a narrow zone called interface. When these two different vortices are in phase, they will connect across the interface. Otherwise, the one by one connection will be broken and at least one misconnection will happen and form a hole at the interface. When  $D/d > 1.55$ , the indirect mode occurs and the two dominating vortices link to each other in the interface zone along a line that is perpendicular to the cylinders' axis. Furthermore, a third frequency  $f_N$  can be found in a region called modulated zone, near the interface behind the large cylinder. This modulated zone acts as a buffer zone, and in the modulated zone connections between vortices are cut by inclined interfaces which appear at the beat frequency ( $f_L - f_N$ ).

Lots of studies have been done based on these distinct shedding frequencies. In his study, Norberg [17] found that the vortex shedding behind the larger cylinder was strongly affected by the discontinuity in diameter which was caused by the presence of the step. However, the flow behind the small cylinder was nearly unaffected by the discontinuity in diameter. Chua et al. [18] conducted an experiment to measure pressure distributions and velocity in the far wake of a step cylinder. They found that the large cylinder tended to suffer greater drag, and the difference of drag between the large and small cylinders affected the flow field behind the step cylinder, especially the downstream wake behind the large cylinder. The wake behind the small cylinder was structured, while there are twin spectral peaks in the wake of the large cylinder, which are associated with the two distinct vortex shedding frequencies from the large and small cylinders.

Dunn [19] investigated the vortex shedding patterns and interactions of vortices near the step cylinder. In his project, he named the cells behind the small, large cylinders and step, respectively, the *S-cell*, *L-cell* and *N-cell*. His observations agreed with previous researches. With low  $Re$  ( $Re = 79$ ), the S-cell vortices were laminar and remained parallel to each other even in the far region from the step. In contrast, even for low  $Re$  ( $Re = 152$ ), due to the presence of the step, the L-cell vortices were interrupted spanwise, and therefore three-dimensionality appeared and made the L-cell vortices hardly remain their forms as they moved downstream. Dunn found that both S-cell vortices and N-cell vortices were inclined to the axis of the cylinder, but in an opposite way. For S-cell vortices, the part away from the step was closer downstream than the part near to the step. On the other hand, the N-cell vortices started to shed at the far spanwise location downstream from the step. The pressure difference between large and small cylinders is the reason for this opposite inclination. The pressure of the small cylinder is greater than the pressure of the large cylinder, and this pressure difference then leads the small cylinder wake to move over the step, down to the large cylinder wake. Finally, this fluid downwash causes the early vortex shedding of S-cell close to the step and suppresses the shedding of L-cell vortices.

## 2.2 Motivation

Cross-flow around cylinders is commonly observed in many marine engineering applications. One of the most commonly used geometries in marine engineering is the uniform circular cylinder, which has been investigated in many studies over the last decades. In contrast, less research has been done involving more complex cylindrical geometries, for example, step cylinders. Although, some investigations about uniform flow past a step cylinder have been done, and wake development is found to be similar to that of a uniform circular cylinder, the development of oscillatory flow around a step cylinder has not been investigated in detail.

---

Honji [6] first observed the three-dimensional instability in the form of mushroom-shaped coherent structures distributed along a uniform circular cylinder in oscillatory flow. This three-dimensional flow instability is called Honji instability and is associated with the transition from two-dimensional laminar flow to turbulent flow in a specific range of  $KC$  and  $\beta$ . On the other hand, the three-dimensionality in wake behind a cylinder is commonly found in which discontinuities in velocity or diameter exist. These discontinuities can cause change of shedding frequency along spanwise direction. Thus, It is interesting to combine the Honji instability with the three-dimensionality caused by appearance of step and investigate how it affects the mushroom-shaped coherent structures.

## 2.3 Structure of the thesis

The structure of rest of thesis is as follows:

**Chapter 3** presents an overview of the basic theory regarding flow around a cylinder, flow around a cylinder in oscillatory flows, flow around a step cylinder and some literature reviews regarding generating and merging process of Honji vortex.

**Chapter 4** gives a brief introduction to the governing equations and solution algorithm of the MGLET solver which is used in this studying.

**Chapter 5** gives the details of numerical step-up of the simulation. The computational domain and grid, the boundary conditions, the validity of the numerical code MGLET and the convergence test will be described.

**Chapter 6** presents the results obtained from the simulation of oscillatory flow around a step cylinder. The development of flow, the appearance and merging process of Honji vortex will be included.

**Chapter 7** shows a discussion of the main results obtained in the present thesis.

**Chapter 8** includes a conclusion of this study.

---

## 3 Flow around a cylinder

The oscillating flow around circular cylinder have complex features which are highly relative to the shape and size of the cylinder, the fluid properties, the environment, etc. Among those features, the three-dimensional instability is important because it could make the recognizable two-dimensional flow transform into the chaotic turbulent flow. The mushroom-shaped Honji vortices is associated with the transition from two-dimensional flow to three-dimensional flow, and thus can be used as a sign of occurrence of the three-dimensional instability. For cylinder having spanwise discontinuity in diameter, for example a step cylinder, the three-dimensional phenomena are even more complicated. In this chapter, the basic concepts of these main features will be presented.

### 3.1 Flow regions

The free stream flow could be disturbed by the presence of the circular cylinder and the disturbed flow field around the circular cylinder are divided into four regions:

- One narrow region of stagnation region in front the cylinder.
- Boundary layers attached to the surface of the body.
- Two regions of displaced and accelerated flow over and under the body.
- One downstream region called the wake.

The incoming flow is deflected and directed in different directions at the stagnation point on the cylinder in the stagnation region. The deflection of flow is very fast and lead to the unexpectedly high fluctuations in flow velocity. This kind of highly fluctuating velocity could cause unstable problems but significantly increases local heat transfer.

Unlike the boundary layer on a flat plate, the boundary layers around the cylinder are exposed to the favourable pressure gradient on the front side of the cylinder and to the adverse pressure gradient on the back side. As the boundary layers travel in the adverse pressure, it could detach itself from the surface of cylinder and develops downstream as free shear layers.

The two sidewise region of the displaced flow are not fully investigated as the other three regions. However, the sidewise regions are much larger then the cylinder and are easily affected by the walls or other boundaries around them. As a result, before making a numerical simulation, the size of domain should be large enough to eliminate the blockage effect.

The wake region behind a cylinder is investigated by many researches focusing on different aspects. Here, the flow structures in the wake behind a step cylinder are analyzed.

The Reynolds number ( $Re$ ) is one of the crucial dimensionless quantities in fluid mechanics.  $Re$  is the ratio of inertial forces to viscous forces and is used to predict the state of flow (laminar, transitional, or turbulent). The Reynolds number of the flow around a circular cylinder is defined as:

$$Re = \frac{DU}{\nu} \quad (3)$$

Where  $D$  is the cross-section diameter of the cylinder,  $U$  is the free-stream velocity and  $\nu$  is the kinematic viscosity.

### 3.2 Boundary layers and separation

When a viscous fluid flows over a impermeable surface, the molecules near the surface are brought to rest by the shear stress and adhere to the wall, in another word, the velocity at any point on the

wall is zero. The adjacent layer are also slow down, but to a lower and lower extent. The extent of slowing down depends on the value of the viscosity and is found limited to a thin layer near the surface which are called boundary layer. The fluid velocity rises rapidly and asymptotically from zero at the wall to main-stream value which is not influenced by friction. As a result, in the boundary layers, even the viscosity itself is very small, it can not be negligible. Furthermore, this non-negligible viscous term in the equation of motion makes the simplified equations, which are only valid for potential theory, become unable to be used in the boundary layer.

The boundary layer thickness  $\delta$  is defined as the distance from the wall to the point where the flow velocity become equal to 99% of the free stream value. The laminar boundary layer thickness around a cylinder is relative to the  $Re$  and the cylinder diameter(D). The thickness values is approximated as:

$$\delta = \frac{D}{\sqrt{Re}} \quad (4)$$

The flow in the boundary layer can be either laminar or turbulent depending on the value of the  $Re$ . For lower  $Re$ , the boundary layer is laminar and the streamwise velocity changes uniformly as one moves away from the wall. As a consequence, the laminar flow have small velocity gradient and generate less skin friction drag. However, as the flow continues moving backward, the laminar boundary layer thickness increases and the boundary layer tends to be less stable, and thus the motion within it easily becomes disturbed. As the irregularities of the flow develop, the laminar flow breaks down and transitions to a turbulent flow over a small area called transition region. For a turbulent boundary layer flow, the thickness is larger while the velocity gradient is steep towards the wall, causing a greater frictional resistance. On the another hand, the disturbed flows, such as swirls, contain more energy and prevent the boundary layer lift off and delay the boundary layer separation.

The boundary layer velocity profile is highly dependent on the external acceleration and pressure gradient, which are generally based on the body shape and surface curvature, as seen in Figure 2. For a circular cylinder, the tangential pressure gradient, which accelerates the flow, called favorable pressure gradient ( $\frac{dp}{dx} < 0$ ) appears on the front side and will not cause the boundary layer separation. While the freestream pressure increasing in the direction of flow, known as adverse pressure ( $\frac{dp}{dx} > 0$ ), causes the flow to slow down. When the velocity gradient at the wall approaches zero ( $\frac{\partial u}{\partial y} = 0$ ), the kinetic energy of the fluid is not enough to overcome the pressure. The flow will stop move tangentially, but lift off, detach from the surface and push the streamlines away from the surface. This phenomenon is known as flow separation.

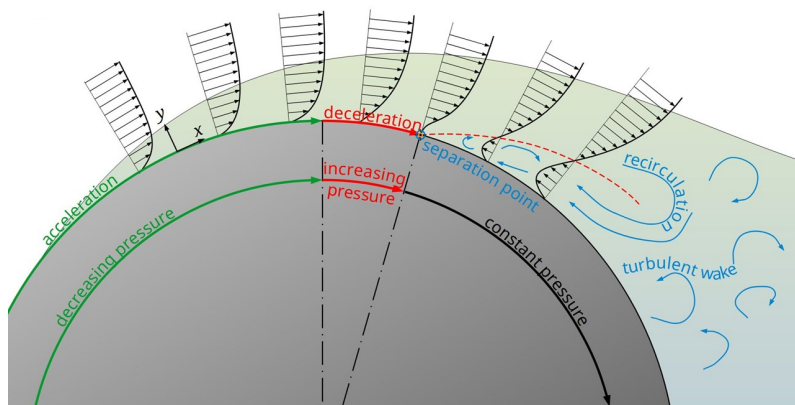


Figure 2: Velocity distribution in the case of a flow around a cylinder. Reprinted from Tec-science [20].

It should be noticed that the adverse pressure is not the only reason cause the flow separation. At



the sharp corners, the flow will separate naturally. At the corner, due to lack of external pressure gradient which push the flow turn around, the boundary layer could stay attached and separates.

In his book, Faltinsen [21] determine the location where the flow separation occurs for subcritical flows. The two-dimensional circular cylinder are placed in a high  $Re$  flow while the boundary layer on the body is assumed to be thin and laminar.

The ambient flow velocity  $U_\infty$  is defined as:

$$U_\infty = U_M \sin(\omega t - \alpha) + U_c \quad (5)$$

Where  $U_M$ ,  $U_c$  are constants,  $\omega$  is the circular frequency of oscillation and  $\alpha$  is a phase angle.

The initial vorticity is set to be zero and the flow is analysed until the first maximum ambient flow velocity is reached. By solving a potential flow problem outside the boundary layer, the tangential fluid velocity ( $U(x, t)$ ) at the outside boundary layer is:

$$U(x, t) = (U_M \sin(\omega t - \alpha) + U_c) \Phi(x) \quad (6)$$

Then the shear stress on the body is written as

$$\frac{\partial u}{\partial y} = \sqrt{\frac{\omega}{v} U_M \Phi(x) \left[ f_1 + \frac{U_M}{\omega} \frac{d\Phi(x)}{dx} \right] f_2} \quad (7)$$

Where  $f_1$  and  $f_2$  are functions of  $\frac{U_c}{U_M}$ ,  $\alpha$  and  $\omega$ , but are not relative to the body shape. for a circular cylinder:

$$\Phi(x) = 2 \sin\left(\frac{x}{R}\right) \quad (8)$$

Then the separation angles  $\pm|\theta_s|$  are defined as:

$$\theta_s = \frac{x_r}{R} = \cos^{-1} \left[ -\frac{f_1}{f_2} \frac{\pi}{2KC} \right] \quad (9)$$

However, the Equation (9) are only suitable for limiting range of value of  $KC$ . The limiting value of  $KC$  ( $KC_{lim}$ ) for separation to occur is a relative to  $\frac{U_c}{U_M}$  and should be great then 1.2 when  $\frac{U_c}{U_M} = 0$ , as shown in Figure 3. It should to be noticed that the results calculated by using Equation (9) do not depend on  $Re$ . This due to the assumption of laminar, high  $Re$  start up flow.

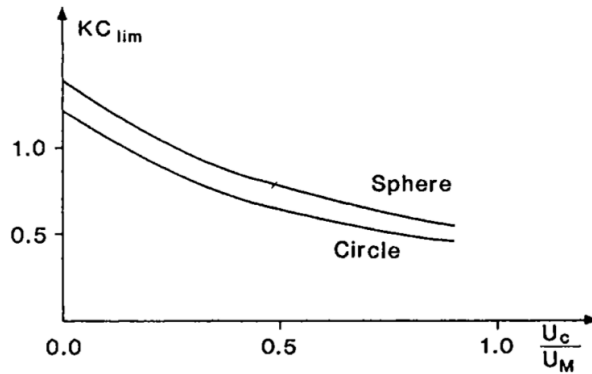


Figure 3: The limiting value of KC number when the flow separation occurs. Reprinted from Faltinsen [21].

### 3.3 Flow regimes around a cylinder with various fixed ranges of $Re$

From the beginning of development to the end of decay, the flow has an vast variation of regular and irregular patterns. These distinct flow structures are highly related to the  $Re$ , and each of them persists only over a certain range  $Re$ . As a result, the values of  $Re$  are used to specify the flow regimes (or flow patterns) around the cylinder. The Figure 4 below shows how the flow regimes around a circular cylinder change referred to different  $Re$ .


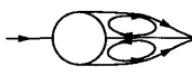


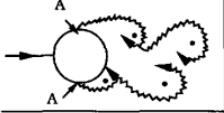
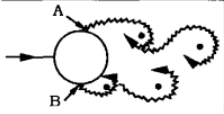
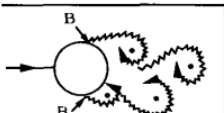
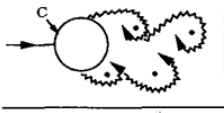
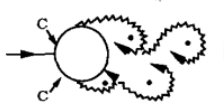
a)		No separation. Creeping flow	$Re < 5$
b)		A fixed pair of symmetric vortices	$5 < Re < 40$
c)		Laminar vortex street	$40 < Re < 200$
d)		Transition to turbulence in the wake	$200 < Re < 300$
e)		Wake completely turbulent. A: Laminar boundary layer separation	$300 < Re < 3 \times 10^5$ Subcritical
f)		A: Laminar boundary layer separation B: Turbulent boundary layer separation; but boundary layer laminar	$3 \times 10^5 < Re < 3.5 \times 10^5$ Critical (Lower transition)
g)		B: Turbulent boundary layer separation; the boundary layer partly laminar partly turbulent	$3.5 \times 10^5 < Re < 1.5 \times 10^6$ Supercritical
h)		C: Boundary layer com- pletely turbulent at one side	$1.5 \times 10^6 < Re < 4 \times 10^6$ Upper transition
i)		C: Boundary layer com- pletely turbulent at two sides	$4 \times 10^6 < Re$ Transcritical

Figure 4: Regimes of flow around a smooth, circular cylinder in steady current. Reprinted from Sumer [22].

As the  $Re$  starts to increase from 0 to 5, the flow attaches strongly to the surface of the cylinder and no separation occurs. Behind the cylinder, the trail of laminar shear layer is smooth and symmetric and does not generate a distinct wake. This kind of flow pattern are known as creeping flow and the flow regime are called non-separation regime.

Around  $Re = 5$ , the flow begins to separate, and close to the back of cylinder, a steady, symmetric and closed near-wake forms. The reverse velocity in the near-wake is lower than the free stream velocity, and thus the free shear layers could meet at the end of the near-wake.

For the range of  $Re > 40$ , the wake behind the cylinder becomes unstable, and vortices are shed alternately at either side of the cylinder at a particular frequency. This phenomenon is called

vortex shedding. When the vortex starts to shed, the vortex street is laminar, however as the further increase in  $Re$ , transition to turbulence occurs in the wake region. For  $Re$  over a vast range,  $300 < Re < 3 \times 10^5$ , this regime is known as the subcritical flow regime, in which the wake is completely turbulent while the boundary layer remains laminar.

The next flow regime is the critical flow regime where  $3 \times 10^5 < Re < 3.5 \times 10^5$ . In this regime, at one side of the cylinder, the boundary layer becomes turbulent at the separation point, while the boundary layer at the other separation point is still laminar. These two different types of the boundary layer at two separation points cause an asymmetry flow and thus induce a non-zero mean lift on the cylinder.

For  $3.5 \times 10^5 < Re < 1.5 \times 10^6$ , the boundary layer separation is turbulent on both sides of the cylinder, and the boundary layers transit to partly laminar and partly turbulent. This regime is called the supercritical flow regime. As the  $Re$  increases, one side of the boundary layer is completely turbulent over a range of  $1.5 \times 10^6 < Re < 4 \times 10^6$ , and then when  $4 \times 10^6 < Re$ , the boundary layer over the whole cylinder surface is turbulent.

### 3.3.1 Vortex shedding

For the range of  $Re > 40$ , at the rear side of the cylinder, the boundary layer over the cylinder surface will separate because of the adverse pressure gradient [22]. As mentioned before, there are a non-negligible amount of vorticity formed in the boundary layer. As the boundary layers detach from either side of the cylinder at the separation points, the vorticity is fed into the shear layer and force the shear layers roll up into vortices which rotate in the opposite direction. Due to instability caused by disturbances, these vortices are unstable and one vortex becomes larger than the other. The larger vortex continues to grow, and it eventually becomes strong enough to draw the smaller vortex across the wake. When the smaller vortex approach close to the larger vortex, the opposite vorticity in the smaller vortex interrupts the supply of vorticity to larger vortex. As consequence, the larger vortex forms to a free vortex, and then is converted downstream by the free stream flow. This phenomenon is called vortex shedding.

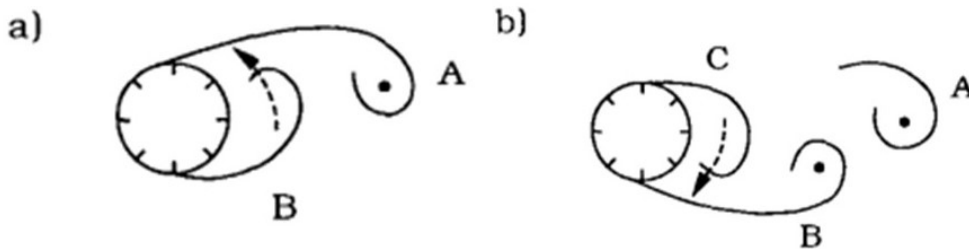


Figure 5: Shedding of vortex. Reprinted from Sumer [22].

The frequency at which vortex shedding takes place is related to the dimensionless Strouhal number:

$$St = \frac{f_v D}{U} \quad (10)$$

Where  $f_v$  is the vortex shedding frequency. It is clear that the Strouhal number number is a function of the Reynolds number. The Figure 6 illustrates how the  $St$  varies with the  $Re$ . The vortex shedding start at  $Re = 40$  and the shedding frequency  $St$  is around 0.1 which is smallest value around whole  $Re$  range. Then the  $St$  gradually increases and reach about 0.2 when  $Re$  is approximately 300. The  $St$  remains nearly constant throughout subcritical regime and a sudden jump in value of  $St$  at  $3 \times 10^5 < Re < 3.5 \times 10^5$ , which is the critical flow regime as mentioned before. The large increase in  $St$  is due to the delay of the separation. The separation points move downstream as the boundary layers become turbulent, and then the vortices at the both side of

cylinder could interact much faster than in the subcritical regime. This faster incrtation rate would lead to a sudden jump in the vaules of  $St$ .

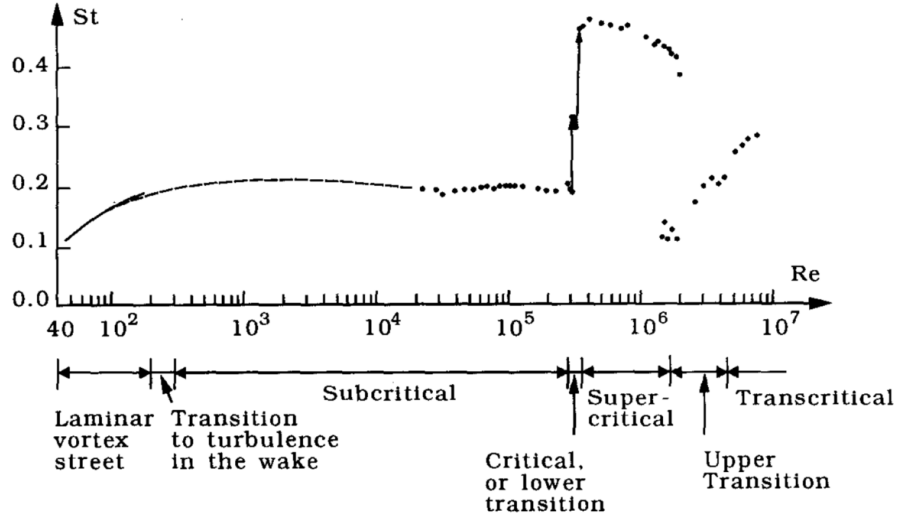


Figure 6: Strouhal number for a smooth circular cylinder. Reprinted from Sumer [22].

### 3.3.2 Forces on a cylinder

The flow around the cylinder will apply force on the cylinder. There are two types of force, one from the pressure and the other from the friction.

The in-line pressure force is given by:

$$F_p = \int_0^{2\pi} p \cos(\theta) r d\theta \quad (11)$$

Where  $p$  is the pressure on the cylinder surface and  $r$  is the cross-section radius of the cylinder.

The in-line friction force is given by:

$$F_f = \int_0^{2\pi} \tau \cos(\theta) r d\theta \quad (12)$$

Where  $\tau$  is the wall shear stress on the cylinder surface.

The total in-line force is the sum of these two forces, given by:

$$F_D = F_p + F_f \quad (13)$$

As discussed in previous section, expect for minimal Reynolds number such as  $Re < 40$ , there will be vortex shedding in all the flow regimes. As vortex starts to shed behind the cylinder, the pressure distribution around the cylinder experience a periodic change. This periodic pressure distribution induces an oscillating in-line force (the drag force) that fluctuates around the mean drag. Unlike flow in the in-line direction, the flow in the cross-flow is symmetric, while there still exists a non-zero force in the transverse direction (the lift force), shown in Figure 7.

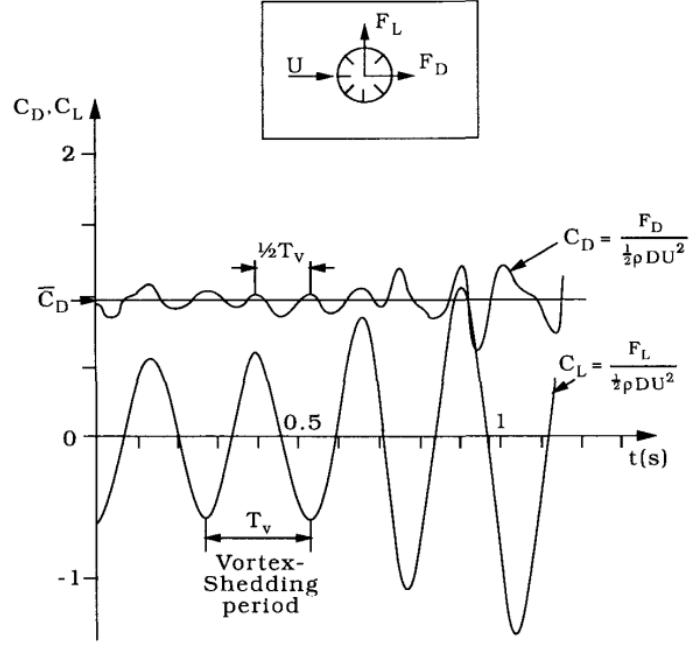


Figure 7: Drag and lift force coefficient. Reprinted from Sumer [22].

The drag and lift coefficient is given by:

$$C_D = \frac{F_D}{\frac{1}{2}\rho DU^2} \quad (14)$$

$$C_L = \frac{F_L}{\frac{1}{2}\rho DU^2} \quad (15)$$

The drag and lift coefficient is highly related to the flow regime around the cylinder because the pressure and the wall shear stress are functions of the Reynolds number for a smooth cylinder. Furthermore, other effects such as the surface roughness, the cross-sectional shape, the incoming turbulence, and the shear in the incoming flow also influence the lift and drag coefficient.

### 3.4 Flow around a cylinder in oscillatory flows

#### 3.4.1 Parameters and flow regimes

The non-dimensional quantity Reynolds number describes the flow around a cylinder in a steady current. When the cylinder is exposed to an oscillatory flow, another dimensionless quantity Keulegan–Carpenter number, also called the period number appears:

$$KC = \frac{U_a T}{D} \quad (16)$$

Where  $U_a$  is the velocity amplitude of the oscillatory flow and  $T$  is the period of the oscillatory flow.

The Stokes number (also called frequency number) is another valid dimensionless parameter which is defined as

$$\beta = \frac{D^2}{\nu T} = \frac{Re}{KC} \quad (17)$$

For a sinusoidal flow, the velocity is given by:

$$U = U_a \sin(\omega t) \quad (18)$$

The maximum of the flow velocity oscillation is:

$$U_a = a\omega = \frac{2\pi a}{T} \quad (19)$$

Where  $a$  is the amplitude of the motion of the fluid particles. Then for the sinusoidal case, the  $KC$  number will be:

$$KC = \frac{2\pi a}{D} \quad (20)$$

Then  $KC$  number describes the ratio of the motion of fluid particles over the diameter of the cylinder. Small  $KC$  numbers, therefore, mean that the fluid particles travel a small distance relative to the width of the cylinder and vice versa.

For  $KC < 15$  and for  $\beta < 160$ , according to the flow structures, Tatsuno et al. [5] categorized oscillatory flow around a cylinder into eight regimes (A\*, A, B, C, D, E, F, and G). These different types of flow structures and their regime boundaries are also reported by Elston et al. [23], Zhao et al. [24] and Tong et al. [25] and are shown in Figure 8.

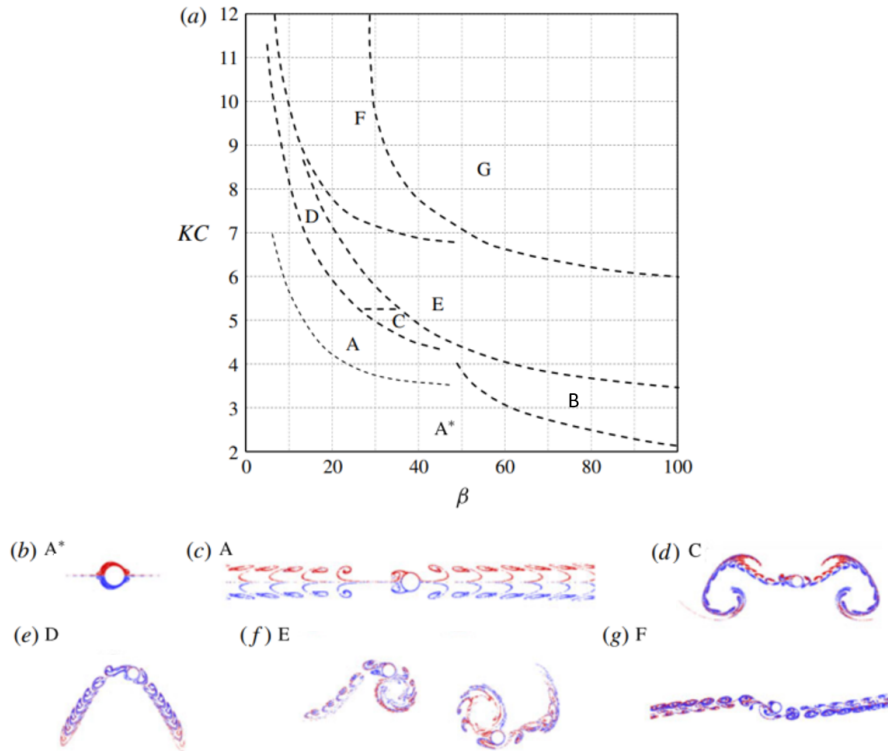


Figure 8: Flow regime for oscillatory flow around a cylinder and streaklines. Reprinted from Elston et al. [23], Zhao et al. [24] and Tong et al. [25].

The flow in regime A\* and A are both two-dimensional along the cylinder and are symmetrical with respect to the oscillatory plane. The only difference is that there are no vortex shedding in regime A\*. Above the regime A\* boundary (which is usually difficult to be determined), two vortices with opposite rotation signs are formed and shed from the cylinder. However, these vortices are weak and will be cancelled by the vorticity from the cylinder boundary layer in half cycle.

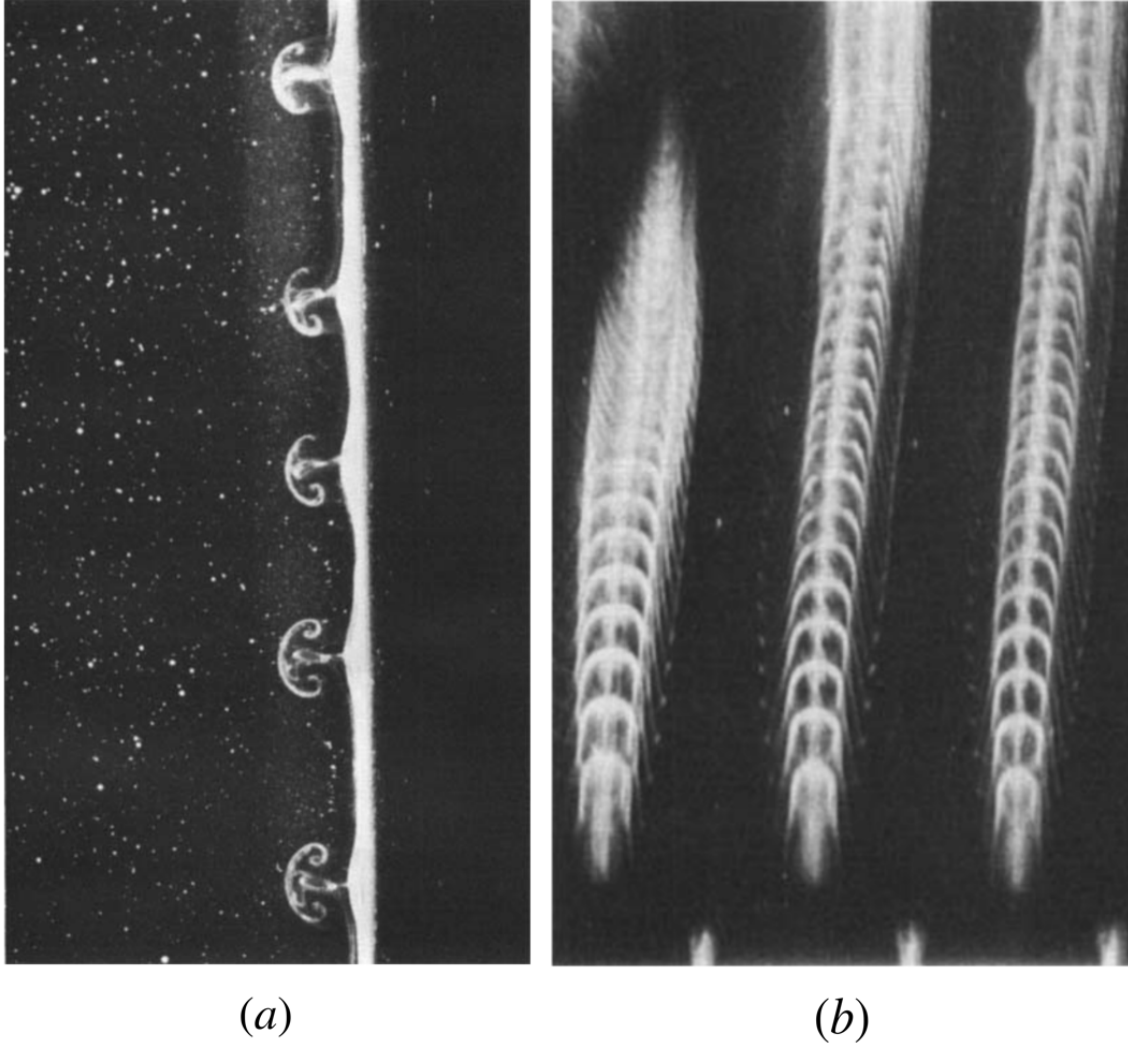


Figure 9: Flow regime B for oscillatory flow around a cylinder and streaklines. (a) is plane view of flow in the  $(y,z)$ -plane and (b) is plane view of flow in the  $(x,z)$ -plane. Reprinted from Elston et al. [23], Zhao et al. [24] and Tong et al. [25].

The flow structures in regime B are greatly different from the other regimes. In this regime, the flow is in the transition from two-dimensional flow to three-dimensional flow, and the vortices formed not because of flow separation, but due to three-dimensional instability in the boundary layer. This three-dimensional instability occurs the form of mushroom-like structures distributed evenly along the spanwise direction of the cylinder. These mushroom-like vortices separate and move away from the cylinder in the oscillatory direction and make up streaked flows shown in Figure 9. The wavelength of the Honji vortex pair has been measured by Honji [6], Tatsuno [5], Sarpkaya [8] according to their experimental results. Sarpkaya [8] also found an empirical equation for the spacing between vortices given by

$$\lambda \sim 22D\beta^{-3/5} \quad (21)$$

---

This empirical equation works well for  $10^3 < \beta$ , but overall, the spacing between adjacent vortices is sensitive to the value of  $KC$ , but hardly relative to the value of  $\beta$ . An et al. [14] conducted a series of numerical investigation on the spacing between vortices over a rang of  $150 < \beta < 550$  and they manged to quantify the relation between  $KC$  and  $\lambda$ . This equation has a good agreement with previous study and given by

$$\lambda \sim 0.2DKC^{7/4} \quad (22)$$

By analysing the governing equations, An et al. [14] explained the reason why spacing is strongly dependent on  $KC$  instead of  $\beta$ .

$$\frac{\partial u_i}{\partial t} = \frac{1}{\beta} \frac{\partial^2 u_i}{\partial x_j^2} - KC \left( u_j \frac{\partial u_i}{\partial x_j} + \frac{\partial p}{\partial x_i} \right) \quad (23)$$

They first define the first term on the right-hand side is diffusion term (DI) and second term is convective-pressure (CP) term. At the plane where the strongest Honji vortices appear, the CP term is about 25 times greater than DI term. Furthermore, the CP term varied greatly in spanwise direction, while the DI term is uniformly distributed along the span of the cylinder. As a result, the Honji vortices are highly dependent on the  $KC$ -related CP term, and this result is agree with the previous observations that the spacing is strongly related to the  $KC$ .

### 3.4.2 Morison's equation

Morison's equation is a semi-empirical equation that is widely used to predict inline loads on a cylindrical element in oscillatory flow. It is a long wave viscous approximation and works well when wavelengths are long relative to the cross-sectional dimension. For a vertical rigid circular cylinder, Morison's equation is given by:

$$F = \rho \frac{\pi D^2}{4} C_M a_1 + \frac{\rho}{2} C_D D |u|u \quad (24)$$

The first term on the right hand side of Equation (24) represents the inertia force, and the second term represents the drag force.  $\rho$  is the mass density of water,  $D$  is the diameter of the cylinder,  $u$  and  $a_1$  are the horizontal undisturbed fluid velocity and acceleration at the geometrical centre of the strip respectively. The drag coefficient  $C_D$  and mass coefficient  $C_M$  have to be empirically determined [21]. Sarpkaya [3] found that, in general, these two coefficients depend on the Keulegan–Carpenter number, Reynolds number, and surface roughness.

For a flow with velocity given in Equation (18) is inserted into the Morison's equation Equation (24) and the inline force coefficient is:

$$C_f = \frac{\pi^2}{KC} \cos(\omega t) C_M + \sin(\omega t) |\sin(\omega t)| C_D \quad (25)$$

Equation (25) shows not only  $C_D$  and  $C_M$  themselves depend on the  $KC$  number, but also the weights of  $C_D$  and  $C_M$  in inline force coefficient are related to  $KC$  number.

## 3.5 Flow around a step cylinder

As mentioned early, the wake structures behind the circular cylinder is strongly related to the  $Re$ , and the distinct flow structures are only appear for certain range of  $Re$ . However, even with same  $Re$  range, after a cylinder with complicated noncontinuous geometries, the wake tends to have more unwanted three-dimensionality and complex three-dimensional dynamics.



The three-dimensionality in wake behind a cylinder is commonly found in which discontinuities in velocity or diameter exist. These discontinuities can cause change of shedding frequency along spanwise direction. Typically for flow around a step cylinder, there are three types of vortex interaction modes due to these various shedding frequency: a direct mode, a transitional mode and an indirect mode. The occurrences and characteristics are related to two important parameters: Reynolds number ( $Re$ ) and diameter ratio ( $D/d$ ) between the large diameter ( $D$ ) and small diameter ( $d$ ) parts of the step cylinder. Dunn [19] define three types of spanwise vortices with constant frequency:

- S-cell vortex with the highest shedding frequency  $f_S$  shed from the small cylinder
- N-cell vortex with the lowest shedding frequency  $f_N$  only appears in the modulation zone when  $1.55 < D/d$
- L-cell vortex with shedding frequency  $f_L$  shed from the large cylinder

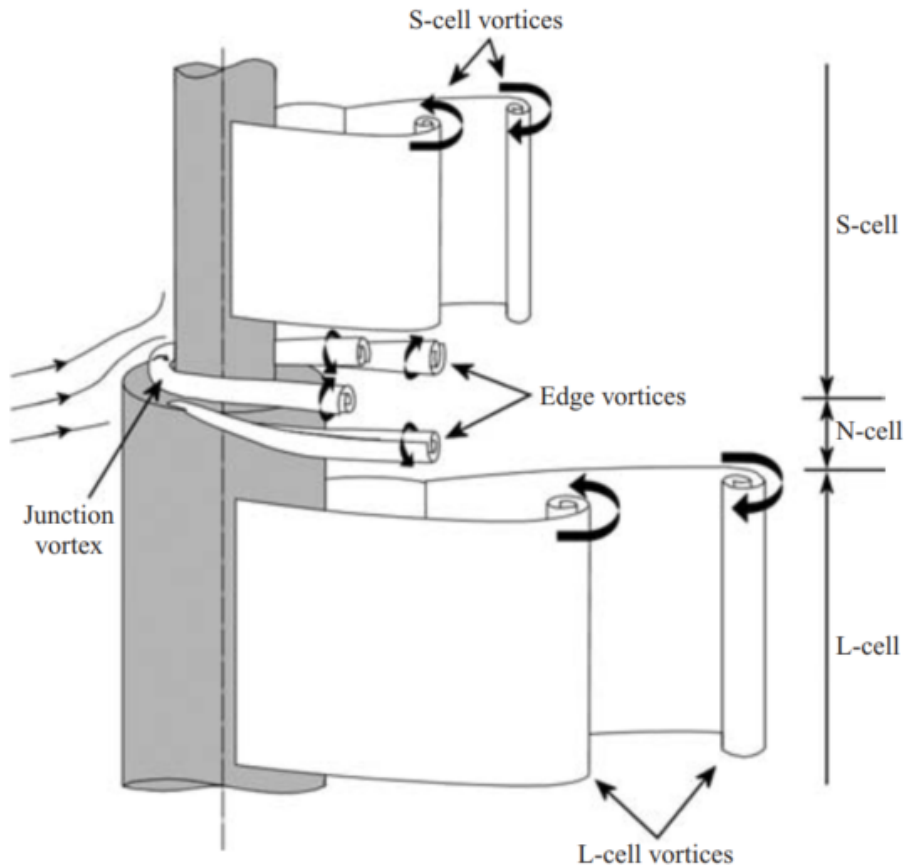


Figure 10: Different types of vortices near the step cylinder. Reprinted from Dunn [19].

In a low Reynolds number range ( $35 < Re < 200$ ), the direct mode dominates when  $D/d < 1.25$ . In direct mode, two distinct shedding frequencies  $f_S$  and  $f_L$  associate to vortices behind the small and large cylinders interact with each other across the interface which is a narrow region of quasiperiodic frequency interaction.

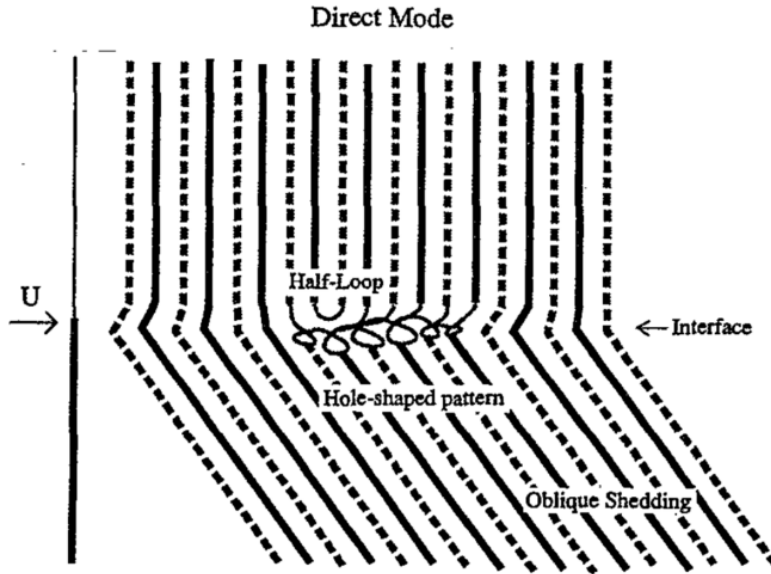


Figure 11: Sketch of vortex lines and vortex linkages in direct mode (large cylinder  $Re_L = 76$ , small cylinder  $Re_S = 57$ ). Reprinted from Lewis and Gharib. [16].

If the vortices are nearly in phase, they would directly connect to one another across the interface. Otherwise, the linkages across the interface are broken and the vortices tend to connect to one another on the same side of interface, and this phenomenon is called vortex-splitting or vortex dislocations. The absence of connection between different sides of the interaction region could lead to holes forming in the interface. Among these one-sided connections in S-cell, at least one vortex form a linkage to the next vortex of opposite sign. This kind of connection is named half-loop and it is a weak vortex linkage which cause subharmonics of the shedding frequency in analysis of local frequency.

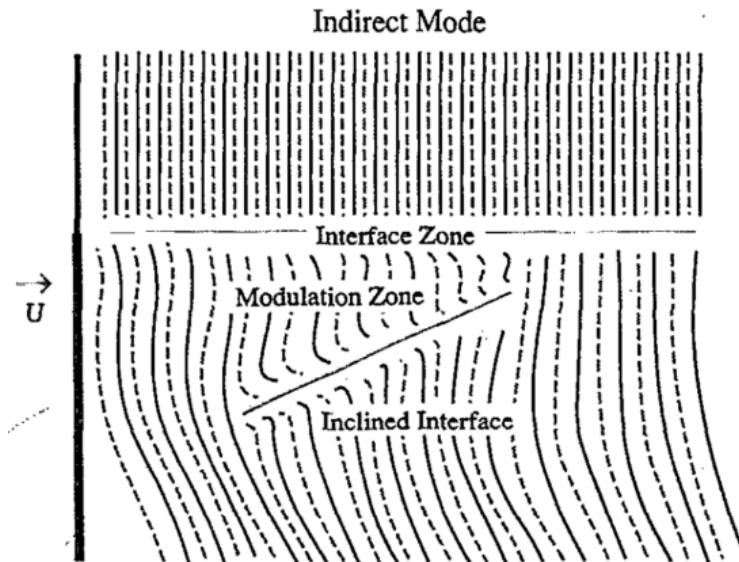


Figure 12: Sketch of vortex lines and vortex linkages in indirect mode (large cylinder  $Re_L = 99$ , small cylinder  $Re_S = 56$ ). Reprinted from Lewis and Gharib. [16].

When the  $D/d$  keeps increasing until it exceeds 1.55, the indirect mode dominates. It is clear that in the large-diameter wake a new region called modulation zone appears. In the modulation zone

a third shedding frequency  $f_N$  is found. As mentioned before, the frequency  $f_N$  is typically lower than the other two shedding frequencies  $f_L$  and  $f_S$ , but unlike the half-loop, it is not caused by the quasiperiodic interaction of  $f_L$  and  $f_S$ .

Other distinct differences between direct and indirect mode are the feature and number of interface regions. Due to the presence of the modulated zone, the interface zone in indirect mode collapses into a plane which is nearly perpendicular to the axis of the cylinders. There are no directly connections between the two sides of the interface zone, but in interface zone the vortices interact with each other in a range of frequencies between  $f_N$  and  $f_S$ . In addition to perpendicular interface, another kind of inclined interface occurs at the beat frequency  $f_L - f_N$  in the modulation zone. The inclined interface start form the bottom side of the interface zone and extends spanwise across the modulation zone with a large angle. However, because of its low frequency, after several vortex-shedding cycles, the inclined interfaces are not always appear clearly. Morton and Yarusevych [26] found that the occurrence of inclined interface is due to the vortex dislocations between N-cell and L-cell vortices.

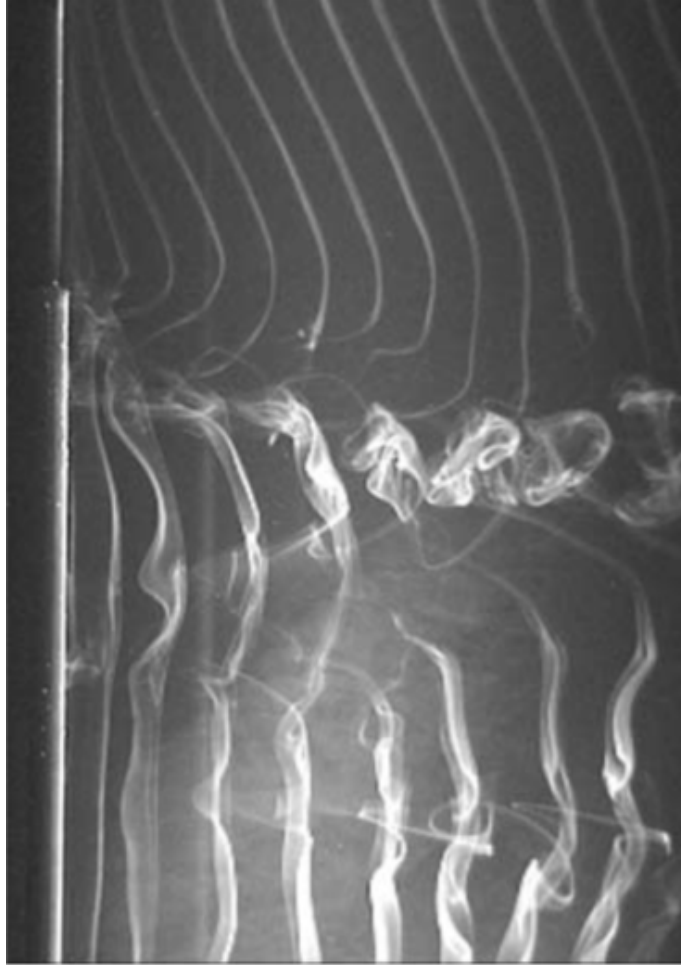


Figure 13: Vortex-shedding patterns from the step cylinder (large cylinder  $Re_L = 156$ , small cylinder  $Re_S = 79$ ). Reprinted from Dunn [19].

The structures of L-cell vortices and S-cell vortices are different due to the Reynolds number difference and the presence of the step. The S-cell shown in Figure 11, Figure 12, Figure 13 are laminar and parallel to each other. These vortices are lightly affected along the spanwise direction up to a several diameters from the step. There are slight waviness near the step, but far downstream from the step, the S-cell vortices are remained parallel. However, even with  $Re_L = 156$ , three-dimensionality caused by the oncontinuous geometry results an earlier transition in L-cell from laminar to turbulent. As a result, there are more waviness along the length of the

---

L-cell vortices, and unlike the parallel S-cell, the subsequent vortices of L-cell are connected by streamwise structures called 'fingers' (shown in Figure 13). These streamwise fingers exit near the cylinder and decay far downstream due to the unstable motions.

Normally, except for the vortices closed to two sides of the interface zone, the N-cell vortices and S-cell vortices both tend to incline with respect to the axis of the cylinder. The vortex shedding of S-cell starts within few diameters from the step and moves away from the step along the span of the cylinder. As a result, the inclination of S-cell starts from step, and the part away from the step is less inclined than the part near the step. In contrast, the vortex shedding of N-cell starts away from the step and moves spanwise toward the step. As a consequence, the N-cell vortices inclines in a way that the part away from step is farther downstream than the part near the step. These different inclinations in N-cell vortices and S-cell vortices are caused due to the pressure differences between the large cylinder and small cylinder. The pressure of the small cylinder is larger than the large cylinder, and this difference make the small cylinder wake spanwise extend across the interface zone and spray into the large cylinder wake. Because of the pressure difference, the flow separates at the trailing edge of the step, and roll down in to the large cylinder wake. This phenomenon is called downwash and lead the early shedding of S-cell vortices near the step and suppress the shedding of N-cell vortices closed to the step.

---

## 4 Governing equations and numerical method

Many engineering practices include several flow conditions and therefore require different treatments. The most accurate approach to flow simulation is to solve the Navier-Stokes equations directly without averaging or approximation, and it is also the simplest approach from the conceptual point of view [27]. This section contains a picture of the solution algorithm and immersed boundary method.

### 4.1 Mass conservation

The conservation of mass is one of the fundamental principle used in fluid mechanics. It states that the mass can neither be created nor destroyed, but can be rearranged in a control volume. In fluid mechanics problems, the mass flow into a control volume must be equal to the mass flow out of it. The conservation of mass can be expressed by using the continuity equation:

$$\frac{\partial \rho}{\partial t} + \nabla \cdot (\rho \mathbf{u}) = 0 \quad (26)$$

Where  $\rho$  is the density,  $\mathbf{u}$  is the flow field. For incompressible flow, the  $\rho$  is constant over the entire domain, and for a three-dimensional problem the continuity equation is simplified:

$$\frac{\partial u}{\partial x} + \frac{\partial v}{\partial y} + \frac{\partial w}{\partial z} = 0 \quad (27)$$

### 4.2 Momentum conservation

The conservation of momentum is another fundamental principle. This law is applied on isolated system of objects, which means no external forces act on the system and the amount of momentum remains constant. The change of the momentum is through the action of forces described by Newton's laws of motion and the general conservation of momentum is described as:

$$\rho \frac{Du_i}{Dt} = -\frac{\partial p}{\partial x_i} + \frac{\partial}{\partial x_j} \left( \mu \frac{\partial u_i}{\partial x_j} + \frac{\partial u_j}{\partial x_i} \right) + \rho f_i \quad (28)$$

Where for three-dimensional problem, the fluid momentum are described in x-,y-,z-direction for  $i = 1, 2, 3$  and  $j = 1, 2, 3$ . The left hand of the equation describes the acceleration of the fluid in three directions. The first term on the right hand side is the pressure term, and it is followed by the dynamic viscosity term and the body force term.

### 4.3 The Navier–Stokes equations

The Navier–Stokes equations based on the consecration of momentum and conservation of mass governs the Newtonian fluids. For an incompressible Newtonian fluid the Navier–Stokes equations can be expressed as:

$$\frac{Du_i}{Dt} = -\frac{1}{\rho} \frac{\partial p}{\partial x_i} + \nu \frac{\partial^2 u_i}{\partial x_j \partial x_j} \quad (29)$$

The Navier–Stokes equations are useful because they describe the motion of the fluid, but there are not general solutions for the Navier–Stokes equations due to the inherent complexities: second order derivative term, nonlinear term and incompressibility constraint. Thus, the full(not simplified) Navier–Stokes equations can only be solved numerically.

---

#### 4.4 The solution algorithm

The MGLET solver is based on a second-order finite volume discretization for the Navier-Stokes equations for an incompressible fluid on a staggered Cartesian grid with non-equidistant spacing. In time, the discretized equations are integrated with Williamson's Third-order low-storage Runge-Kutta scheme with a constant time step  $\Delta t$  is used to ensure a Courant-Friedrichs-Lewy (CFL) number smaller than 0.5 [28]. The spatial discretization is second-order (central) for the convective and diffusive terms [29]. The finite-volume method starts from taking integral over the conservation:

$$\frac{\partial}{\partial t} \int_{\Omega} u_i \, d\Omega + \iint_S \frac{\partial u_i u_j}{\partial x_j} \, dS = - \iint_S \frac{\partial p}{\partial x_i} \, dS + \iint_S \nu \frac{\partial^2 u_i}{\partial x_j \partial x_j} \, dS \quad (30)$$

The solution domain is subdivided into a finite number of contiguous control volumes (CVs), and the conservation equations are applied to each CV. The flow variables are defined on a non-equidistant Cartesian mesh in a staggered arrangement for this project [30]. For a staggered grid (shown in Figure 14) the velocity are defined at the middle of the face of control volume and the pressure are stored at the center of the control volumes. The staggered arrangement eliminates the odd-even decoupling between the velocity and pressure if they are stored at the same position, but the staggered arrangement is complicated than the collocated arrangement. If one knows the convective fluxes in the three Cartesian directions, the integration of the momentum equation could be done. By using the midpoint rule, the convective fluxes could be calculated at the faces of the control volumes. However, for a second order spatial discretization, the velocities  $u(i+1/2, j)$  and  $u(i, j+1/2)$  at the middle of the faces of the control volumes are unknown and they should be computed by using linear interpolation. The velocity derivatives  $\partial u / \partial x(i+1/2, j)$  and  $\partial u / \partial x(i, j+1/2)$  are calculated by using central difference method [31].

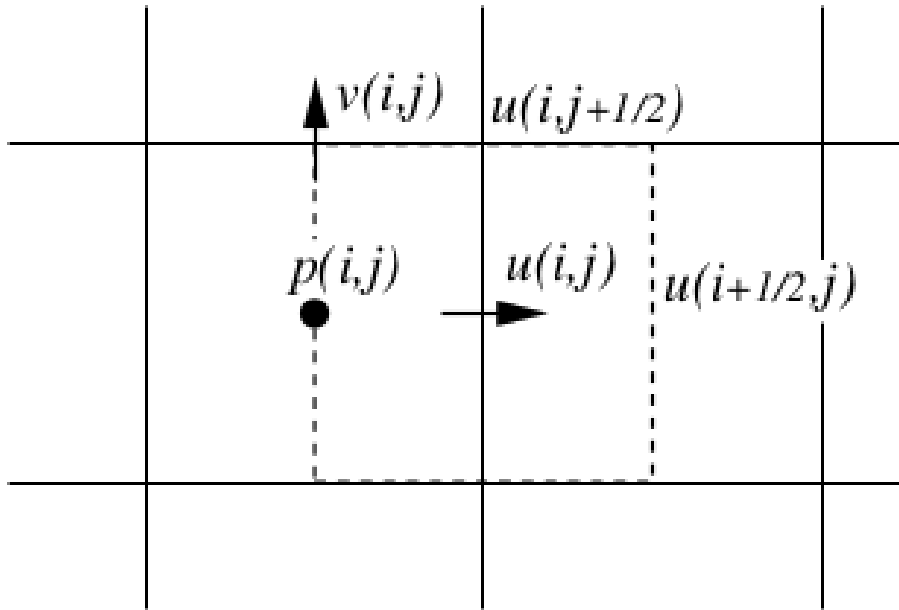


Figure 14: Staggered arrangement of the variables in grid. Dashed line: momentum cell for  $u$ -velocity. Reprinted from Manhart [31].

Conventionally, when simulating fluid-structure interactions, the structured or unstructured grid that conforms to the boundary is applied. However, these grids need to be generated numerically, and if the boundary is moving, grids has to be re-computed which could lead to a significant

increase in computational cost. As a result, in this numerical simulation, the immersed boundary method (IBM) is used to take into account the effect of the body on a flow inside the Cartesian grid. The advantage of the immersed boundary method is that it has great mesh generation for complex geometries and do not necessarily conform to the boundary. Thus, the immersed boundary method saves the memory and computation power. To apply the immersed boundary method, an additional body-force term is added to the Equation (29) and it gives:

$$\frac{Du_i}{Dt} = -\frac{1}{\rho} \frac{\partial p}{\partial x_i} + \nu \frac{\partial^2 u_i}{\partial x_j \partial x_j} + f_i \quad (31)$$

Depending on the way to apply the momentum forcing, there are two groups of forcing approaches for IBM, the discrete forcing approach and continuous forcing approach. For continuous forcing approach the momentum forcing is spread at Lagrangian points to fluid grid points. Thus, the continuous forcing approach is flexible at distributing the grid near the boundary and it is generally applied to the elastic bodies. However, due to the lack of rigidity and numerical stability, the continuous forcing approach is not applicable for rigid bodies. As a consequence, the discrete forcing approach is more suitable for problem with solid step cylinder. In the discrete forcing approach, the governing equations Equation (31) without body-force term are solved on a fixed Cartesian grid, in another word, the governing equations are discretized on the domain pretending that the immersed boundary do not exist. Then, the no-slip and no-penetrations boundary conditions is imposed implicitly or explicitly (generally using implicit treatment for stiff material) on the immersed boundary by using additional interpolation schemes. These are many different interpolation schemes developed by previous studies, all of them require the variables on the grid points near the interface, and in some problems, the concept of ghost cells may also be used.

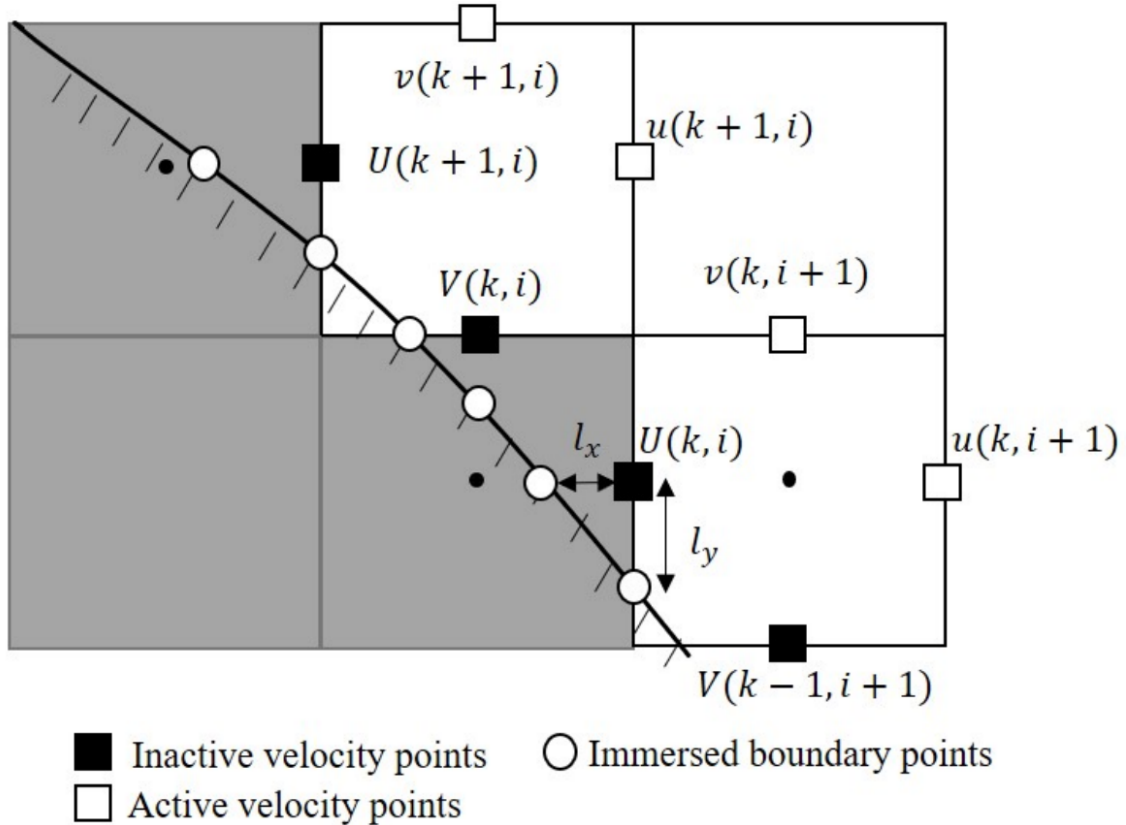


Figure 15: Treatment of the immersed boundary. Reprinted from Jiang [32].

In this thesis, the immersed boundary method is based on the high-order stable interpolations method developed by Peller et al. [33]. The values of velocities at ambiguous points on the

---

immersed boundary are a sum of values of velocities interpolated along each directions. The interpolation is formed by weighted factor multiplying the distance between the ambiguous points and the inactive velocity points. The treatment of the immersed boundary and the arrangement of different groups of points shown in Figure 14. The velocities based on the Lagrange interpolation method according to the following stencil formulation described as:

$$\phi(x) = \left( \sum_{i=1}^3 \alpha_i(x) \cdot \phi_i \right) + \alpha_r(x_r) \cdot \phi_r \quad (32)$$

Where  $\phi(x)$ ,  $\phi_i$  and  $\phi_r$ , is the values of velocity at the inactive velocity points, the active velocity points and the immersed boundary points, respectively, the number three shows that there are three neighbours involved in the interpolation. The Lagrange coefficients  $\alpha_i$  and  $\alpha_r$  are obtained by the Lagrange formula:

$$\alpha_i(x) = \left( \prod_{j=1, j \neq k}^3 \frac{(x - x_j)}{(x_k - x_j)} \right) \frac{x - x_r}{x_k - x_r} \quad (33)$$

$$\alpha_r(x_r) = \left( \prod_{j=1}^3 \frac{(x - x_j)}{(x_r - x_j)} \right) \quad (34)$$

This is a third-order polynomial and the accuracy of the interpolation is of order  $O(\Delta x^4)$ , because the degree of the interpolation polynomial is one order less than the order of accuracy. For an inactive velocity point that can be interpolated from two directions, the value of velocity can be expressed by:

$$\phi(x) = \lambda_x \phi^x + \lambda_y \phi^y \quad (35)$$

Where  $x$  and  $y$  are the interpolation in  $x$  and  $y$  directions. The weighing factors  $\lambda_x$  and  $\lambda_y$  are:

$$\lambda_x = \frac{1}{1 + \left(\frac{l_x}{l_y}\right)^2} \quad \text{and} \quad \lambda_y = \frac{1}{1 + \left(\frac{l_y}{l_x}\right)^2} \quad (36)$$

Where  $\lambda_x$  and  $\lambda_y$  are the distance between the immersed boundary and the inactive velocity point in  $x$  and  $y$  directions, respectively.

After the governing equations are discretized on the fluid domain and the immersed boundary, time integration can be performed via an explicit low-storage third-order Runge-Kutta method developed by Williamson [34]. The semi-discrete form of Equation (29) is given:

$$\frac{\partial u}{\partial t} = D(u) + C(u) + G(p) \quad (37)$$

Where  $D(u)$  is the discretized diffusive term,  $C(u)$  is the discretized convective term,  $G(p)$  is the discretized pressure gradient term.

The three steps of the third-order Runge-Kutta method developed by Canabes [35] are given:



$$\left\{ \begin{array}{l} h_1 = f(u) \\ \tilde{u} = u + \frac{\Delta t}{3} h_1 \\ \text{div}[G(\delta\tilde{p})] \frac{\Delta t}{3} = -\text{div}(\tilde{u}) \\ p = p + \delta\tilde{p} \\ u = \tilde{u} + \frac{\Delta t}{3} G(\delta\tilde{p}). \end{array} \right. \quad (38)$$

$$\left\{ \begin{array}{l} h_2 = f(u) \\ h_1 = h_2 - \frac{5}{9} h_1 \\ \tilde{u} = u + \frac{15}{16} \Delta t h_1 \\ \text{div}[G(\delta\tilde{p})] \frac{3}{4} \Delta t = -\text{div}(\tilde{u}) \\ p = p + \delta\tilde{p} \\ u = \tilde{u} + \frac{3}{4} \Delta t G(\delta\tilde{p}) \end{array} \right. \quad (39)$$

$$\left\{ \begin{array}{l} h_2 = f(u) \\ h_1 = h_2 - \frac{153}{128} h_1 \\ \tilde{u} = u + \frac{8}{15} \Delta t h_1 \\ \text{div}[G(\delta\tilde{p})] \Delta t = -\text{div}(\tilde{u}) \\ p = p + \delta\tilde{p} \\ u = \tilde{u} + \Delta t G(\delta\tilde{p}) \\ u^{n+1} = u \end{array} \right. \quad (40)$$

The Poisson equation for the pressure is solved in every steps of the Runge-Kutta method. The discretized form of the Poisson equation for pressure correction developed by Canabes [35] is:

$$\begin{aligned} & \left[ -\frac{1}{\Delta x_P} \left( \frac{\delta p_E - \delta p_P}{\delta x_e} - \frac{\delta p_P - \delta p_W}{\delta x_w} \right) \right. \\ & - \frac{1}{\Delta y_P} \left( \frac{\delta p_N - \delta p_P}{\delta y_n} - \frac{\delta p_P - \delta p_S}{\delta y_s} \right) \\ & \left. - \frac{1}{\Delta z_P} \left( \frac{\delta p_T - \delta p_P}{\delta z_t} - \frac{\delta p_P - \delta p_B}{\delta z_b} \right) \right] \frac{\Delta t}{\rho} \\ & = - \left( \frac{\tilde{u}_P + \tilde{u}_W}{\Delta x_P} - \frac{\tilde{u}_P - \tilde{u}_S}{\Delta y_P} + \frac{\tilde{u}_P - \tilde{u}_B}{\Delta z_P} \right) \end{aligned} \quad (41)$$

This linear equations is solved by the Stone's strongly implicit procedure(SIP).

---

## 5 Numerical step-up

### 5.1 Computational domain and grid

The computational domain is the space where the CFD simulation is conducted. The computational domain is need to be well meshed to solve the discretized governing equation of fluid flows. Thus, the domain size should be large enough to include the result of the interaction between flows and structures. Furthermore, the domain size should also be large enough to prevent great unwanted effects on the boundaries. Therefore, the dimensions of computational domain are dependent on the problems and there is no general computational domains suitable for all cases.

A three-dimensional cuboid shaped computational domain is used in the present project and a circular cylinder with a step is placed at the center of the three-dimensional rectangular domain, and the inlet and outlet are half  $L_x$  away from the center of the cylinder. The length of streamwise direction  $L_x$  is  $51.2D$ , and the depth of transverse direction  $L_y$  is  $32D$ , and the height of the spanwise direction  $L_z$  is  $32D$ . The choice of the domain size is based on previous research and the strategy of mesh generation. The domain convergence test presented in later section shows that this computational domain is large enough to capture the three-dimensional influence of the flow while avoid boundary effects.

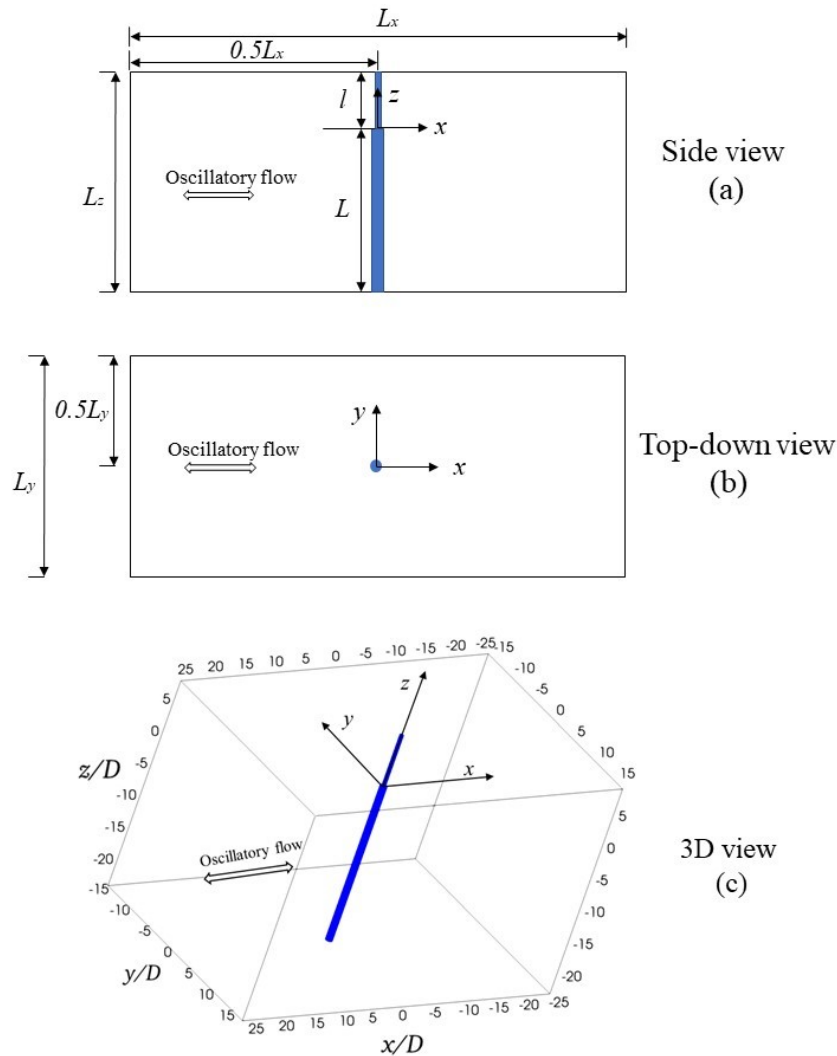


Figure 16: The coordinate system and computational domain.

As discoursed in the previous section, because the pressure of the small cylinder is greater than the large cylinder, the downwash causes great effects on the vortices behind the large cylinder, and leaves the vortices behind the small cylinder nearly undistributed. Thus, to prevent the boundaries from the three-dimensionality due to the presence of the step, the length of the large cylinder should be greater than the length of small cylinder. In this case, the length of large cylinder is  $24D$  and the length of small cylinder is  $8D$ . The diameters of the large and small cylinder is determined in a way that the oscillatory flow around large cylinder is in regime B and around small cylinder is in regime A. As a consequence, the diameter ( $D$ ) of the large cylinder is 1 meter, and the diameter ratio ( $D/d$ ) is 1.8, and thus the diameter of the small cylinder is 0.5556 meter.

The computational domain is first equally divided into cubic Cartesian grid boxes, which are named as the level-1 box. Furthermore, there are  $N \times N \times N$  equal-sized cubic Cartesian grid cells uniformly distributed in each grid box. Normally the level-1 boxes are not fine enough to capture the information of complex flow phenomena, such as the form of vortices. As a result, high grid refinement throughout the domain is required throughout the region where these complex phenomena appear. In these regions, a fine zonal grid is embedded into the global coarse grid. All the grid boxes (the level-1 box) are equally divided into  $N \times N \times N$  small cubic Cartesian grid cells, named the level-2 box. There are also  $N \times N \times N$  grid cells in each level-2 box. Thus, the level-2 boxes have a higher grid resolution which is about two times finer than the level-1 boxes. This grid refinement process continues automatically until the details of the complex flow can be captured, and thus the grid independence is achieved. The mesh details used in the simulation can be found in Figure 17. There are five levels of cubic Cartesian grid boxes as numbered in Figure 17, and each grid box contains  $20 \times 20 \times 20$  grid cells. All in all, a total of  $1.2224 \times 10^8$  grid cells, with minimum grid cell size  $\Delta_s/D = 0.01$ , largest grid cell size  $\Delta_l/D = 0.16$ , were used to discretize the computational domain. Different grid sizes are used to verify the grid independence in a conventional study.

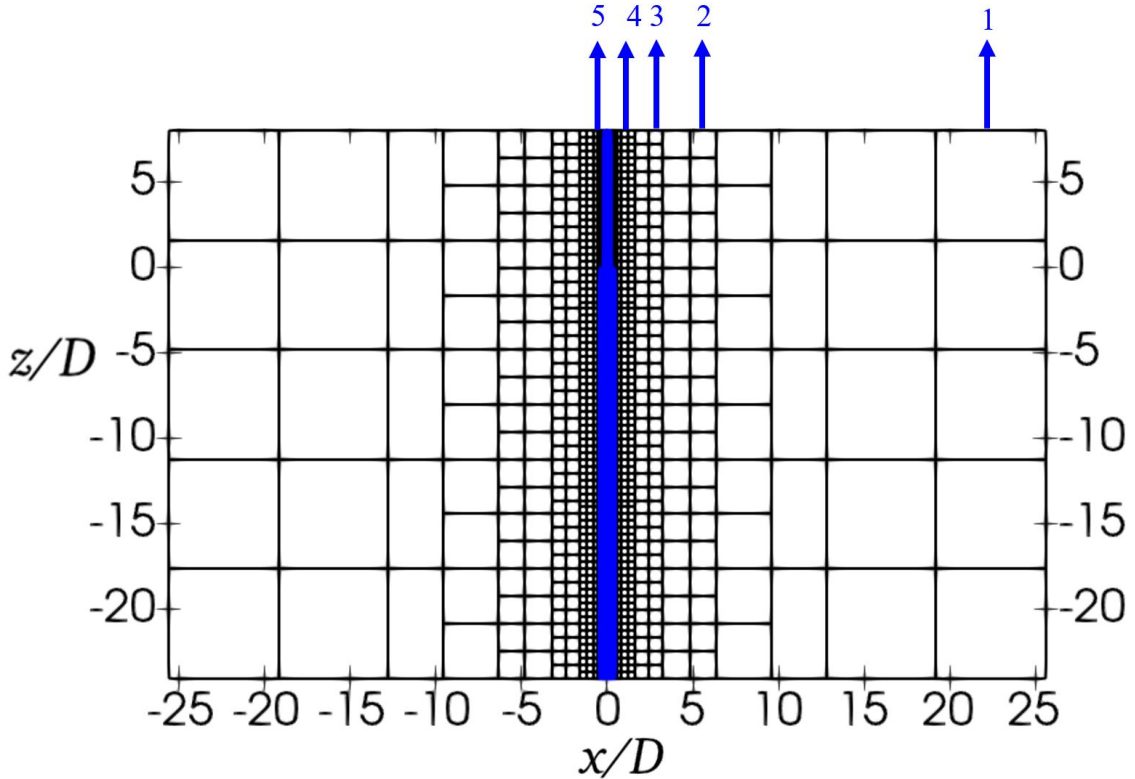


Figure 17: Multi-level grids in the  $(x, z)$ -plane at  $y/D = 0$ . The level of boxes are illustrated with the blue line arrows and numbers. Numbers 1 to 5 represent the coarsest boxes to the finest grid cells.

Table 1: Detailed mesh information.

Min. cell size $\Delta_s/D$	Max. cell size $\Delta_l/D$	Domain size ( $L_x \times L_y \times L_z/D$ )	Number of grid cells
0.01	0.16	$51.2 \times 32 \times 32$	$1.2224 \times 10^8$

In this project, because the flow oscillates, the maximum CFL number oscillates between 0.147 and 0.352. Since the maximum CFL number is less than 0.5, the time steps  $\Delta t u/D = 0.002$  and minimum grid  $\Delta_s/D = 0.01$  are acceptable for the MGLET solver.

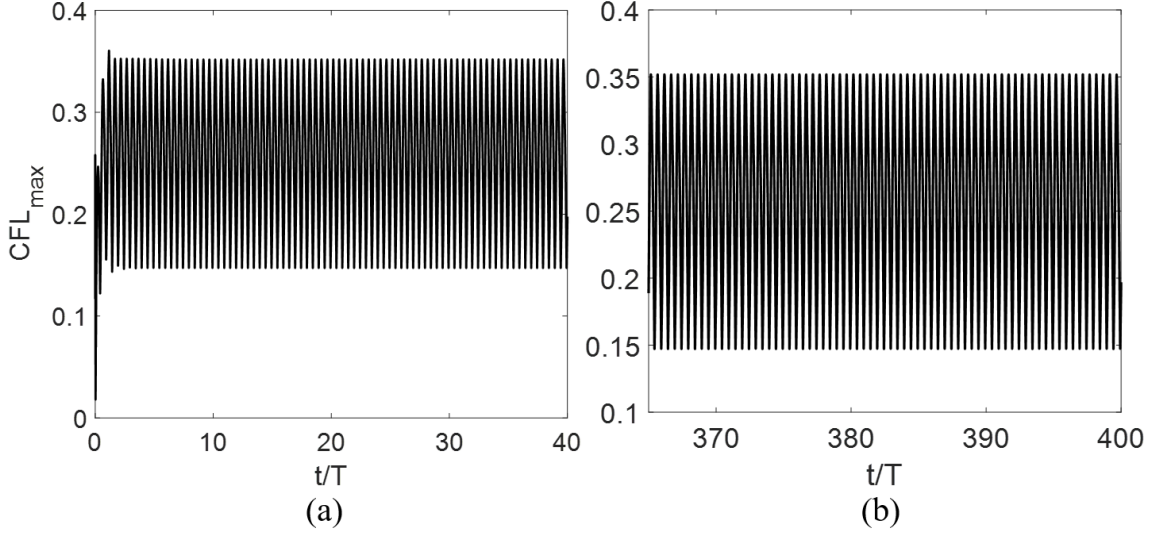


Figure 18: Time series of the maximum CFL criterion. (a) The CFL criterion from 0-40T (b) The CFL criterion from 365T-400T.

## 5.2 Boundary conditions

The boundary conditions applied to the domain boundaries are one of the most critical parameters for the solution of the numerical simulation, because boundary conditions link the simulation model to its surroundings and define the inputs and outputs of the flows. There are two different inlet and outlet boundary condition are tested in this numerical simulation. The details of the boundary conditions for two cases are shown in Table 2.

Table 2: Two different boundary conditions tested in the domain.

Case	Inlet	Outlet	Step cylinder	Top and bottom	Front and back
A	Fixed velocity	Pressure	No-slip	Free slip	Free slip
B	Periodic	Periodic	No-slip	Free slip	Free slip

In case A, the flow is driven by velocity. Thus, the inlet has a fixed velocity condition and the outlet is pressure outlet boundary condition. At the inlet, the velocity vector and its fixed value are shown in Equation (42), where  $U_a$  is equal to  $1m/s$ . The pressure gradient is fixed to be zero at the inlet which means that the pressure persists in value at the inlet. At the outlet the pressure is given a fixed value, which means that the outlet should be far enough from the step cylinder to prevent the flow near the outlet from the disturbed flow due to the presence of the step cylinder. As a consequence, the domain and the distance between the step cylinder and outlet should be large enough to eliminate the effects of the outlet boundary condition.

---

In case B, the inlet and outlet are both set to be periodic boundary conditions. The periodic boundary condition defines a cyclic situation of the flow across the boundary surface. For this condition, two boundaries with same size and shape are treated as if they are physically connected and thus, the flow exiting from one boundary then enters the other boundary. Mathematically speaking, the flow across the two boundaries has same magnitude but with opposite signs. In case B the flow is driven by pressure and how to achieve it is described as follow.

The oscillatory flow is considered to be incompressible, and the aiming fluid velocity is only in x-direction. The fluid velocity is specified to be

$$(u, v, w) = (U_a \sin\left(\frac{2\pi t}{T}\right), 0, 0) \quad (42)$$

This study applies an oscillating pressure gradient is applied to the fluid in the computational domain to force the flow to oscillate. The Navier-Stokes equation with this additional written as:

$$\frac{\partial u_i}{\partial t} + u_j \frac{\partial u_i}{\partial x_j} = -\frac{1}{\rho} \frac{\partial p}{\partial x_i} + \nu \frac{\partial^2 u_i}{\partial x_j \partial x_j} - \varphi_i \quad (43)$$

Where the forcing term  $\varphi_i$  represents the force generated by the oscillating pressure gradient. Since the aiming fluid velocity is defined in Equation (42), the additional forcing term can be written as:

$$\varphi_i = -U_a \frac{2\pi}{T} \cos\left(\frac{2\pi t}{T}\right) \delta_{ix} \quad (44)$$

Where  $\delta_{ix}$  is the Kronecker delta. According to Jiang [36], the effect of the forcing term can be absorbed by the reformulated pressure

$$\tilde{p} = p + p_\varphi \quad (45)$$

with

$$p_\varphi = U_a x \frac{2\pi}{T} \cos\left(\frac{2\pi t}{T}\right) \quad (46)$$

By using the reformulation, Batchelor [37] found that the pressure gradient term can absorb the forcing term while has no influence on the velocity field calculated from the Navier-Stokes equations.

The step cylinder has a no-slip condition which means that the velocities and the pressure gradients are zero at the surface of the step cylinder and the boundaries of the step cylinder are treated as walls. The free slip conditions are applied to the rest of boundaries: top, bottom, front and back boundaries. In this case, the normal velocity components are fixed to be zero and the tangential velocity components have zero gradients. Physically it means that flow do not go trough these but move along these boundaries. However, the free slip condition requires that the boundaries should be far away from the cylinders, especially the region where the flow structures are sensitive to the velocities.

The Figure 19 Figure 20 show the Comparison between theoretical and simulative fluid velocity  $u$  at two corner points on inlet and outlet in case A and case B, respectively. In case A, the setting of velocity inlet and fixed pressure outlet achieves a fine match between theoretical and simulative fluid velocity  $u$ . On the other hand, in case B, the periodic boundary condition at the inlet and the outlet can lead to a very small phase difference between theoretical and simulative fluid velocity  $u$ . Although this setting of periodic boundary condition at the inlet and the outlet cloud cause unwanted errors, because this phase difference in velocity  $u$  are relatively small, it can still give good simulation results as shown in the next section. However, to reduce simulation errors, the boundary conditions in case A are used for final numerical simulation of the oscillatory flow around a step circular cylinder.

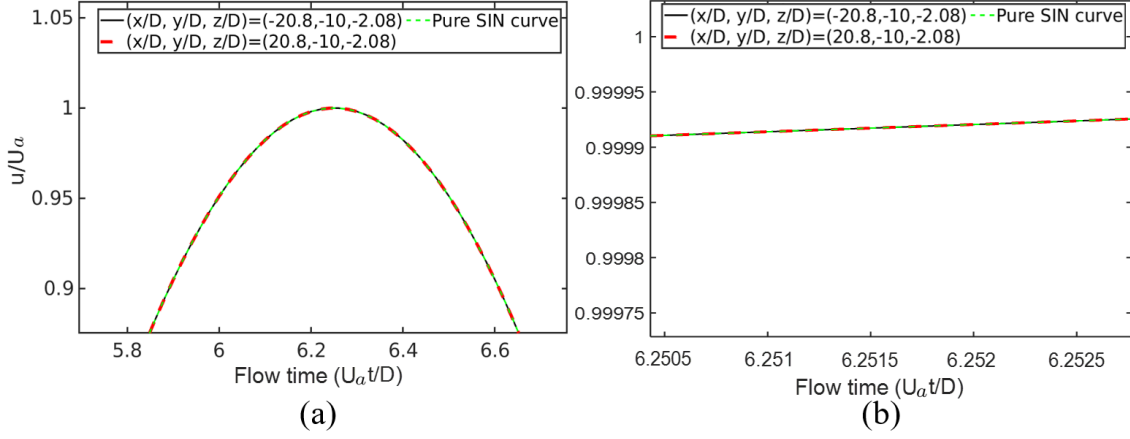


Figure 19: Comparison between theoretical and simulative fluid velocity  $u$  at two corner points on inlet (black solid line) and outlet (red dash line) in case A. The theoretical sinusoidal velocity  $u$  is illustrated by green dash line. (a) shows one peak of the velocity  $u$  and (b) shows zoomed in velocity  $u$  at the peak

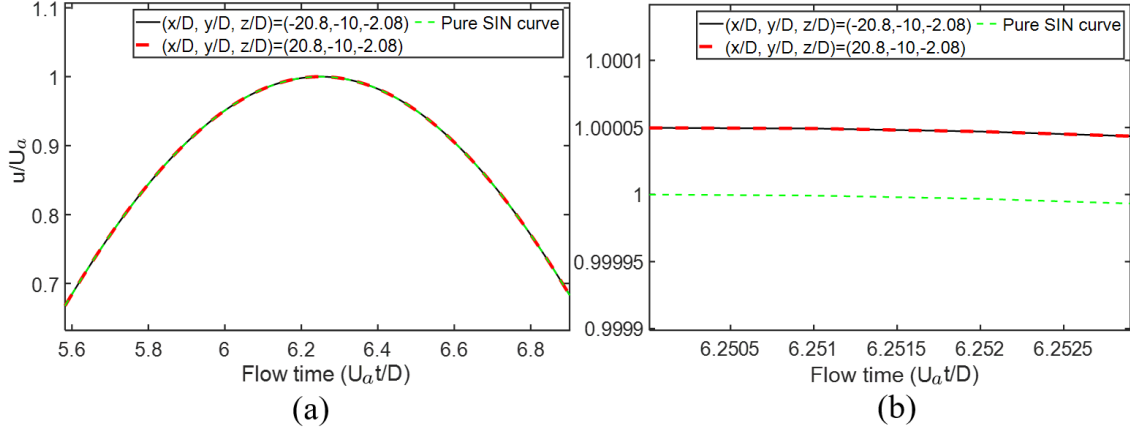


Figure 20: Comparison between theoretical and simulative fluid velocity  $u$  at two corner points on inlet (black solid line) and outlet (red dash line) in case B. The theoretical sinusoidal velocity  $u$  is illustrated by green dash line. (a) shows one peak of the velocity  $u$  and (b) shows zoomed in velocity  $u$  at the peak

### 5.3 Validity of the numerical code MGLET

Unlike commonly used CFD software packages such as OpenFOAM, although MGLET has been used for excellent performance on high-performance computing system, its validity for present numerical simulations still need to be assessed. Thus, a numerical investigation of oscillatory flow around a circular cylinder in regime B is carried out.

The coordinate system, the geometry of the computational domain, and the oscillatory flow direction are similar to the final simulation (shown in Figure 16), but with different dimensions. The details of domain size and flow property are shown in Table 3. The two vertical side boundaries in  $(x,z)$ -plane use the free-slip conditions ( $v = 0, \partial u/\partial y = \partial w/\partial y = 0$ ) while periodic conditions are used at the other four boundaries (inlet, outlet, top and bottom). The cylinder surfaces are regraded as no-slip and impermeable walls.

---

Table 3: Domain information and flow property.

$KC$	$\beta$	$U_a$	$T$	$D$	Domain size ( $L_x \times L_y \times L_z$ )/ $D$
2	200	1	2	1	41.6×20.8×4.16

### 5.3.1 Validation of $C_D$ and $C_M$

Table 4: A collection of relevant studies of the case  $KC = 2, \beta = 200$ .

Study	Domain size in cross-section plane	$L_z/D$	$C_D$	$C_M$
Bearman [38]	-	-	1.7	2.15
Justesen [39]	-	-	1	2.15
Zhang and Dalton [13]	-	2.25	1.36	2.05
An [14]	40D × 20D	4	1.32	2.23
Rashid [40]	30D × 10D	3 and 4	0.868	2.14
Justesen [41]	40D × 20D	4	0.949	2.08
Yang [42]	40D × 20D	4	1.418	2.15
Validation	40D × 20D	4	1.369	2.12

For oscillating flows, results can be validated by comparing Morison’s force coefficients with existing results (Jiang [36]). The  $C_D$  and  $C_M$ , obtained by curve-fitting of Morison’s equation (Equation (24)), are used as criteria to conduct an investigation into the validation of the simulation. The results in Table 4 show that  $C_M$  from the present work and all these studies are in a small range close to 2.15, while the  $C_D$  varies with each case. The lowest value of  $C_D$  0.868 was found by Rashid [40] which is almost twice smaller than the largest  $C_D$  1.7 obtained by Bearman [38] in his experiment. This widely spread  $C_D$  are commonly found in similar studies, and Jiang [36] explained the reason for such sensitivity of  $C_D$  in his study. Jiang found that the wide  $C_D$  range is most likely due to the different fitting algorithms used in different studies, especially for  $KC = 2$ . At  $KC = 2$ , the drag force only has a small weight in total inline force. As a result, the  $C_D$  is sensitive to inaccuracies and can not serve as a reliable validation parameter. On the other hand, due to the large weights in inline force,  $C_M$  is not sensitive to such inaccuracies and can be used as a reliable validation criterion. One thing worth noting: among these studies shown in Table 4, only Bearman [38] obtained  $C_D$  and  $C_M$  by conducting experiments, while the other studies are all based on numerical simulations. Compared to experimental results, the numerical simulations tend to under-predict  $C_D$ , and this phenomenon was also found by Justesen [39].

### 5.3.2 Validation of Honji vortices

Since Honji [6] first observed spanwise mushroom-shaped structures caused by the three-dimensional instability in flows. Many experiments and numerical simulations of the Honji vortices have been done by researchers. These studies on Honji instability provide us with enough information to conduct validations of our numerical model.

Figure 21 shows the evolution of velocity  $w$  for our simulation with  $KC = 2, \beta = 200$ . The simulation takes 320 flow periods, and the flow development can be divided into three phases. In the first phase, the transition of two-dimensional flow to three-dimensional flow is complete instantly, but the evenly distributed Honji vortices do not appear. Then, with the further development of the flow, eight equally distributed vortex pairs form in the spanwise direction in phase two. However, the vortex pairs in phase two are not stable, and they tend to interact with each other. As a result, two vortex pairs merge with their neighboring vortex pairs, and then, at the end of this phase, only six evenly distributed vortex pairs are left. This merging of vortices are not observed by Jiang [36], but found by An [14](shown in Figure 22). In his study, Jiang [36] found the Honji vortices in the flow with  $KC = 2, \beta = 200$  are on the edge of instability. Therefore, differences in NS solver and

simulation set-ups may cause different results. The Honji vortices in phase three are stable, but the vortex pairs change their positions in the spanwise direction as time goes by. This re-arranged phenomenon is shown clearly in Figure 23 - Figure 24.

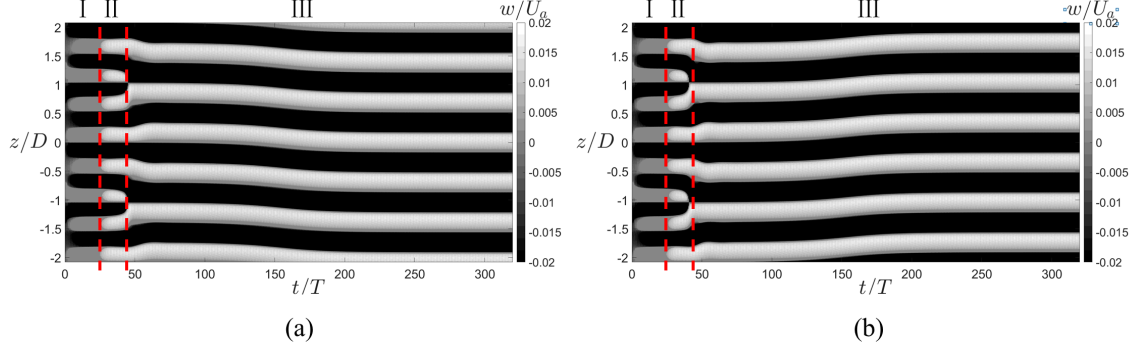


Figure 21: Temporal and spatial evolution of the spanwise velocity component  $w$ . (a) shows  $w$  along the line  $x/D = 0$ ,  $y/D = 0.52$  and (b) shows  $w$  along the  $x/D = 0$ ,  $y/D = -0.52$ .

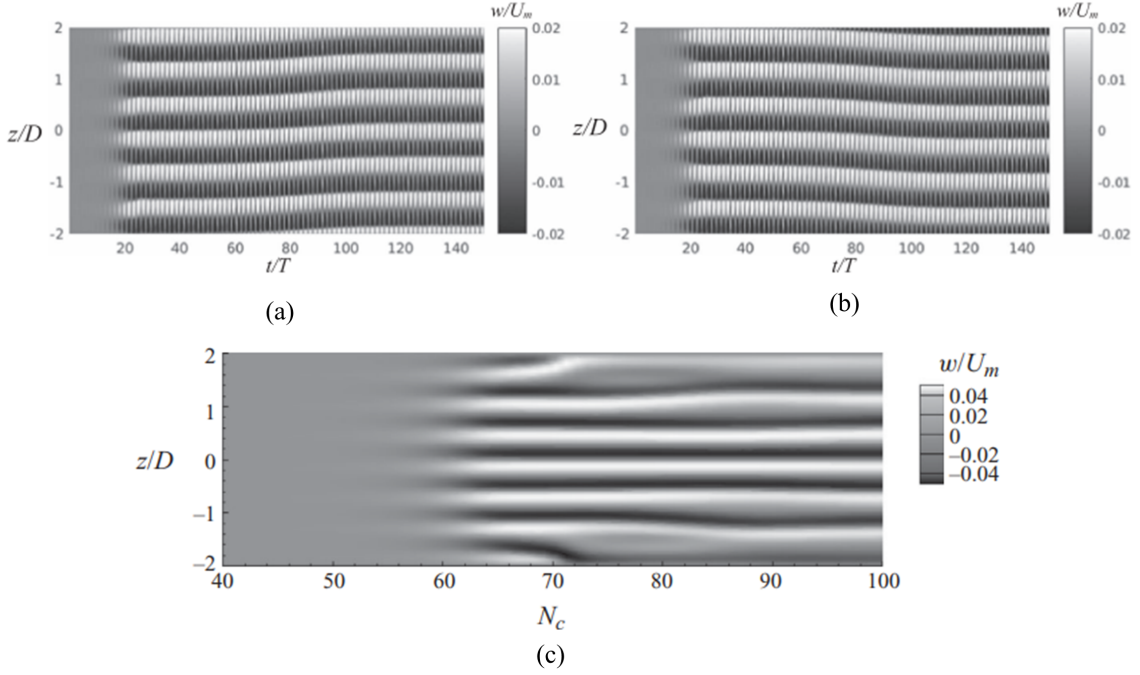


Figure 22: Temporal and spatial evolution of the axial velocity component  $w$ . (a) and (b) are reprinted from Jiang [36] and (c) is reprinted from An [14].

The vorticity isosurfaces around the cylinder are illustrated in Figure 23 - Figure 25. Each pair of rotating vortices represent the stable Honji vortices. For components  $\omega = \pm 1$ , Yang [42] found two-layered vortex pairs in his study (shown in Figure 26). The rib-like top-layer are also presented by An [14] (shwon in Figure 25 (a)) and our simulation results((a) in Figure 23 and Figure 24), while the bottom layer attached to the cylinder only appear observed by Yang [42]. In the initial phase 3(shown in Figure 21), the vortex pairs are symmetrically placed at the two sides of the cylinder. As mentioned before, the vortex pairs are re-arranged as time goes by. In this re-arranged process, the vortex pairs on the two sides of the cylinder move in the opposite direction. At the end of the re-arranged process, the vortex pairs become staggered at two dies of the cylinder.



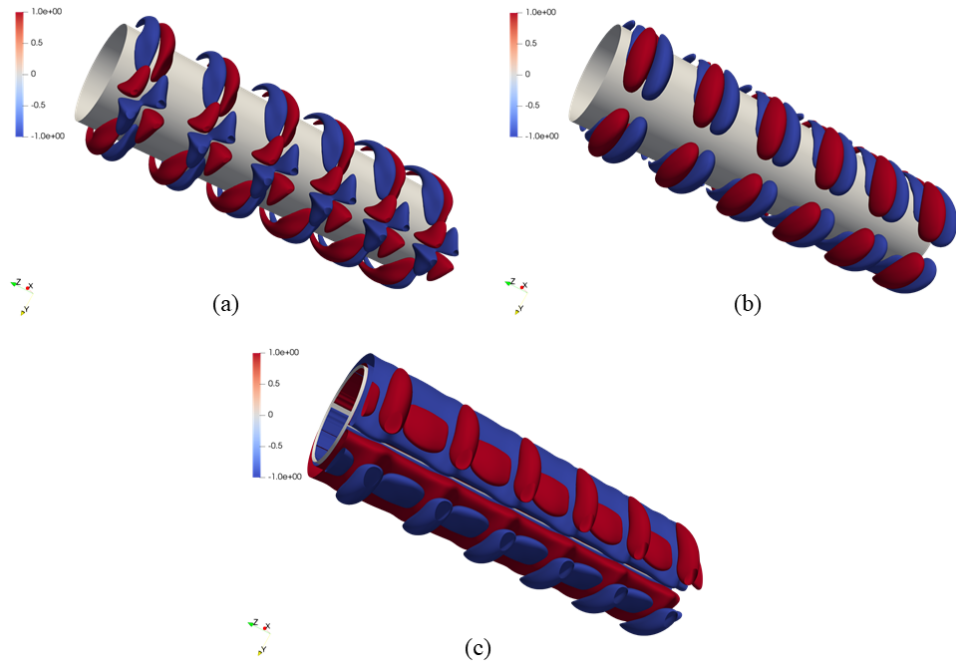


Figure 23: Vorticity isosurfaces around the cylinder when  $KC = 2, \beta = 200$  and at time  $t/T = 120$ . (a-c) are the components  $\omega_x = \pm 1, \omega_y = \pm 1$  and  $\omega_z = \pm 1$  respectively.

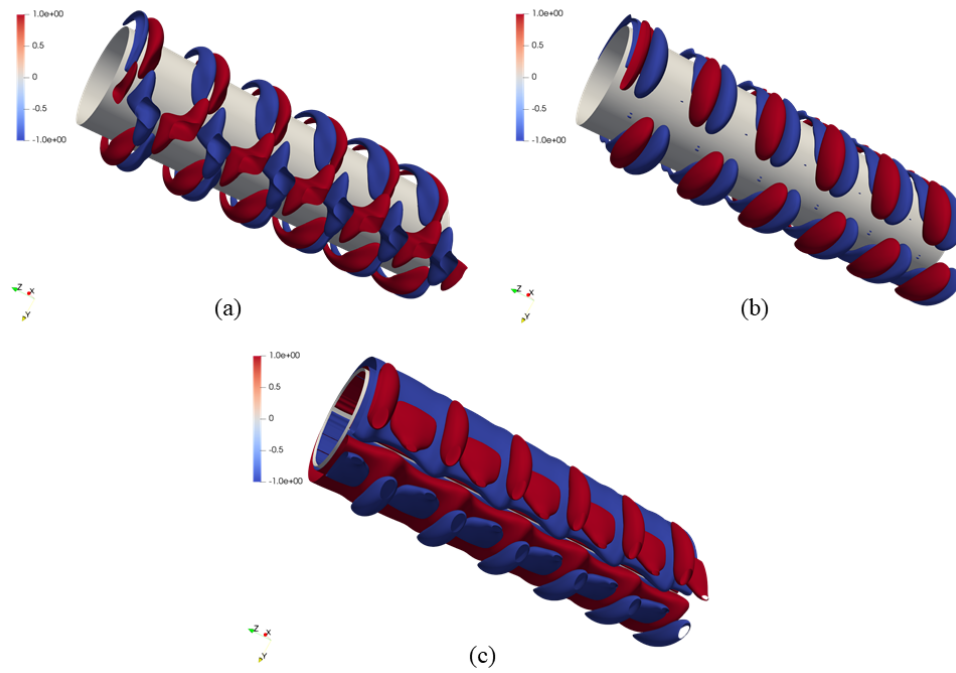


Figure 24: Vorticity isosurfaces around the cylinder when  $KC = 2, \beta = 200$  and at time  $t/T = 220$ . (a-c) are the components  $\omega_x = \pm 1, \omega_y = \pm 1$  and  $\omega_z = \pm 1$  respectively.

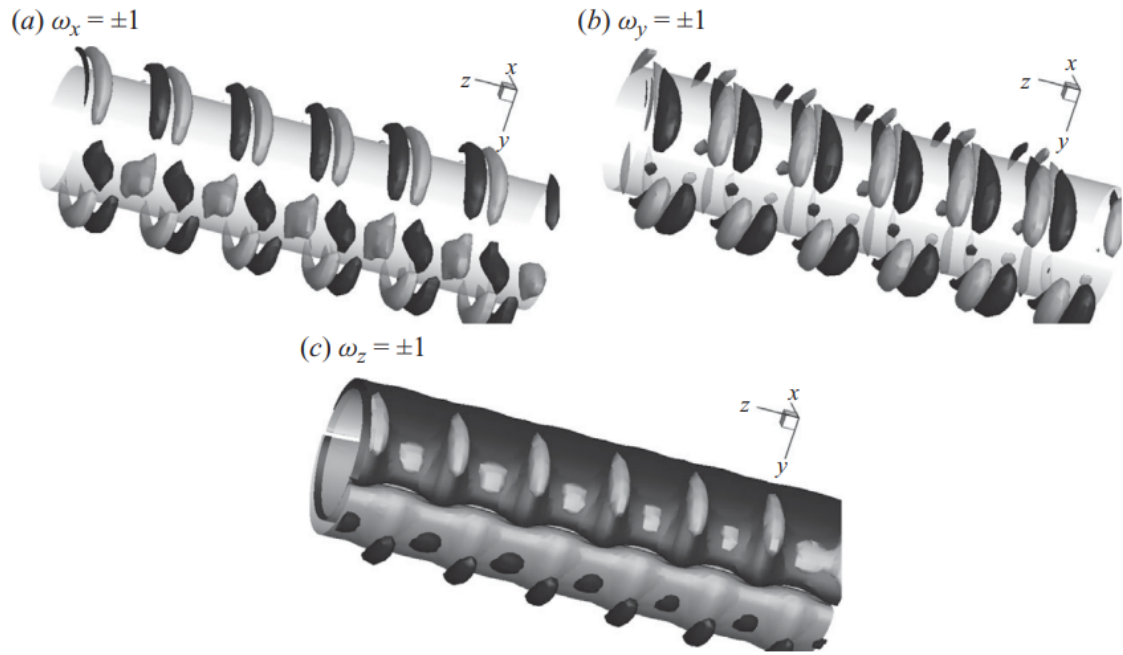


Figure 25: Vorticity isosurfaces around the cylinder when  $KC = 2, \beta = 200$  and at time  $t/T = 220$ . (a-c) are the components  $\omega_x = \pm 1, \omega_y = \pm 1$  and  $\omega_z = \pm 1$  respectively. Reprinted from An [14].

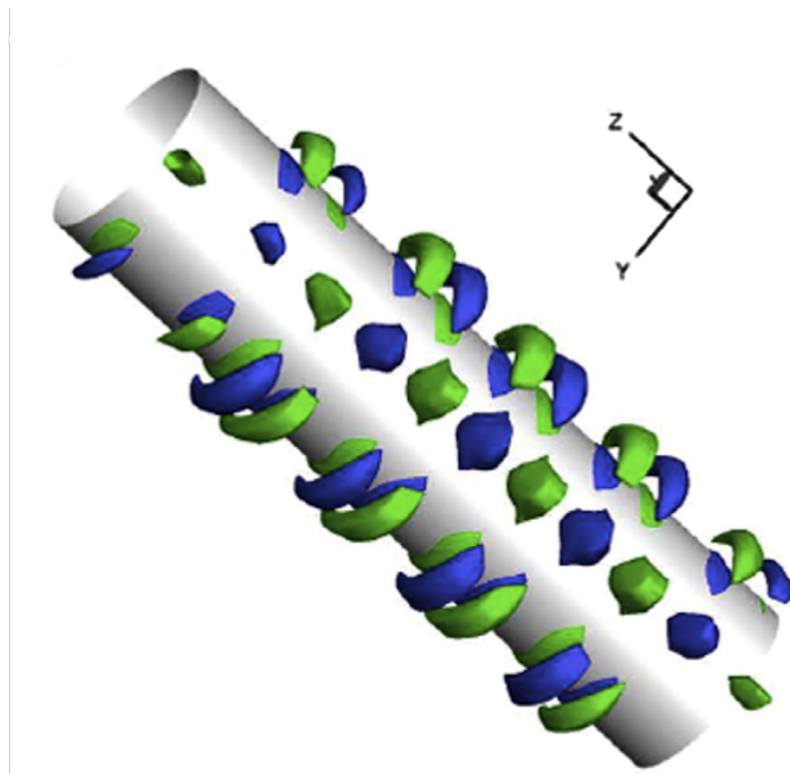


Figure 26: Vorticity isosurfaces of x component ( $\omega_x = \pm 1$ ) around the cylinder when  $KC = 2, \beta = 200$  and at time  $t/T = 220$ . Reprinted from Yang [42].

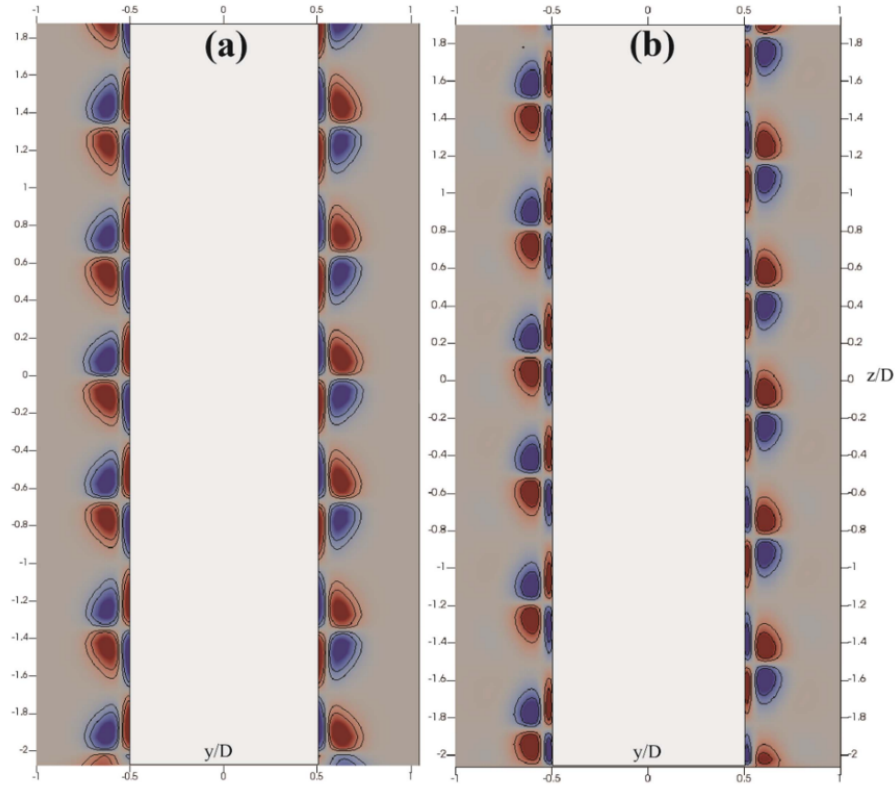


Figure 27: The crosssection of the Honji vortices in  $(y,z)$ -plane at  $x/D = 0$ . Reprinted from Jiang [36].

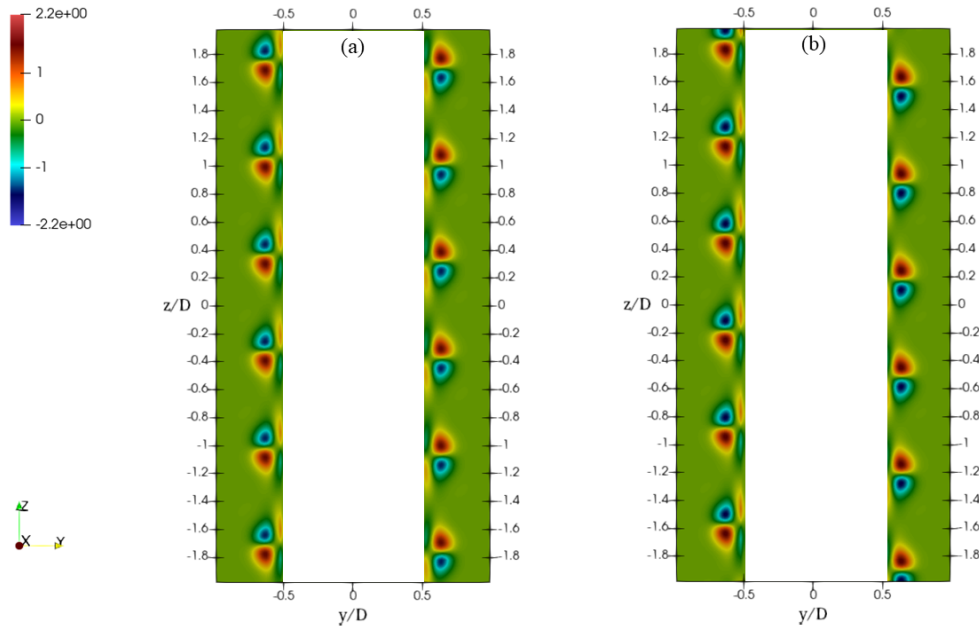


Figure 28: Streamwise vorticity distribution in the  $(y,z)$ -plane at  $x/D = 0$ . (a)  $t = 240$ , (b)  $t = 440$ .

Finally, it is worth noting the spacing  $\lambda$  between vortices. The  $\lambda$  may vary with studies even though they have the same flow properties, domain size, and cylinder length. Yang [42] found five vortex pairs while the present study and Jiang [36] both obtained six vortex pairs. The Sarpkaya

---

[8] quantified the  $\lambda$  over a range of  $\beta$  and he got an empirical relationship between  $\beta$  and  $\lambda$  that  $\lambda \sim 22D\beta^{-3/5}$ . However, the later study done by An [14] found the  $\lambda$  is independent of  $\beta$  when  $KC = 2.09$  and he quantified the influence of  $KC$  number on  $\lambda$  that  $\lambda \sim 0.2D(KC)^{7/4}$ . Our  $KC$  is close to 2.09, so according to An's estimation, our  $\lambda/D$  is about 0.673, which is six vortex pairs for cylinder length  $L_z = 4D$ . This result is consistent with the present study.

## 5.4 Convergence test

In the process of CFD Modeling, simulation and analysis, the grid is an important role as the numerical solver. The choice of the gridding methodology is not only critical for computation, but also determine the spatial resolution of the flow field. Generally, the basic requirement of grid generation is to capture the geometry and the details of the flow structures, etc. As a consequence, the grid should be fine enough to get accurate results. However, a very fine grid normally results larger grid generation and computing time, and thus lead to increases in computational hardware requirement. To solve this dilemma, the break-even point, in which the grid is fine enough to make accurate predictions and the cost of time and computational resources is acceptable, should be determined according to aims and requirements of each individual numerical simulation projects. Thus, before conducting a full-scale production numerical simulation, it is necessary to perform a grid convergence test. In present grid convergence test, three levels of grids: coarse(0.02D), medium(0.016D) and fine(0.01D) are used. The results of the grid convergence study are shown in Figure 29(c) and Figure 30(c). The maximum relative errors of the phase average velocity  $u/U_a$  between each grids occur around  $y/D = -0.5D$ , and the value of the relative error is 2.49% between fine and medium grids and is 4.19% between fine and coarse grids. The reason that the maximum relative errors appear around  $y/D = -0.5D$  is that the presence of the step induces unwanted three-dimensionality to the larger cylinder, and thus results greater disturbance of the phase average velocity  $u/U_a$ .

As mentioned in boundary conditions section, if the non-physical boundaries are placed near to the step cylinder, they can cause unwanted influences on the results and constitute a source of error in the numerical simulation. However, due to constraints of computational time and power, the computational domain cannot be infinitely large either. Thus, the compromise between accuracy of solution and computational cost results the need for domain convergence test. In the domain convergence test, the streamwise length  $L_x$  and the transverse width  $L_y$  varies from  $19.2D$  to  $51.2D$  and from  $12.8D$  to  $32D$ , respectively. The phase average velocity profiles of  $u/U_a$  and  $v/U_a$  illustrated in Figure 29(a) and Figure 30(a) shows that the domain with  $L_x = 51.2D$  and  $L_y = 32D$  is suitable for the final numerical simulation.

The residuals of the governing equations should be reduced up to get theoretically vanishing to achieve the time step convergence. If the time step is not small enough, it could lead to numerical error that may affect the initial conditions for the next time step. Normally for explicit schemes a large time step may cause instability and results an unacceptable CFL number. The implicit schemes are generally unconditionally stable and the time step affects the accuracy. Three different time step are tested in this project and they are  $\Delta t u/D = 0.002$  for smallest time step,  $\Delta t u/D = 0.003$  for medium time step and  $\Delta t u/D = 0.004$  for largest time step. The phase average velocity profiles of  $u/U_a$  and  $v/U_a$  illustrated in Figure 29(b) and Figure 30(b) and the CFL number illustrated in Figure 18 show that the smallest time step with value of  $\Delta t u/D = 0.002$  achieves the time step convergence.

For a numerical simulation of a uniform circular cylinder placed in oscillatory flow, the top and bottom boundaries can be set to periodic boundary condition. For case with periodic boundary condition at the top and bottom boundary, due to the cyclic situation of the flow across the periodic boundary surface, the length of uniform circular cylinder can be considered to be infinite long. However, for a step cylinder, the flow features around the small cylinder near the top boundary are different than those around the large cylinder close to the bottom boundary. As a result, the periodic boundary condition can not be applied to the present numerical simulation, and thus the length of small and large cylinder matters. As mentioned in domain convergence test, the length of both small and large cylinder must be large enough enough to prevent the boundary effects from the flow structures near the step. Three step cylinders with different length are tested in present

study. The phase average velocity profiles of  $u/U_a$  and  $v/U_a$  shown in Figure 29(d) and Figure 30(d) are similar to those in grid convergence test. The flow features below the step are also sensitive to the length of the step cylinder. Although, closed to  $y/D = -0.5D$ , there is an relative error 2.34% between maximum phase average velocity  $u/U_a$  of longest and medium-lengthed cylinder, the solutions are well within the asymptotic range of convergence.

The Figure 29 and Figure 30 and Table 5 shows the results and the details of setting of convergence tests. Although the black line has different names in sub figures, it represents the results of the fine case listed in Table 5. The red dotted line in the sub figures to the medium case in different convergence tests, and the blue dash line in the sub figures correspond to the coarse, small, large and short case in grid, domain, time step and geometric convergence test, respectively.

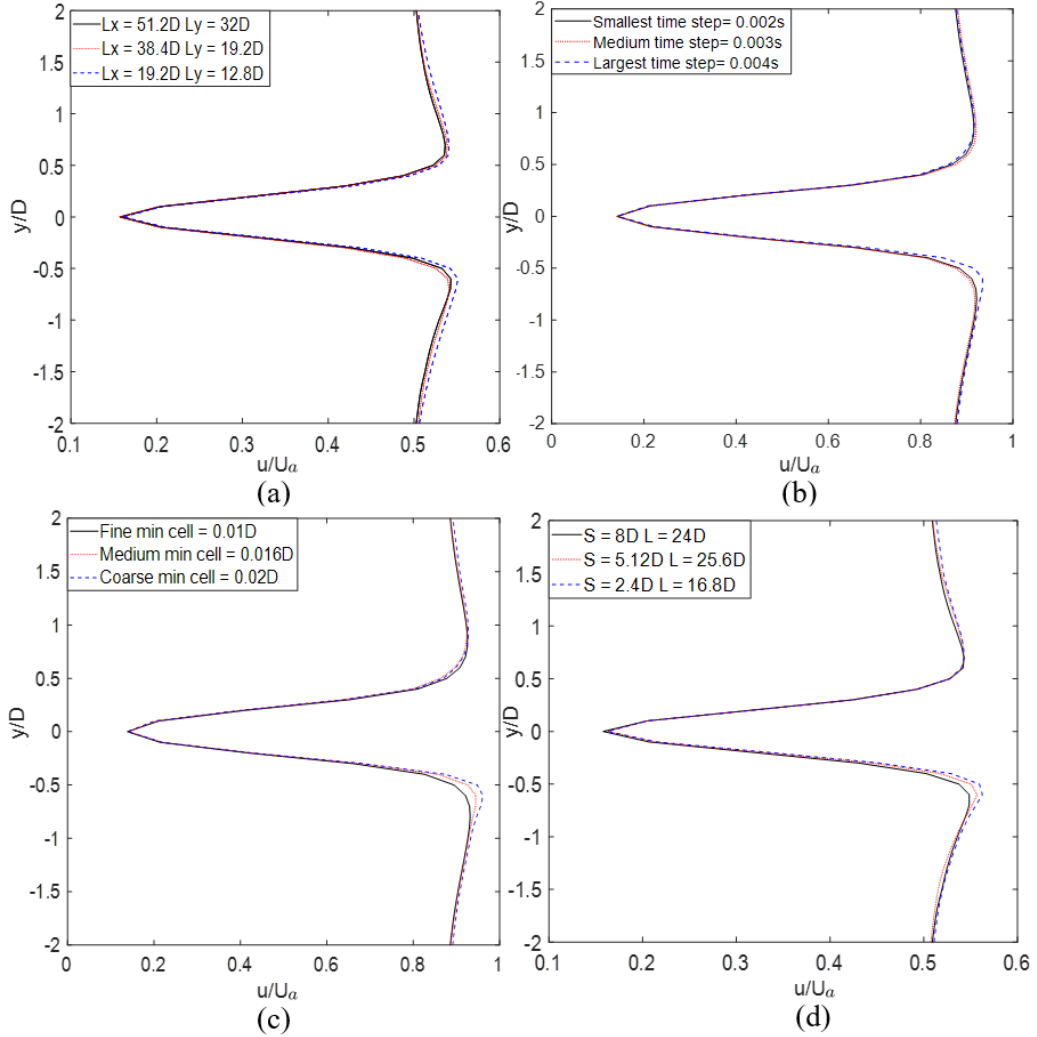


Figure 29: The phase average velocity  $u/U_a$  at streamwise location  $x/D = 0.6D$ , spanwise location  $z/D = -6.2$  calculated using properties listed in Table 5 and using parameter values  $KC = 2.8$ ,  $\beta = 80$  with time range from  $t = 365T$  to  $t = 465T$ . The sub figures (a), (b), (c), (d) are results of domain, time step, grid and geometry convergence tests, respectively. The phase angle for each case is (a)  $\theta = 57.85^\circ$ , (b)  $\theta = 101.83^\circ$ , (c)  $\theta = 101.83^\circ$ , (d)  $\theta = 57.85^\circ$ .

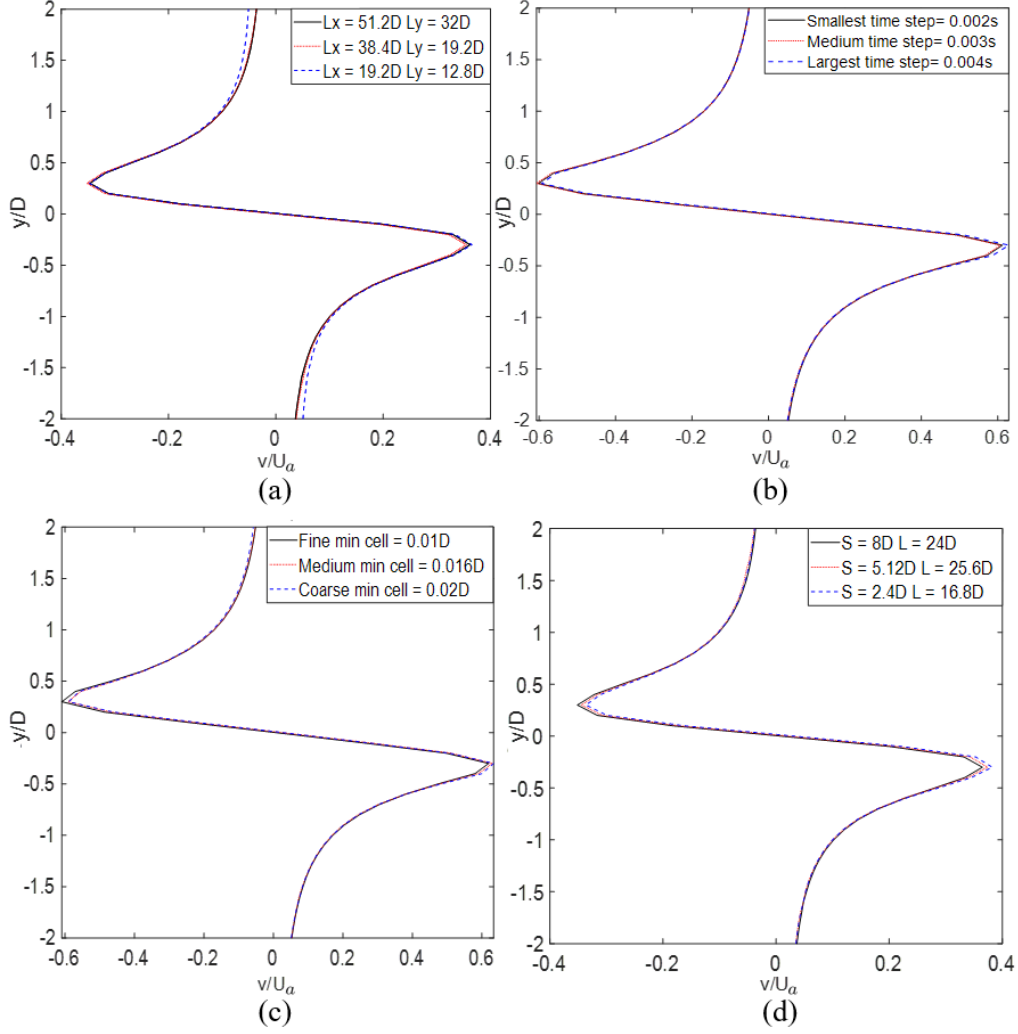


Figure 30: The phase average velocity  $v/U_a$  at streamwise location  $x/D = 0.6D$ , spanwise location  $z/D = -6.2$  calculated using properties listed in Table 5 and using parameter values  $KC = 2.8$ ,  $\beta = 80$  with time range from  $t = 365T$  to  $t = 465T$ . The sub figures (a), (b), (c), (d) are results of domain, time step, grid and geometry convergence tests, respectively. The phase angle for each case is (a)  $\theta = 57.85^\circ$ , (b)  $\theta = 101.83^\circ$ , (c)  $\theta = 101.83^\circ$ , (d)  $\theta = 57.85^\circ$ .

Table 5: Details of convergence tests

	Case	min cell (D)	time step (s)	Lx (D)	Ly (D)	Lz (D)	S (D)	L (D)
Grid convergence test	Fine	0.01	0.002	51.2	32	32	8	24
	Medium	0.016	0.0032	51.2	32	32	8	24
	Coarse	0.02	0.004	51.2	32	32	8	24
Domain convergence test	Medium	0.01	0.002	38.4	19.2	32	8	24
	Small	0.01	0.002	19.2	12.8	32	8	24
Time step convergence test	Medium	0.01	0.003	51.2	32	32	8	24
	Large	0.01	0.004	51.2	32	32	8	24
geometric convergence test	Medium	0.01	0.002	51.2	32	25.6	5.12	20.48
	Short	0.01	0.002	51.2	32	19.2	2.4	16.8

---

## 6 Results and discussion

The results presented in this chapter obtained from the simulation of oscillatory flow around a step cylinder. As a summary, Table 6 shows the details of the simulations.

Table 6: Details of geometries and parameters

	Large cylinder	Small cylinder
Diameter of cylinder, $D$	1	0.5556
Length of cylinder, $L/D$	24	8
Keulegan–Carpenter number ( $KC$ )	2.8	5.04
Stokes number ( $\beta$ )	80	24.69
Reynolds number ( $Re$ )	224	124.44
Flow regime	B	A

The time steps  $\Delta t u/D = 0.002$  are used and the final simulation was run for 1250 oscillation periods (3500s) of the large cylinder. The results of flow development illustrated in subsection 6.1 show two interrelated long-period phenomena: appearance and merging of Honji vortex. These two long-period phenomena are described in subsection 6.2 and subsection 6.3, respectively.

### 6.1 Flow development at parameters $KC = 2.8$ and $\beta = 80$ for large cylinder

One of the best way to evaluate the evolution of the flow in regime A and B is visualization of the time history of the relative axial (spanwise) velocity. The spanwise velocity  $w/U_a$  is monitored along two probe lines which are parallel to the axis of the cylinder and close to the surface of the step cylinder at  $x/D = 0$ ,  $y/D = 0.52$ , and  $x/D = 0$ ,  $y/D = -0.52$ . Figure 31 shows both the temporal and spatial evolution of the spanwise velocity  $w/U_a$ . The colour shade illustrates the value and direction of  $w/U_a$  which is from -0.08 to 0.08. The region where three-dimensionality occurs can also be observed by the colour shade structures.

The Figure 31 and Figure 32 shows that, according to the variation of the spanwise velocity, the flow near the step cylinder appears different patterns in up, interface and bottom zone. In the up zone where  $1 < z/D < 8$ , the flow are slightly affected by the three-dimensionality caused by the presence of the step. There are no complex three-dimensional dynamics in this up zone and the flow remains two-dimensional. All in all, the flow in the up zone has the same pattern as it has in the regime A of the case of oscillatory flow around a uniform cylinder.

It is clear that there is great variation of the spanwise velocity  $w/U_a$  in the interface zone around  $-1 < z/D < 0.9$ . The interface zone shown in Figure 32 is separated into three parts I, II and III by lines perpendicular to the axis of the cylinders at  $z/D = 0.3$  and at  $z/D = 0$ . In the part I, the spanwise velocity  $w/U_a$  reaches its maximum value 0.08 with upward direction every 2.8s. The appearance of the maximum spanwise velocity means that the flow has strongest three-dimensionality in part I. However, outside the part I those upward three-dimensional dynamics dissipate fast and cause slight effects on the flow in up zone. The part II  $0 < z/D < 0.3$  is where the most intense variation of the spanwise velocity happens. Within 0.7s, the value of spanwise velocity  $w/U_a$  decreased from the maximum to zero, and then increases again to the maximum, but in the opposite direction. Such great variation of the spanwise velocity occurs every 1.4s, which is equal to half the oscillation period of the flow. The part III is the largest part of the three parts. In this part the spanwise velocity  $w/U_a$  reaches its maximum value every 2.8s as in part I. However, unlike it in part I, the three-dimensionality is stronger in part III and tends to affects the flow patterns in downward zone.



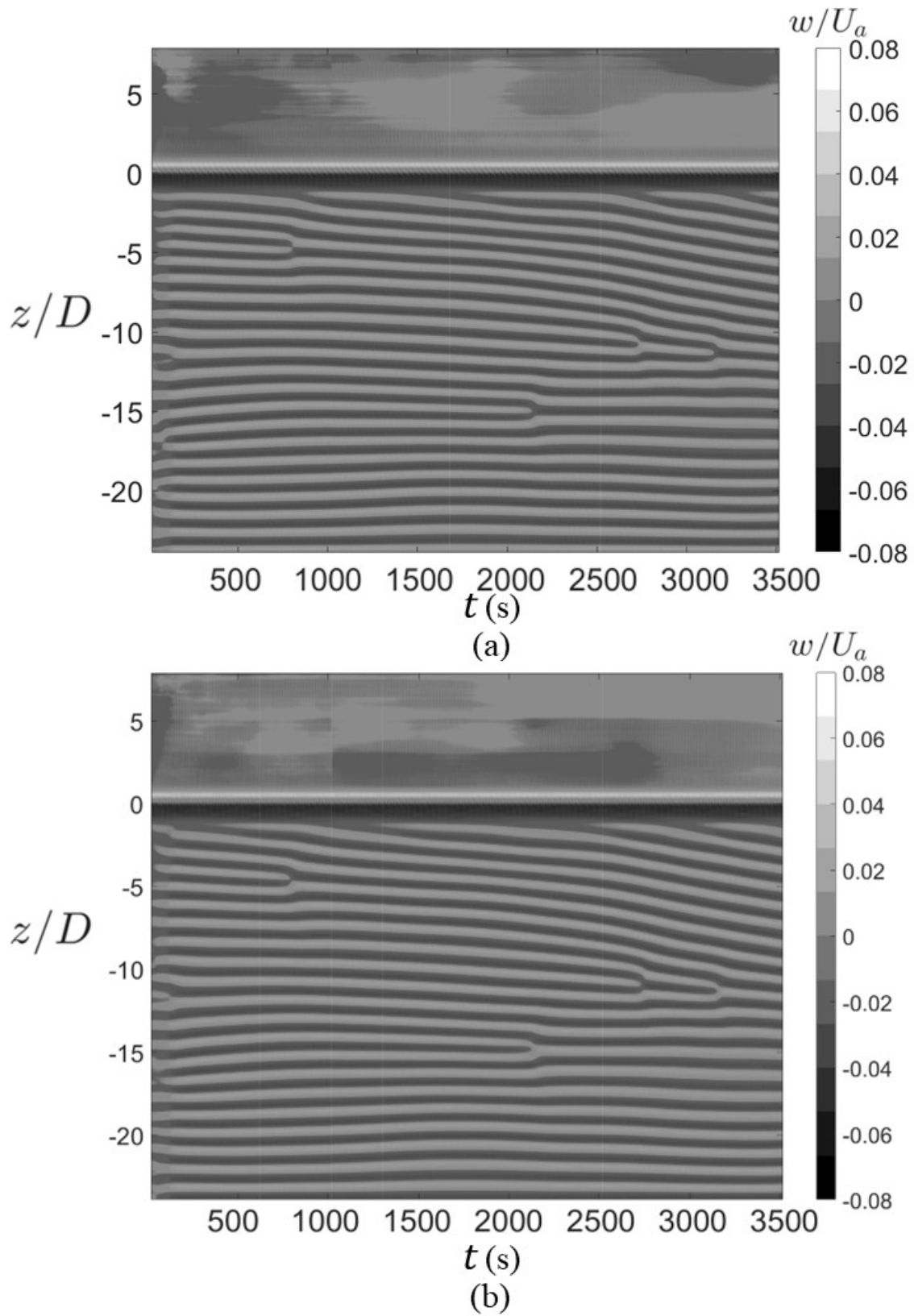


Figure 31: Temporal and spatial evolution of the spanwise velocity component  $w/U_m$ . (a) shows  $w/U_m$  along the line  $x/D = 0$ ,  $y/D = 0.52$  and (b) shows  $w$  along the  $x/D = 0$ ,  $y/D = -0.52$ .



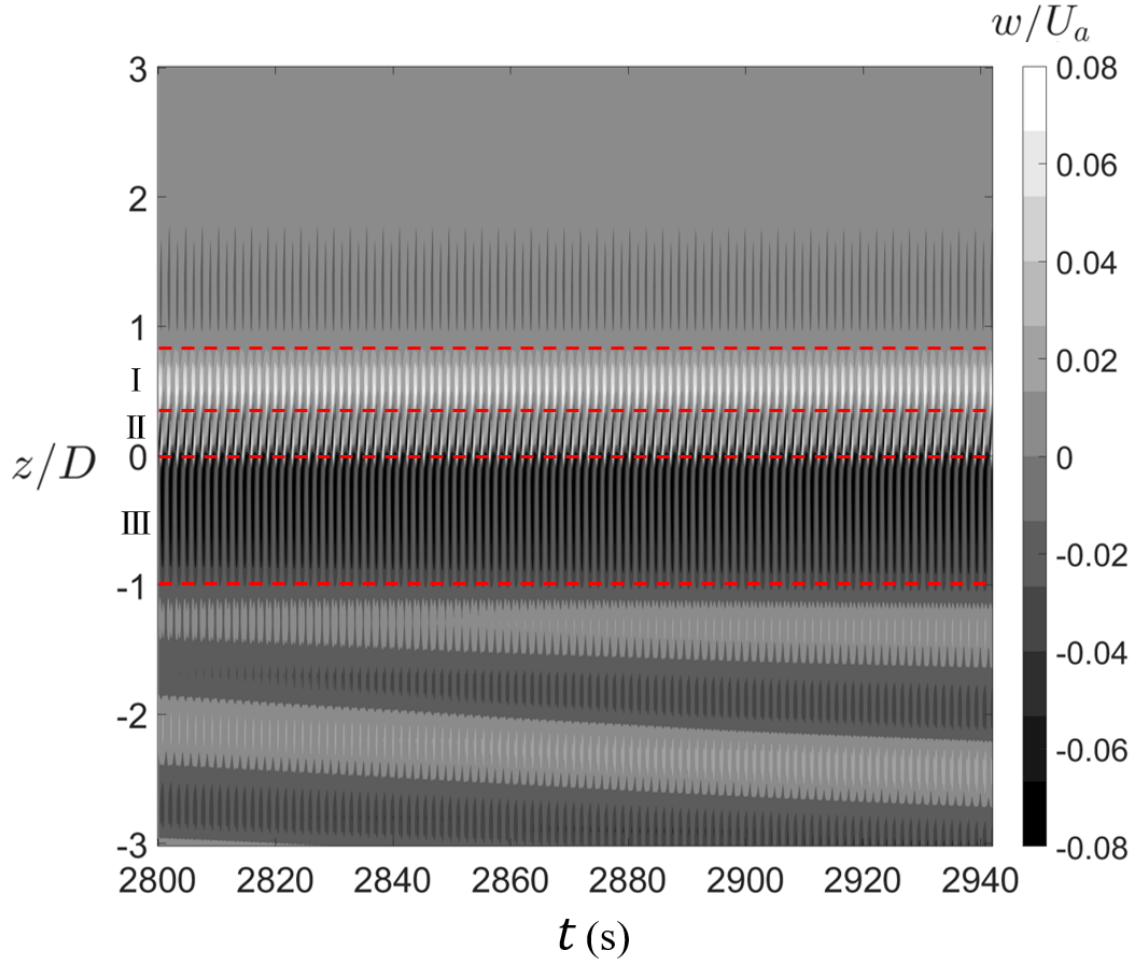


Figure 32: Zoomed-in temporal and spatial evolution of the spanwise velocity component  $w/U_m$  along the line  $x/D = 0$ ,  $y/D = 0.52$ .

Although having different flow parameters  $KC$  and  $\beta$ , the flow in the bottom zone ( $-24 < z/D < -1$ ) has similar patterns to those mentioned in the previous subsection 5.3.2 such as the evenly distributed Honji vortex pairs and the merging process of Honji vortex. However, the development and the phase of the flow structures are great different from those in the oscillatory flow around a uniform cylinder with parameters  $KC = 2$  and  $\beta = 200$ . At the start of the simulation, the flow in bottom zone does not remain two-dimensional. The three-dimensionality appears in the flow at the beginning of oscillation of flow and after around 50 periods of oscillation the colour shade stripes along the cylinder span show that the three-dimensionality is evenly distributed spanwise. This uniformly distributed three-dimensionality is called Honji vortex pair. Unlike the stable Honji vortices mentioned in 5.3.2, the number of main Honji vortex pairs changes in present case. At the first time when evenly distributed Honji vortex pairs appear, there are 20.5 Honji vortex pairs shown in Figure 31 (a) and (b). As the time goes by, a new Honji vortex appears at the top of the bottom zone at negative side of y direction shown in Figure 31 (b) and 200s later another new Honji vortex appears at the positive side of y direction, at that time there are 21.5 Honji vortex pairs distributed at both sides of the step cylinder. The Honji vortex pairs at up parts of the bottom zone keep shifting their position downward and squeeze other vortex pairs below them. Then the first merging of two neighbouring vortices is observed around  $z/D = -5$  at both sides of the step cylinder. After about 300s since the first merging of Honji vortex, near the step, a new Honji vortex pair appears at positive y side and then appears at negative y side, and then second merging process occurs. As the time goes by, this kind of long period phenomenon of appearance and merging process keeps happen and the happening time of these processes are listed in Table 7.

Table 7: Oscillatory period number of occurrence of appearance and merging of Honji vortex

	Appearance at $y/D = 0.52$	Appearance at $y/D = -0.52$	Merging
First time, $t/T$	270	75	255
Second time, $t/T$	600	405	735
Third time, $t/T$	940	825	945
Fourth time, $t/T$	1160	1060	1100

## 6.2 Appearance process of Honji vortex

The Figure 33 to Figure 37 show the first appearance process of Honji vortex at positive  $y$  side, starting around  $t/T = 270$ . At the beginning of the appearance process, near the step at positive  $y$  side of the step cylinder, there is no Honji vortex pair, but only a vorticity isosurface with value  $\omega_y = -0.1$  indicates the presence of a newly generated weak vortex. After about 17 periods, the appearance of another vorticity isosurface with value  $\omega_y = 0.1$  shows that a new weak vortex with opposite rotating direction forms above the previous vortex. Although those two newly generated vortices have similar strength and opposite rotating direction, they are not a Honji vortex pair. In fact, in this two newly generated vortices, the lower vortex is actually in pair with the already existing vortex below. As the time goes by, those two newly generated vortices becomes stronger and stronger and keeps pushing other vortices downward. It should be noticed that at the negative  $y$  side of the step cylinder, even though there is no appearance of the vortex, the existing vortex pairs still continue to move downward.

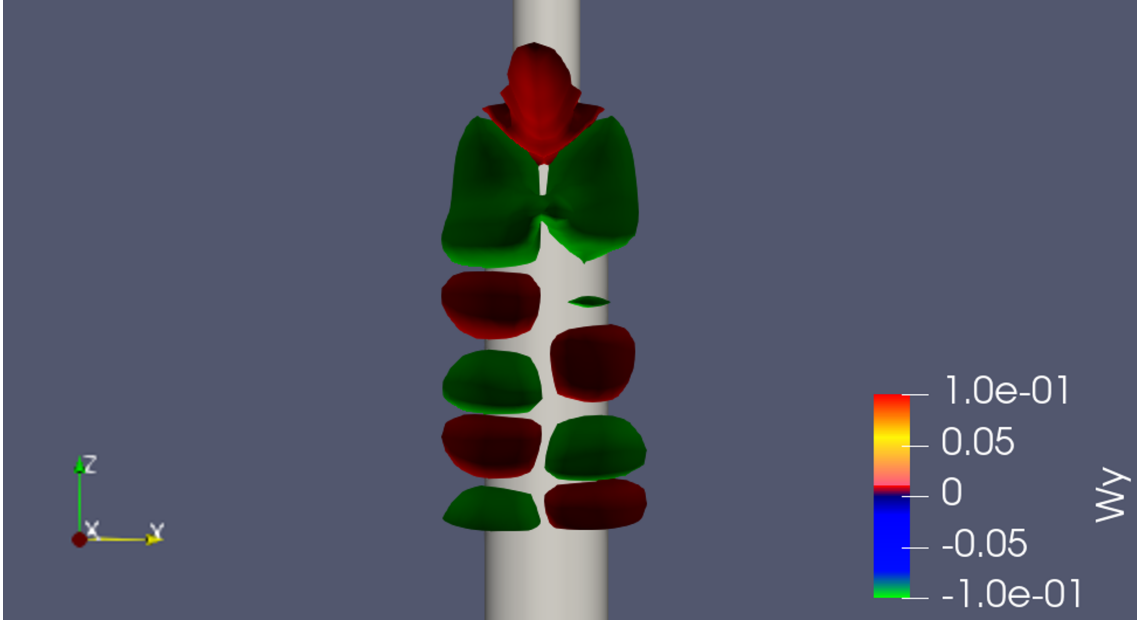


Figure 33: Vorticity isosurfaces  $\omega_y = \pm 0.1$  around the cylinder at time  $t = 760.06s$ , in the range  $-3 < z/D < 0$ .

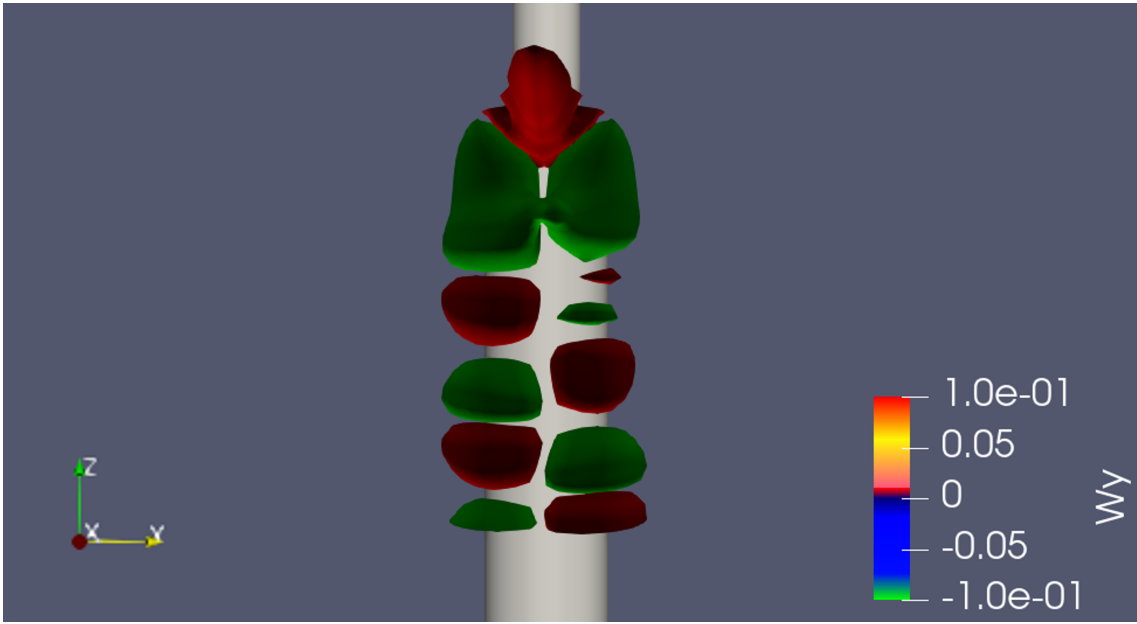


Figure 34: Vorticity isosurfaces  $\omega_y = \pm 0.1$  around the cylinder at time  $t = 807.66s$ , in the range  $-3 < z/D < 0$ .

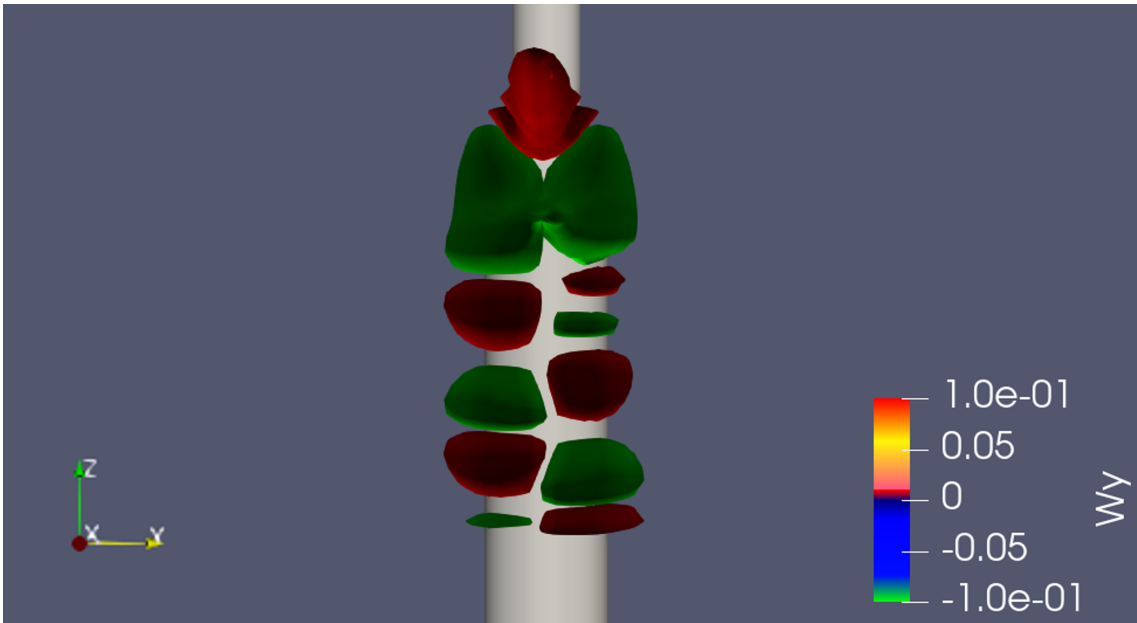


Figure 35: Vorticity isosurfaces  $\omega_y = \pm 0.1$  around the cylinder at time  $t = 838.46s$ , in the range  $-3 < z/D < 0$ .

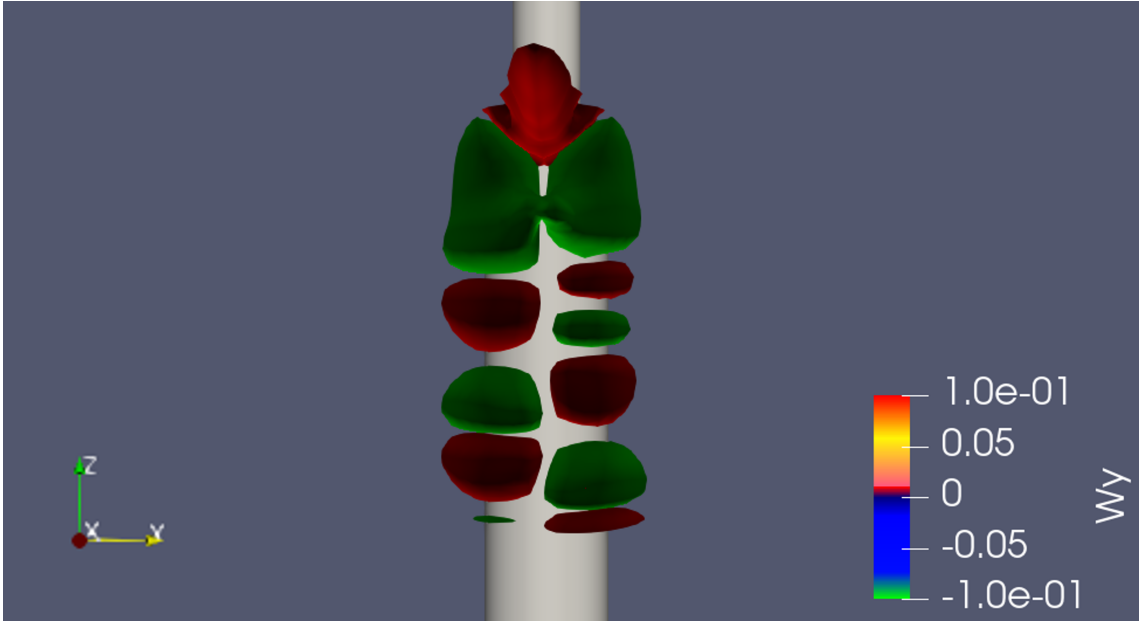


Figure 36: Vorticity isosurfaces  $\omega_y = \pm 0.1$  around the cylinder at time  $t = 857.71s$ , in the range  $-3 < z/D < 0$ .

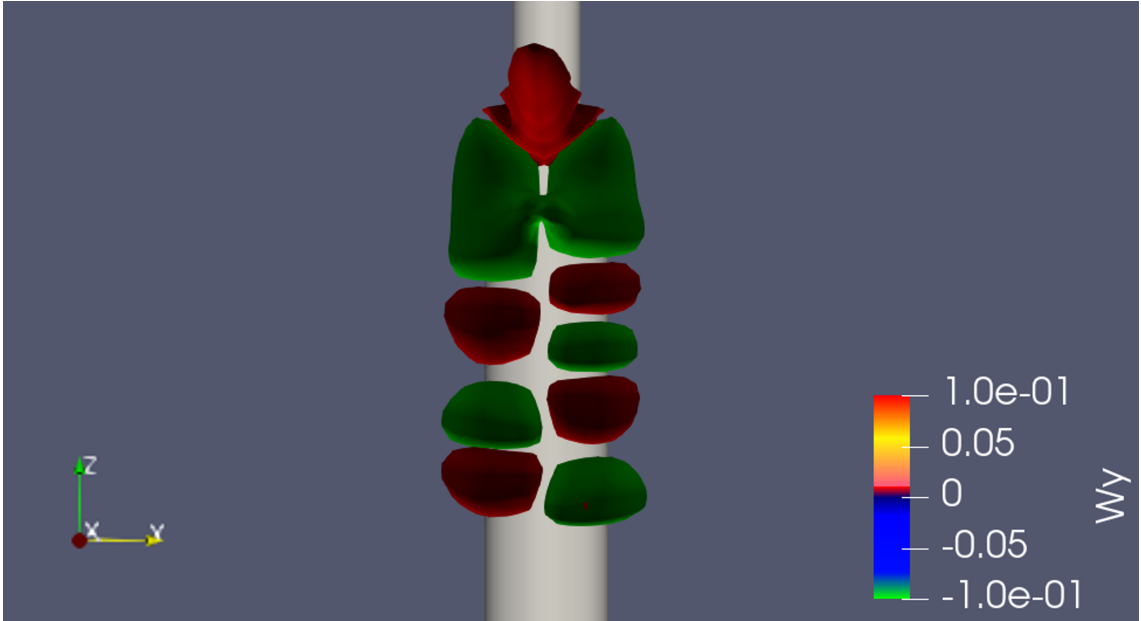


Figure 37: Vorticity isosurfaces  $\omega_y = \pm 0.1$  around the cylinder at time  $t = 919.66s$ , in the range  $-3 < z/D < 0$ .

### 6.3 Merging process of Honji vortex

The Figure 38 to Figure 44 show the first merging process of existing Honji vortex. Unlike the appearance process of Honji vortex only happening at one side of the step cylinder, the merging of Honji vortex occurs at the both sides of the step cylinder at the same time. The vortices involved in the merging process in the range  $-5.5 < z/D < -3.8$  are denoted by  $V1$  to  $V6$ . At the negative  $y$  side,  $V1$  and  $V2$  is a pair of Honji vortex and  $V3$  and  $V4$  is a pair of Honji vortex. At the positive  $y$  side,  $V5$  and  $V6$  is a pair of Honji vortex. At the beginning of merging process, the strength of

$V_2$ ,  $V_3$ ,  $V_5$  and  $V_6$  are all decrease, but the strength of  $V_2$  and  $V_3$  reduces faster. As the time goes by, in the negative y side, the  $V_2$  and  $V_3$  become smaller and smaller, while the other vortex in their pairs  $V_1$  and  $V_4$  are becoming larger and larger. In the other side of the step cylinder, the pair Honji vortex  $V_5$  and  $V_6$  is getting smaller and smaller, while the vortices in the other pairs above  $V_5$  and below  $V_6$  are also become smaller and smaller. As the merging process continues, in the positive y side,  $V_2$  and  $V_3$  are completely cancelled by each other, and the remaining vortices  $V_1$  and  $V_4$  form a new pair of Honji vortex. The  $V_5$  and  $V_6$  in the positive y side also disappears, but the reason that why they disappears can not be told from the Figure 38 to Figure 44.  $V_5$  and  $V_6$  may be cancelled by the vortices with opposite rotating directions in above and below vortex pairs, or they may be cancelled by each other.

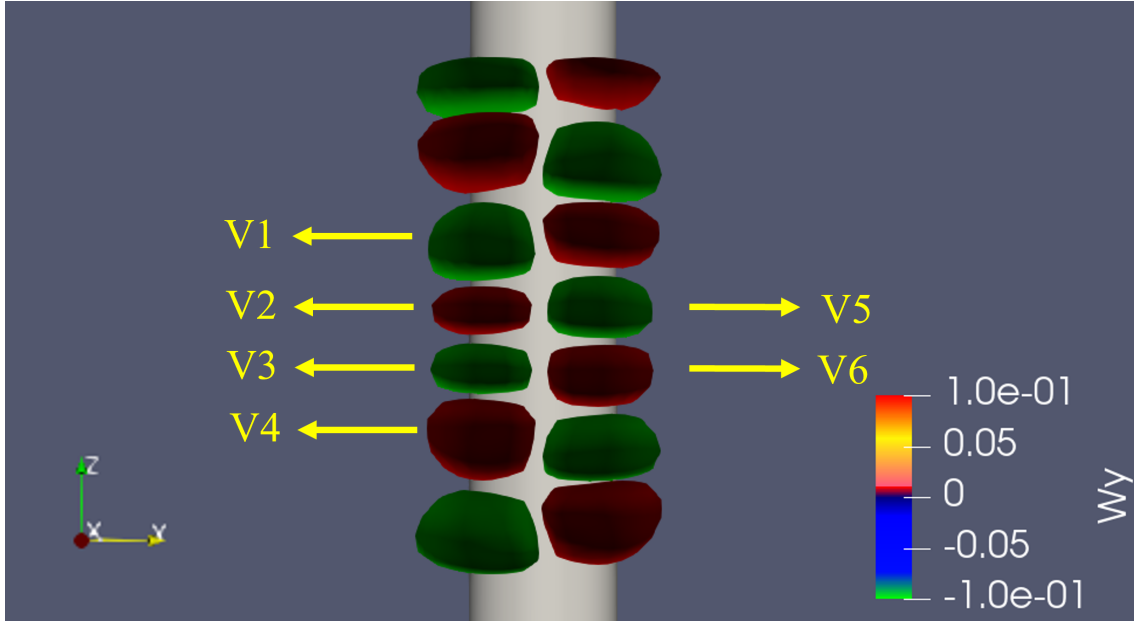


Figure 38: Vorticity isosurfaces  $\omega_y = \pm 0.1$  around the cylinder at time  $t = 776.51s$ , in the range  $-7 < z/D < -3$ .

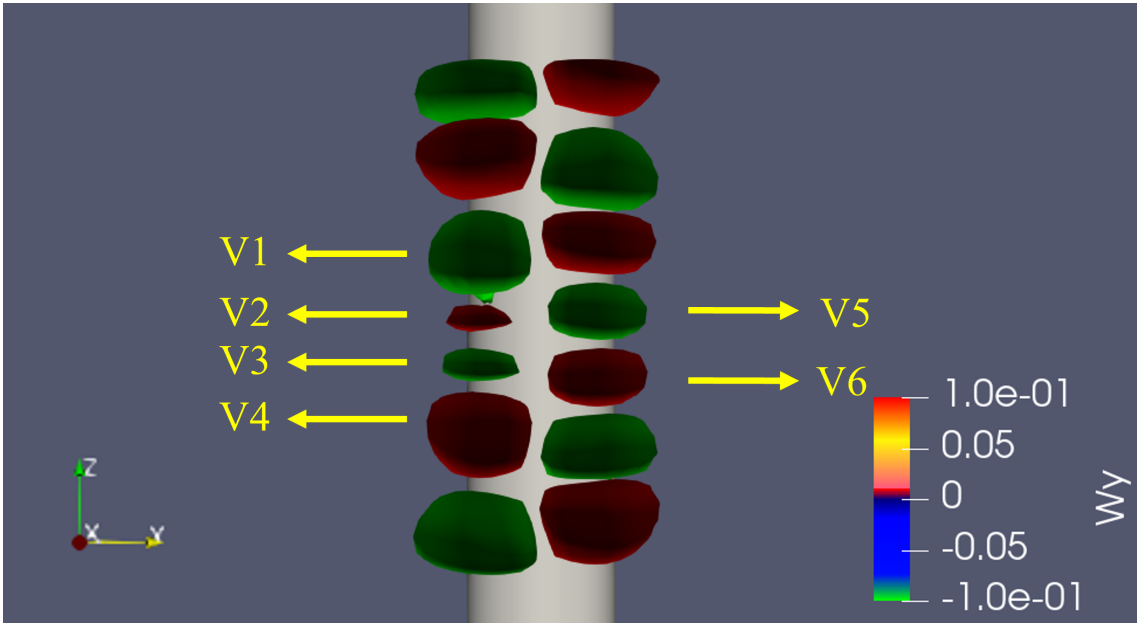


Figure 39: Vorticity isosurfaces  $\omega_y = \pm 0.1$  around the cylinder at time  $t = 787.71s$ , in the range  $-7 < z/D < -3$ .

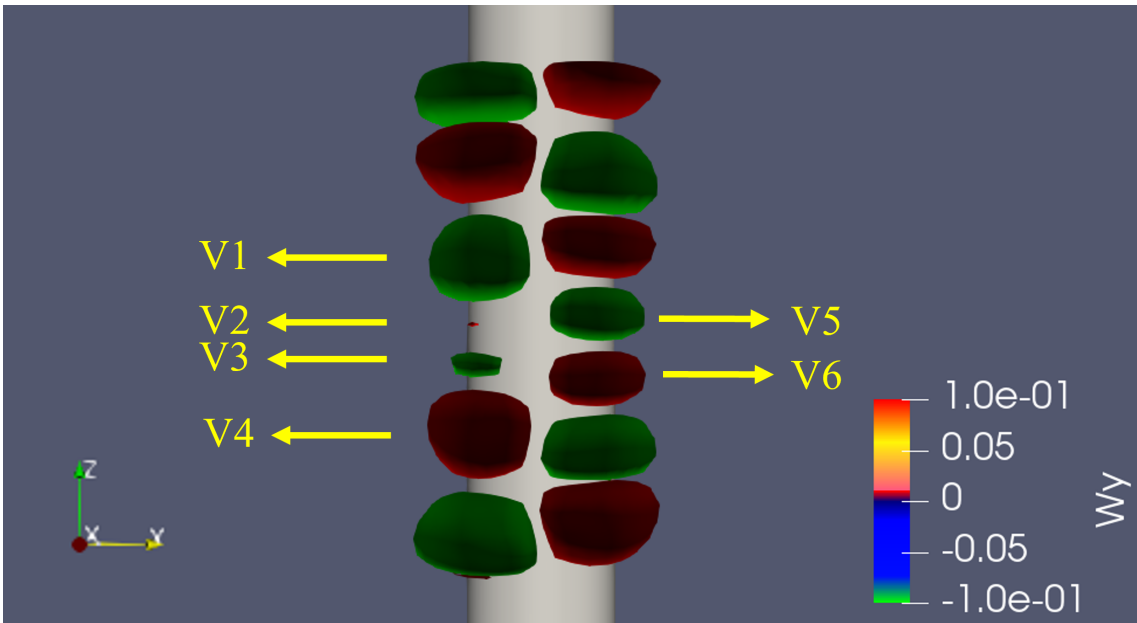


Figure 40: Vorticity isosurfaces  $\omega_y = \pm 0.1$  around the cylinder at time  $t = 790.51s$ , in the range  $-7 < z/D < -3$ .

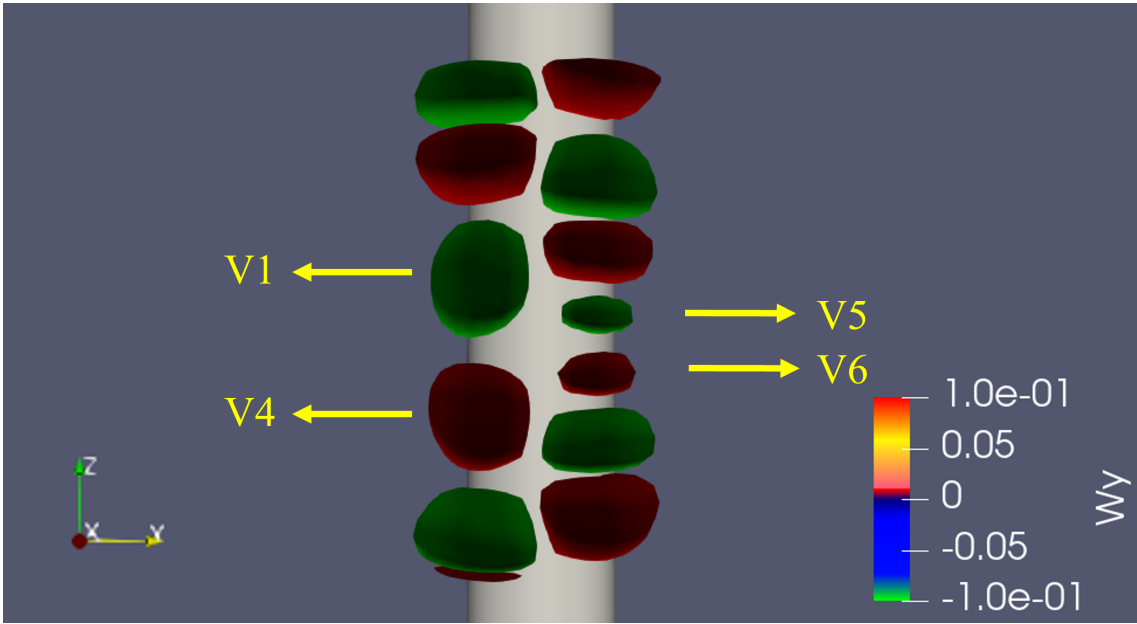


Figure 41: Vorticity isosurfaces  $\omega_y = \pm 0.1$  around the cylinder at time  $t = 798.91s$ , in the range  $-7 < z/D < -3$ .

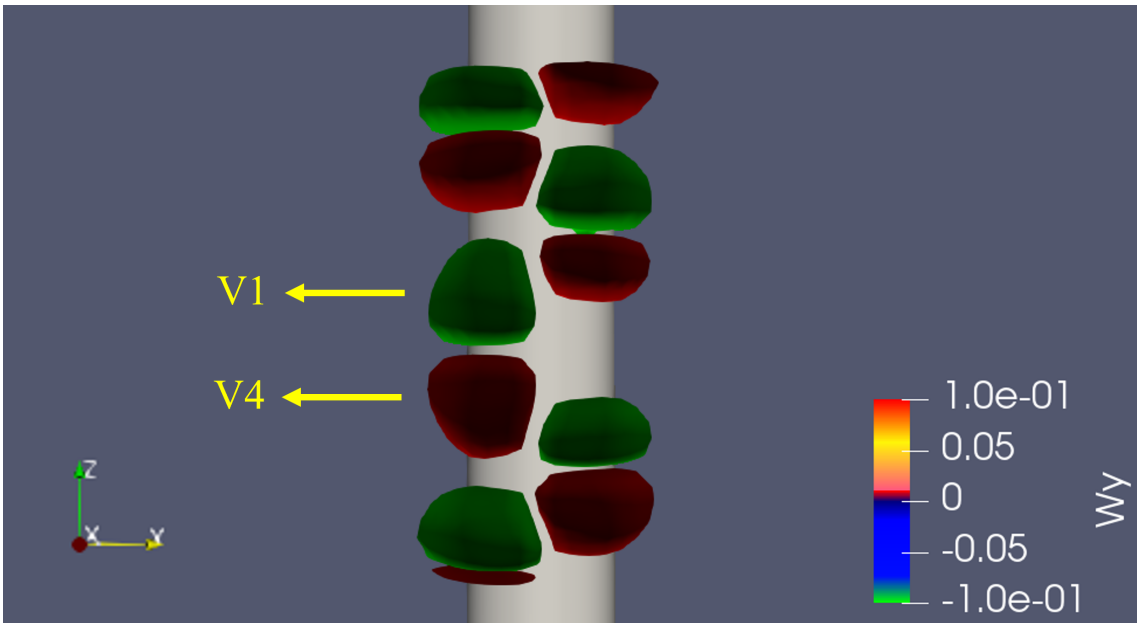


Figure 42: Vorticity isosurfaces  $\omega_y = \pm 0.1$  around the cylinder at time  $t = 807.66s$ , in the range  $-7 < z/D < -3$ .

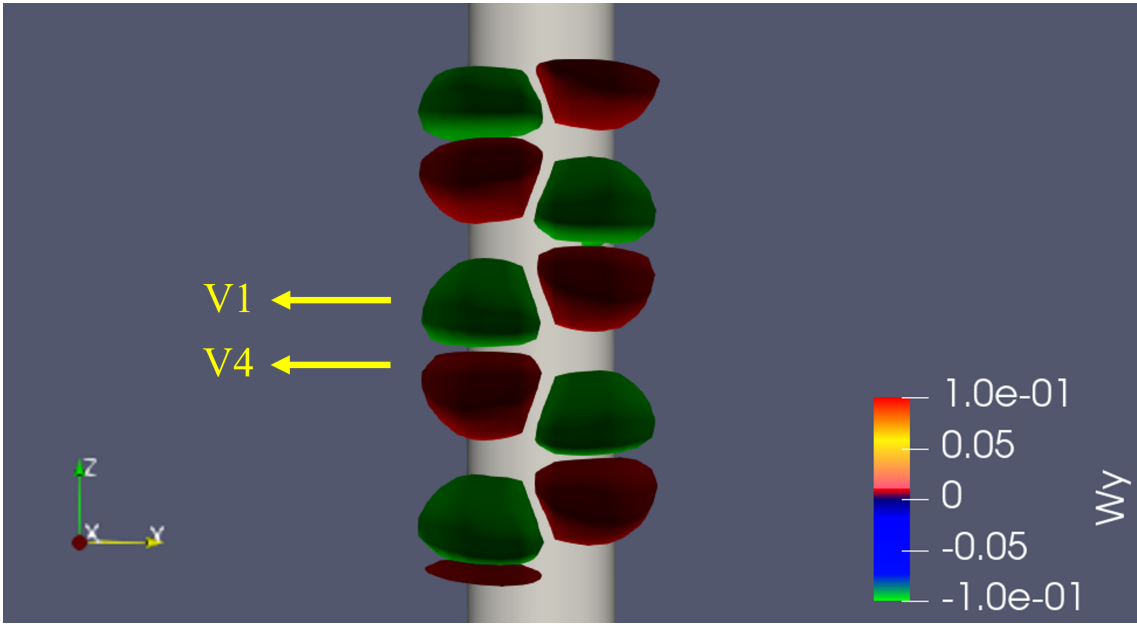


Figure 43: Vorticity isosurfaces  $\omega_y = \pm 0.1$  around the cylinder at time  $t = 821.66s$ , in the range  $-7 < z/D < -3$ .

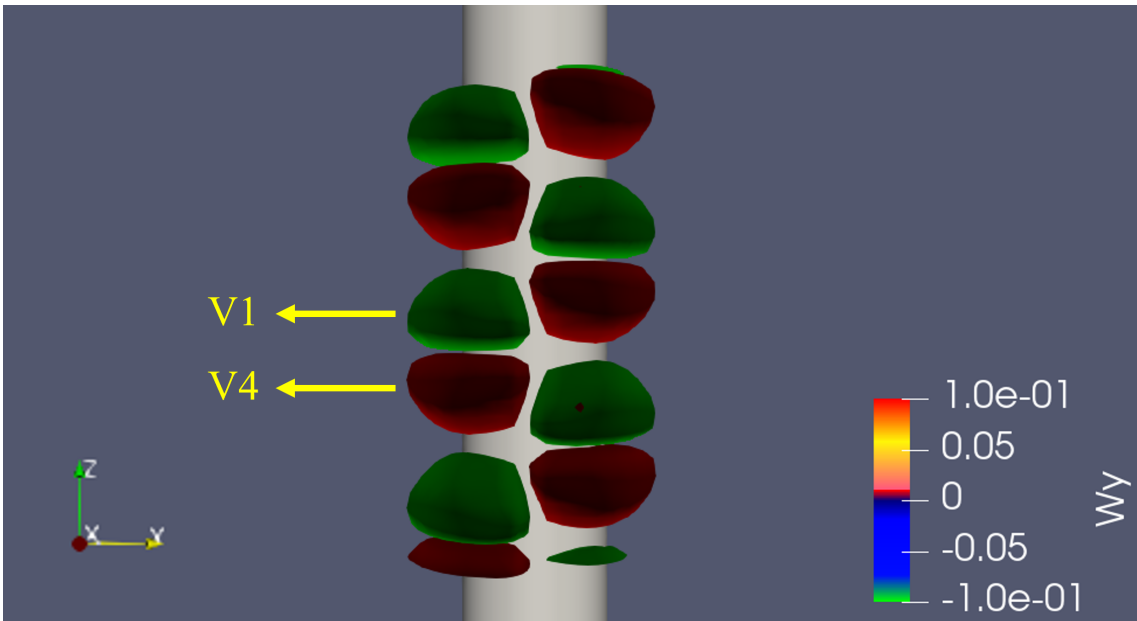


Figure 44: Vorticity isosurfaces  $\omega_y = \pm 0.1$  around the cylinder at time  $t = 832.51s$ , in the range  $-7 < z/D < -3$ .



---

## 7 Discussion

The results of the simulation focus on showing the effect of the three-dimensional effect on the flow around the small cylinder and the large cylinder. The fluid structure after the step cylinder can be divided into three zones (up zone, interface zone and bottom zone) regarding to its position along the axis. This is similar to the S-cell, N-cell and L-cell in indirect mode defined by Dunn [19]. However, unlike indirect mode, there are no vortices moving away from the small and large cylinders. This is because by adjusting the diameter ratio, KC number and  $\beta$ , the flow around the small cylinder is set to regime A and the flow around the large cylinder is set to regime B.

In regime A, vortices are formed at the end of a half oscillatory period, but they do not survive in to the next half oscillatory period, and thus no vortices shade away from the small cylinder. Since there are no vortices, the flow behind the small cylinder remain two-dimensional which is the same as the results obtained in simulation shown in Figure 31 and Figure 32. In addition, the results show that the three-dimensional effect due to the presence of the step does not have a significant effect on the regime A flow behind the small cylinder. The three-dimensional effect due to the discontinuity influences the flow only in 0.9 diameter upward. The reason why step cause less effect on the flow behind small cylinder, can be explained by the pressure difference between the large and small cylinders. The pressure of the small cylinder is larger than the large cylinder, and this difference makes the small cylinder wake extend downward and offsets the impact of the step. On the other hand, this downwash caused by the pressure difference enhances the downward three-dimensional effect (due to the step) on the flow behind the large cylinder and make the Honji vortex in regime B less stable.

Unlike its slight effect on the flow behind the small cylinder, the three-dimensionality has great impact on the flow below the step and make the three-dimensional dynamics in regime B more complex. Figure 31 shows that in present simulation, the flow in regime B transform from two-dimensional flow to three-dimensional flow instantly. Although it can be found from the simulation results that the appearance of the step and the downwash from small cylinder has a strong three-dimensional effect to the flow behind the large cylinder, it's hard to tell what really caused this instantaneous transition from two to three dimensional. In their study, Zhang [43] shows that the flow with parameters  $KC = 2.6$  and  $\beta = 196$  has much strong three-dimensional motion and the transition from two-dimensional flow to three-dimensional flow only take about ten cycles of calculation. Thus, a larger KC number ( $KC = 2.8$ ) could result the great three-dimensionality in the flow in regime B. In addition to the effects of the step and the large  $KC$  value, the numerical code MGLET itself used in the simulation may also cause this instantaneous transition from two to three dimensional. Figure 21 shows that even with same flow parameters  $KC = 2$  and  $\beta = 200$ , compared to the results form Jiang [36] and An [14], the numerical simulation results obtained by using MGLET lose the two to three-dimensional transition. In summary, it is hard to determine what causes this very strong initial three-dimensional effect based on present results of numerical simulation.

Another thing worth discussing is the appearance process of Honji vortex. Although the process of Honji vortex generation has been described by many previous studies abased on experiments (Sarpkaya [8], Honji [6]) and numerical simulations (An [14], Yang [42]), the cause of Honji vortex generation in the present study is different from them and is found for the first time. In these previous studies, the described generation process of Honji vortex is about the emergence of Honji vortex pairs along whole uniform cylinder or the appearance of a pair of Honji vortex near the area where merging process occurred. This present thesis describes the generation of new Honji vortex pair due to the presence of the step. Unlike other studies where the Honji vortex appear in pairs, it can be obtained from the Figure 31 that in present simulation not all Honji vortexes are paired in the development of the flow structure. In present study a total of 20.5 or 21.5 pairs of Honji vortex are distributed along the axis of the large cylinder. It can be found from Figure 33 to Figure 37 that the Honji vortex within one to two diameter lengths below the step lost its companions. This absence of Honji vortex is most likely related to the three-dimensional effect due to the presence of step. As mentioned in previous chapter, the Honji instability is an onset three-dimensional instability, and thus it could be easily affected by the strong three-dimensionality near the step and finally lose it's unstable structure. The lose of counter-rotating vortex makes the remaining

---

Honji vortex stronger but unstable. Thus this remaining unstable Honji vortex tends to move away from the step which increases the spacing between step and leave the enough space for generation of new vortices. As the remaining vortex becomes stronger and stronger, it rolls up the boundary to form a new counter-rotating vortex. However, at the same time, another vortex with the same rotating direction as the remaining unstable vortex appears under the step. As a result, those two newly generated Honji vortices do not stabilize the rest Honji vortices, and thus the flow structures are still unstable and continue cause the generation of new Honji vortices below the step.

As these newly generated Honji vortices become stronger and stronger, they push other Honji vortex pairs downward, and the merging process of Honji vortex occurs when the distance between these Honji vortices is small. The results from Figure 38 to Figure 44 show the merging process of Honji vortex on both side of the step cylinder. It is obvious that the merging processes are different at the each side of the step cylinder. On the negative y side, two neighbouring Honji vortex pairs merge together. In his study, An [14] describes this merging process in detail. As the two neighbouring Honji vortex pairs move toward each other, the positive part  $V2$  of the upper vortex pair and the negative part  $V3$  of the lower vortex pair effectively cancel each other. As the time goes by,  $V2$  and  $V3$  finally destroy each other completely, and the remaining negative part  $V1$  and the positive part  $V4$  gather together and form a new Honji vortex pair. However, on the other side of the step cylinder, the Honji vortex pair formed by  $V5$  and  $V6$  disappears rather than merge to their neighbouring vortex pairs. The reason why that this can not be clearly defined as a merging process is because if the merging process happens,  $V5$  and  $V6$  are supposed to be cancelled with the vortices in their neighbouring vortex pairs, and these three vortex pairs should merge together and form only one new vortex pair, like what happens in merging process in the other side of the step cylinder. As for why this phenomenon occurs, the results of the simulation do not provide a clear answer. The hypothesis is that it is because this disappeared Honji vortex pair is simultaneously squeezed by the upper and lower neighboring Honji vortex pairs. The  $V5$  and  $V6$  are not only cancelled by neighboring vortices, but the decrease spacing limits the rolling up of the boundary, and thus the development of Honji vortex pair with  $V5$  and  $V6$  is suppressed. As a result, because the cancellation and the suppression occurs simultaneously, the vortices in the neighboring Honji vortex pairs are not destroyed completely by the disappeared Honji vortex pair. However, it should be noted, that this is only a hypothesis. In the future more detailed simulations need to be done to discover the real cause of this phenomenon.

---

## 8 Conclusion

This thesis focuses on the oscillatory flow around a step cylinder. In this simulation, by adjusting the values diameter ratio to 1.8, KC number to 2.8, and  $\beta$  to 80, the flow around the small cylinder is set in regime A, while the flow around the large cylinder is set in regime B. According to the results of this study, the following conclusions can be made:

- The three-dimensionality resulted by the presence of the step slightly affects the flow patterns behind the small cylinder, while it has a great impacts on the flow around the large cylinder. The flow behind small cylinder remains its two-dimensional features like it has in regime A around a uniform cylinder. The three-dimensionality near the step lead to instability in Honji vortices around the step cylinder in regime B and finally induce two kinds of long-term phenomenons: appearance and merging of Honji vortex pair.
- The cause of Honji vortex generation in the present study is instability in Honji vortics due to the lack of half vortex pair. In present study a total of 20.5 or 21.5 pairs of Honji vortex are distributed along the axis of the large cylinder. The lose of counter-rotating vortex makes the remaining Honji vortex stronger but unstable. As time goes by, the newly generated Vortices appear in a pair. One part of the newly generated vortex pair and the unstable Honji vortex form a new pair, but the other vortex of the newly generated vortex pair are left alone, and thus the instability in Honji vortics continues.
- The merging process of the Honji vortex shows different features in negative and positive y side of the step cylinder. On the negative side, as two neighbouring Honji vortex pairs move toward each other, the negative part of upper pair and the positive part of lower pair cancelled each other completely and the two remaining vortices form a new vortex pair. On the positive side, as the upper and lower vortex pairs keep squeezing the middle vortex pair. The middle vortex pair finally disappear due to the cancellation and suppression effect.

Although the results of this simulation can provide people with basic understanding such as the effect of step, Honji vortex generation and merging, the information provided by the preset results is still limited. Thus, some further work is recommended as follow:

- **Do the same simulation with another numerical solver.** The results obtained from the numerical code MGLET tends to eliminate the initial two-dimensional dynamics in regimes B. This makes it difficult to determine what led to the great three-dimensionality at the very beginning of the simulation. So, it is very necessary to go through the whole simulation again with another numerical solver.
- **Do the simulation again with same flow parameters but with a dual step cylinder.** Half of a Honji vortex pair disappears due to the three-dimensionality caused by the presence of the step. This lost vortex lead to instability of the rest Honji vortex pairs. Thus, it is interesting to reduce another half of a Honji vortex pair by using dual step cylinder and investigate how it affects the flow pattern.
- **Conduct more detailed investigation of the present results.** In this thesis, the results of the numerical simulation are presented by temporal and spatial evolution of the spanwise velocity component and vorticity isosurfaces. They can provide people with some useful information, but other visualization such as contours and streamlines can provide more detailed information of the flow development.

---

## Bibliography

- [1] Morison, J. R. and Johnsonf, J. W. ‘The Force Exerted by Surface Waves on Piles’. In: *J Pet Technol* 05 (1950).
- [2] Keulegan, G. H. and Carpenter, L.H. ‘Forces on Cylinders and Plates in an Oscillating Fluid’. In: *Journal of Research of the National Bureau of Standards* 60 (1958).
- [3] Sarpkaya, T. ‘Vortex shedding and resistance in harmonic flow about smooth and rough circular cylinders’. In: *J. Fluids Mech* (1976). DOI: <http://hdl.handle.net/10945/29595>.
- [4] Williamson, C. H. K. ‘Sinusoidal flow relative to circular cylinders’. In: *J. Fluid Mech* 155,141 (1985). DOI: [doi:10.1017/S0022112085001756](https://doi.org/10.1017/S0022112085001756).
- [5] Tatsuno, M. and Bearman, P. W. ‘A visual study of the flow around an oscillating circular cylinder at low Keulegan-Karpenter numbers and low Stokes numbers’. In: *J. Fluid Mech* 211,157 (1990). DOI: [doi:10.1017/S0022112090001537](https://doi.org/10.1017/S0022112090001537).
- [6] Honji, H. ‘Streaked flow around an oscillating circular cylinder’. In: *J. Fluids Mech* 107 (1981), pp. 509–520. DOI: <https://doi.org/10.1017/S0022112081001894>.
- [7] Hall, P. ‘On the stability of the unsteady boundary layer on a cylinder oscillating transversely in a viscous fluid’. In: *J. Fluids Mech* 146 (1984), pp. 347–367. DOI: [doi:10.1017/S0022112084001907](https://doi.org/10.1017/S0022112084001907).
- [8] Sarpkaya, T. ‘Experiments on the stability of sinusoidal flow over a circular cylinder’. In: *J. Fluids Mech* 457 (2002), pp. 157–180. DOI: [doi:10.1017/S002211200200784X](https://doi.org/10.1017/S002211200200784X).
- [9] Justesen, P. ‘A numerical study of oscillating flow around a circular cylinder.’ In: *J. Fluid Mech* 222,157-196 (1991). DOI: [doi:10.1017/S0022112091001040](https://doi.org/10.1017/S0022112091001040).
- [10] Dütsch, H. ‘Low-Reynolds-number flow around an oscillating circular cylinder at low Keulegan-Carpenter numbers.’ In: *J. Fluid Mech* 360,249 (1998). DOI: [doi:10.1017/S002211209800860X](https://doi.org/10.1017/S002211209800860X).
- [11] Lin, X. W. ‘A numerical study of oscillatory flow about a circular cylinder for low values of beta parameters.’ In: *J. Fluids Struct* 10,501-526 (1996). DOI: <https://doi.org/10.1006/jfls.1996.0034>.
- [12] Nehari, D. and Ballio, F. ‘Three-dimensional analysis of the unidirectional oscillatory flow around a circular cylinder at low Keulegan–Carpenter and  $\beta$  numbers.’ In: *J. Fluid Mech* 520,157-186 (2004). DOI: [doi:10.1017/S002211200400134X](https://doi.org/10.1017/S002211200400134X).
- [13] Zhang, J. F. and Dalton, C. ‘The onset of three-dimensionality in an oscillating flow past a fixed circular cylinder’. In: *Int. J. Numer. Methods Fluids* 30 (1999), pp. 19–42. DOI: <https://onlinelibrary.wiley.com/doi/abs/10.1002/>.
- [14] An, H. W. ‘Direct numerical simulation of oscillatory flow around a circular cylinder at low Keulegan–Carpenter number’. In: *J. Fluid Mech* 666 (2011), pp. 77–103. DOI: <https://doi.org/10.1017/S0022112010003691>.
- [15] Ko, N. W. M. and Leung, W. L. ‘Flow Behind Two Coaxial Circular Cylinders.’ In: *J. Fluids Eng* 104,223-227 (1982). DOI: <https://doi.org/10.1115/1.3241814>.
- [16] Lewis, C. G. and Gharib. ‘An exploration of the wake three dimensionalities caused by a local discontinuity in cylinder diameter.’ In: *Phys. Fluids A* 4,104-117 (1992). DOI: <https://doi.org/10.1063/1.858489>.
- [17] Norberg, C. ‘An experimental study of the flow around cylinders joined with a step in the diameter.’ In: *11th Australasian Fluid Mechanics Conference* 507–510 (1992).
- [18] Chua, L. P. ‘Measurements of a step cylinder.’ In: *Annu. Rev. Fluid Mech* 205–215 (1998). DOI: [https://doi.org/10.1016/S0735-1933\(98\)00007-4](https://doi.org/10.1016/S0735-1933(98)00007-4).
- [19] Dunn, W. and Tavoularis, S. ‘Experimental studies of vortices shed from cylinders with a step-change in diameter.’ In: *J. Fluid Mech* 555,409–437 (2006). DOI: [doi:10.1017/S002211200600927X](https://doi.org/10.1017/S002211200600927X).
- [20] Tec-science. *Flow separation (boundary layer separation)*. URL: <https://www.tec-science.com/mechanics/gases-and-liquids/flow-separation-boundary-layer-separation/>.
- [21] Faltinsen, O. M. *Sea Loads on Ships and Offshore Structures*. Cambridge University Press, 1990.

- 
- [22] Sumer, B. M. *Hydrodynamics Around Cylindrical Structures*. World Scientific, 2006.
- [23] Elston, J. R. ‘Two-dimensional Floquet stability analysis of the flow produced by an oscillating circular cylinder in quiescent fluid.’ In: *Eur. J. Mech.* 23,99–106 (2004). DOI: <https://doi.org/10.1016/j.euromechflu.2003.05.002>.
- [24] Zhaom, M. and Cheng. ‘Two-dimensional numerical study of vortex shedding regimes of oscillatory flow past two circular cylinders in side-by-side and tandem arrangements at low Reynolds numbers.’ In: *J. Fluid Mech.* 751,1–37 (2014). DOI: [doi:10.1017/jfm.2014.268](https://doi.org/10.1017/jfm.2014.268).
- [25] Tong, F. ‘Oscillatory flow regimes around four cylinders in a square arrangement under small KC and Re conditions.’ In: *J. Fluid Mech.* 769,298–336 (2015). DOI: [doi:10.1017/jfm.2015.107](https://doi.org/10.1017/jfm.2015.107).
- [26] Morton, C. and Yarusevych, S. ‘Vortex shedding in the wake of a step cylinder.’ In: *Phys. Fluids*. 22,083602 (2010). DOI: <https://doi.org/10.1063/1.3459157>.
- [27] Ferziger, J. H. *Computational methods for fluid dynamics*. Verlag Berlin Heidelberg NewYork, Springer, 2002.
- [28] Williamson, J. H. ‘Low-storage Runge-Kutta schemes’. In: *Int. J. Computational Physics* 35 (1980), pp. 48–56. DOI: [https://doi.org/10.1016/0021-9991\(80\)90033-9](https://doi.org/10.1016/0021-9991(80)90033-9).
- [29] Manhart, M. ‘MGLET: a parallel code for efficient DNS and LES of complex geometries’. In: *Parallel Computational Fluid Dynamics 2000* (2001), pp. 449–456. DOI: <https://doi.org/10.1016/B978-044450673-3/50123-8>.
- [30] Harlow, H. and Welsh, J. E. ‘Numerical calculation of time-dependent viscous incompressible flow with free surface’. In: *Phys Fluids* 8 (1965), pp. 2182–2189. DOI: <https://doi.org/10.1063/1.1761178>.
- [31] Manhart, M. ‘A zonal grid algorithm for DNS of turbulent boundary layers’. In: *Computers Fluids* 33 (2003), pp. 435–461. DOI: [https://doi.org/10.1016/S0045-7930\(03\)00061-6](https://doi.org/10.1016/S0045-7930(03)00061-6).
- [32] Jiang, F. J. ‘Cavity flows and wake behind an elliptic cylinder translating above the wall’. In: *Institutt for marin teknikk* 978-82-326-4973-0 (2020). DOI: <https://hdl.handle.net/11250/2687355>.
- [33] Peller, N. ‘High-order stable interpolations for immersed boundary methods.’ In: *International Journal for Numerical Methods in Fluids* 52,1175–1193 (2006). DOI: <https://doi.org/10.1002/flid.1227>.
- [34] Williamson, J. H. ‘Low-storage Runge-Kutta schemes’. In: *Int. J. Computational Physics* 35 (1980), pp. 48–56. DOI: [https://doi.org/10.1016/0021-9991\(80\)90033-9](https://doi.org/10.1016/0021-9991(80)90033-9).
- [35] Canabes, J. P. G. *Numerical studies of viscous flow around bluff bodies*. NTNU, 2015.
- [36] Jiang, F. J. ‘Flow around an oscillating cylinder: computational issues’. In: *Fluid Dyn* 49 (2017). DOI: <https://iopscience.iop.org/article/10.1088/1873-7005/aa7e1c>.
- [37] Batchelor, G. *An Introduction to Fluid Dynamics*. Cambridge: Cambridge University Press, 1967.
- [38] Bearman, P. W. ‘Forces on cylinders in viscous oscillatory flow at low Keulegan–Carpenter numbers’. In: *J. Fluid Mech* 154 (1985), pp. 337–356. DOI: <https://doi.org/10.1017/S0022112085001562>.
- [39] Justesen, P. ‘A numerical study of oscillating flow around a circular cylinder’. In: *J. Fluid Mech* 222 (1991), pp. 157–196. DOI: <https://doi.org/10.1017/S0022112091001040>.
- [40] Rashid, F. ‘Oscillating cylinder in viscous fluid: calculation of flow patterns and forces’. In: *J. Eng. Math* 70 (2011), pp. 281–95. DOI: <https://doi.org/10.1007/s10665-010-9395-7>.
- [41] Justesen, P. ‘A numerical study of oscillating flow around a circular cylinder’. In: *J. Fluid Mech* 222 (1991), pp. 157–196. DOI: <https://doi.org/10.1017/S0022112091001040>.
- [42] Yang, K. ‘Effects of an axial flow component on the Honji instability’. In: *J. Fluids Struct* 49 (2014), pp. 614–639. DOI: <https://doi.org/10.1016/j.jfluidstructs.2014.06.003>.
- [43] Zhang, J. F. ‘The onset of three-dimensionality in an oscillating flow past a fixed circular cylinder’. In: *International Journal for Numerical Methods in Fluids* 30.1 (1999), pp. 19–42. DOI: [https://doi.org/10.1002/\(SICI\)1097-0363\(19990515\)30:1<19::AID-FLD836>3.0.CO;2-#](https://doi.org/10.1002/(SICI)1097-0363(19990515)30:1<19::AID-FLD836>3.0.CO;2-#).
-

